

A minimal longitudinal dynamic model of a tailless flapping wing robot

K.M. Kajak

March 2, 2018

A minimal longitudinal dynamic model of a tailless flapping wing robot

MASTER OF SCIENCE THESIS

For obtaining the degree of Master of Science in Aerospace Engineering
at Delft University of Technology

K.M. Kajak

March 2, 2018



Delft University of Technology

Copyright © K.M. Kajak
All rights reserved.

DELFT UNIVERSITY OF TECHNOLOGY
DEPARTMENT OF
CONTROL AND SIMULATION

The undersigned hereby certify that they have read and recommend to the Faculty of Aerospace Engineering for acceptance a thesis entitled “**A minimal longitudinal dynamic model of a tailless flapping wing robot**” by **K.M. Kajak** in partial fulfillment of the requirements for the degree of **Master of Science**.

Dated: March 2, 2018

Readers:

dr.ir. M. Karásek

dr.ir. Q. P. Chu

dr.ir. G. C. H. E. de Croon

dr.ir. B. W. van Oudheusden

Acronyms

AHRS	Attitude Heading Reference System
CFD	Computational Fluid Dynamics
DC	Direct Current
DCM	Direction Cosine Matrix
DOF	Degrees Of Freedom
DTLTI	Discrete Time Linear Time Invariant
FPGA	Field Programmable Gate Array
FWMAV	Flapping Wing Micro Air Vehicle
IMU	Inertial Measurement Unit
LQG	Linear Quadratic Gaussian
LQR	Linear Quadratic Regulator
LTI	Linear Time Invariant
MAV	Micro Air Vehicle
MAVLab	Micro Air Vehicle Laboratory
NLTV	Nonlinear Time Varying
OJF	Open Jet Facility
PD	Proportional-Derivative
PEM	Prediction Error Method
PID	Proportional-Integral-Derivative
PWM	Pulse Width Modulation
SD	Secure Digital

List of Symbols

Greek Symbols

β	Drag force coefficient
γ	Dihedral angle
γ_1	Dihedral angle before velocity correction
γ_2	Dihedral angle after velocity correction
γ_c	Dihedral angle command
$\dot{\gamma}_1$	Dihedral angle rate before velocity correction
$\dot{\gamma}_2$	Dihedral angle rate after velocity correction
Φ	Flapping amplitude
π	Ratio of the circumference of a circle to the diameter
τ	Flapping frequency actuator dynamics time constant
θ	Pitch angle
$\dot{\theta}$	Pitch rate
$\ddot{\theta}$	Pitch acceleration
$\dot{\theta}_{ref}$	Pitch rate reference
θ_{ref}	Pitch angle reference
θ_{sp}	Pitch angle setpoint
ω_n	Dihedral actuator natural frequency
ζ	Dihedral actuator damping

Roman Symbols

$A(z)$	Actuator dynamics
--------	-------------------

b	Wingspan
b_x	Linear damping force coefficient for aerodynamic force along body axis X
b_z	Linear damping force coefficient for aerodynamic force along body axis Z
c_1	Slope of linear thrust as a function of flapping frequency
c_2	Bias of linear thrust as a function of flapping frequency
c_{ucorr}	Dihedral angle velocity correction coefficient
f	Flapping frequency
f_c	Flapping frequency command
f_{cut}	Cutoff frequency of the command filter
f_d	Drag force
\dot{f}_d	Stroke-averaged drag force
g	Gravitational acceleration
$H_{dihedral}$	Actuator dynamics of the dihedral angle
H_{flap}	Actuator dynamics of the flapping frequency
$H(z)$	Second order measurement filter
I_{yy}	Moment of inertia
K_D	Rate feedback gain
K_P	Attitude feedback gain
l_d	The linear displacement of the thrust vector/aerodynamic center from its neutral position
\dot{l}_d	The linear velocity of the thrust vector/aerodynamic center along body axis X
l_p	The linear displacement of the thrust vector/aerodynamic center from its neutral position
$l_{p,c}$	The commanded linear displacement of the thrust vector/aerodynamic center from its neutral position
l_x	The fixed linear offset of the wing neutral position from the center of mass along the body axis X
l_y	The fixed linear offset of the wing neutral position from the center of mass along the body axis Y
l_z	The fixed linear offset of the thrust vector/aerodynamic center from the center of mass along the body axis Z
M	Pitch moment
P_q	Quaternion feedback gain
P_ω	Rate feedback gain
q	Pitch rate

q_m	Quaternion measurement
q_{ref}	Quaternion reference
T	Thrust
u	Air velocity projection onto body axis X
U	Wing velocity due to flapping
u_{COP}	Air velocity of the wing projected onto body axis X
\dot{u}	Body frame acceleration along axis X
w	Air velocity projection onto body axis Z
w_{COP}	Air velocity of the wing projected onto body axis Z
\dot{w}	Body frame acceleration along axis Z
ω_m	Rate measurement
X	Body frame axis
X_b	Body frame axis
Z	Body frame axis
Z_b	Body frame axis

Contents

Acronyms	v
List of Symbols	vii
1 Introduction	1
I Paper	3
II Preliminary studies	19
2 Introduction to the preliminary research	21
3 Existing tail-less FWMAVs	23
4 Modeling	27
4-1 Previous work in FWMAV modeling	27
5 Control	29
5-1 Detailed review of control studies	29
5-1-1 Deng, Schenato et al.	32
5-1-2 Doman et al.	32
5-1-3 Serrani et al.	33
5-1-4 Sun, Wang, Xiong, et al.	33
5-1-5 Rifaï et al.	33
5-1-6 Cheng and Deng	34
5-1-7 Geder et al.	34

5-1-8	Bayandor et al.	34
5-1-9	Gallagher et al., Chung and Dorothy	34
5-1-10	Li and Duan	35
5-1-11	Jun-Seong Lee et al.	35
5-1-12	Maria-Belmonte et al.	35
5-1-13	Guo et al.	35
5-1-14	Du et al.	35
5-1-15	Bluman et al.	36
5-1-16	Keennon et al.	36
5-1-17	Wood et al.	36
5-2	General aircraft stabilizing control approaches	37
5-3	Proposed control system candidates for implementation on the DelFly	38
5-3-1	Single-gain quaternion-based attitude feedback	39
5-3-2	Gain-scheduled quaternion-based attitude feedback	39
5-3-3	Adaptive feedback control	39
6	Model development for DelFly Transformer tailless FWMAV	41
6-1	Thrust force and thrust actuator dynamics	41
6-2	Pitch moment actuator dynamics	43
6-3	Experimental study of aerodynamic forces	47
6-4	Full nonlinear longitudinal model	48
6-5	Model validation	50
A	Individual flight maneuvers - dataset I	53
A-1	Maneuvers with 15 degree pitch setpoints	53
A-2	Maneuvers with 30 degree pitch setpoints	57
A-3	Maneuvers with 45 degree pitch setpoints	61
A-4	Maneuvers with 60 degree pitch setpoints	69
A-5	Maneuvers with 70 degree pitch setpoints	76
A-6	Maneuvers with 80 degree pitch setpoints	78
B	Individual flight maneuvers - dataset II	81
B-1	Maneuvers with front heavy center of mass and 30 degree pitch setpoints	81
B-2	Maneuvers with bottom heavy center of mass and 30 degree pitch setpoints	86
C	Individual flight maneuvers - dataset III	91
C-1	Maneuvers with 40 degree pitch setpoints, baseline controller	91
C-2	Maneuvers with 40 degree pitch setpoints, command filter cutoff 10 Hz	94
C-3	Maneuvers with 40 degree pitch setpoints, command filter cutoff 256 Hz	100
C-4	Maneuvers with 40 degree pitch setpoints, rate feedback gain 600	105
C-5	Maneuvers with 40 degree pitch setpoints, rate feedback gain 800	110
C-6	Maneuvers with 40 degree pitch setpoints, attitude feedback gain 3900	115
C-7	Maneuvers with 40 degree pitch setpoints, attitude feedback gain 11700	121
	Bibliography	127

List of Figures

2-1	DelFly Transformer first prototype	22
3-1	KUBeetle	24
3-2	Nano Hummingbird	24
3-3	RoboBee	25
5-1	Quaternion attitude/rate controller layout	39
5-2	INDI controller layout	40
6-1	Thrust versus flapping frequency.	42
6-2	Flapping frequency versus average PWM signal	43
6-3	Approximately scaled flapping command function versus the original and filtered measurement.	44
6-4	Measured (black) and simulated (blue) flapping frequency.	45
6-5	Filtered, calculated pitch leverage arm (red) and simulated pitch leverage arms (blue - 1 pole, green - 2 poles).	46
6-6	Free body diagram for Equations 6-1. C.O.M. - center of mass, C.O.P. - center of pressure.	47
6-7	Lift and drag versus airspeed and pitch angle (measurements - blue, model - green). 48	
6-8	Aerodynamic body frame forces versus body velocities (measurements - blue, model - green).	49
6-9	Free body diagram of the FWMAV, longitudinal forces only. C.O.M. - center of mass, C.O.P. - center of pressure.	50
6-10	Model fit with previously identified values. X-axis is data point index	51
6-11	Model fit with previously identified values and actual hinge position. X-axis is data point index	52
A-1	First validation step maneuver with 15 degree pitch forwardsetpoint.	53

A-2	Second validation step maneuver with 15 degree pitch forward setpoint.	54
A-3	Third validation step maneuver with 15 degree pitch forward setpoint.	54
A-4	Fourth validation step maneuver with 15 degree pitch forward setpoint.	54
A-5	Fifth validation step maneuver with 15 degree pitch forward setpoint.	55
A-6	First validation step maneuver with 15 degree pitch backward setpoint.	55
A-7	Second validation step maneuver with 15 degree pitch backward setpoint.	55
A-8	Third validation step maneuver with 15 degree pitch backward setpoint.	56
A-9	Fourth validation step maneuver with 15 degree pitch backward setpoint.	56
A-10	First validation step maneuver with 30 degree pitch forward setpoint.	57
A-11	Second validation step maneuver with 30 degree pitch forward setpoint.	57
A-12	Third validation step maneuver with 30 degree pitch forward setpoint.	58
A-13	Fourth validation step maneuver with 30 degree pitch forward setpoint.	58
A-14	Fifth validation step maneuver with 30 degree pitch forward setpoint.	58
A-15	Sixth validation step maneuver with 30 degree pitch forward setpoint.	59
A-16	First validation step maneuver with 30 degree pitch backward setpoint.	59
A-17	Second validation step maneuver with 30 degree pitch backward setpoint.	59
A-18	Third validation step maneuver with 30 degree pitch backward setpoint.	60
A-19	Fourth validation step maneuver with 30 degree pitch backward setpoint.	60
A-20	Fifth validation step maneuver with 30 degree pitch backward setpoint.	60
A-21	First validation step maneuver with 45 degree pitch forward setpoint.	61
A-22	Second validation step maneuver with 45 degree pitch forward setpoint.	61
A-23	Third validation step maneuver with 45 degree pitch forward setpoint.	62
A-24	Fourth validation step maneuver with 45 degree pitch forward setpoint.	62
A-25	Fifth validation step maneuver with 45 degree pitch forward setpoint.	62
A-26	Sixth validation step maneuver with 45 degree pitch forward setpoint.	63
A-27	Seventh validation step maneuver with 45 degree pitch forward setpoint.	63
A-28	Eighth validation step maneuver with 45 degree pitch forward setpoint.	63
A-29	Ninth validation step maneuver with 45 degree pitch forward setpoint.	64
A-30	Tenth validation step maneuver with 45 degree pitch forward setpoint.	64
A-31	Eleventh validation step maneuver with 45 degree pitch forward setpoint.	64
A-32	First validation step maneuver with 45 degree pitch backward setpoint.	65
A-33	Second validation step maneuver with 45 degree pitch backward setpoint.	65
A-34	Third validation step maneuver with 45 degree pitch backward setpoint.	65
A-35	Fourth validation step maneuver with 45 degree pitch backward setpoint.	66
A-36	Fifth validation step maneuver with 45 degree pitch backward setpoint.	66
A-37	Sixth validation step maneuver with 45 degree pitch backward setpoint.	66
A-38	Seventh validation step maneuver with 45 degree pitch backward setpoint.	67
A-39	Eighth validation step maneuver with 45 degree pitch backward setpoint.	67

A-40	Ninth validation step maneuver with 45 degree pitch backward setpoint.	67
A-41	Tenth validation step maneuver with 45 degree pitch backward setpoint.	68
A-42	Eleventh validation step maneuver with 45 degree pitch backward setpoint.	68
A-43	First validation step maneuver with 60 degree pitch forward setpoint.	69
A-44	Second validation step maneuver with 60 degree pitch forward setpoint.	69
A-45	Third validation step maneuver with 60 degree pitch forward setpoint.	70
A-46	Fourth validation step maneuver with 60 degree pitch forward setpoint.	70
A-47	Fifth validation step maneuver with 60 degree pitch forward setpoint.	70
A-48	Sixth validation step maneuver with 60 degree pitch forward setpoint.	71
A-49	Seventh validation step maneuver with 60 degree pitch forward setpoint.	71
A-50	Eighth validation step maneuver with 60 degree pitch forward setpoint.	71
A-51	Ninth validation step maneuver with 60 degree pitch forward setpoint.	72
A-52	Tenth validation step maneuver with 60 degree pitch forward setpoint.	72
A-53	Eleventh validation step maneuver with 60 degree pitch forward setpoint.	72
A-54	Twelfth validation step maneuver with 60 degree pitch forward setpoint.	73
A-55	Thirteenth validation step maneuver with 60 degree pitch forward setpoint.	73
A-56	Fourteenth validation step maneuver with 60 degree pitch forward setpoint.	73
A-57	Fifteenth validation step maneuver with 60 degree pitch forward setpoint.	74
A-58	First validation step maneuver with 60 degree pitch backward setpoint.	74
A-59	Second validation step maneuver with 60 degree pitch backward setpoint.	74
A-60	Third validation step maneuver with 60 degree pitch backward setpoint.	75
A-61	First validation step maneuver with 70 degree pitch forward setpoint.	76
A-62	Second validation step maneuver with 70 degree pitch forward setpoint.	76
A-63	Third validation step maneuver with 70 degree pitch forward setpoint.	77
A-64	Fourth validation step maneuver with 70 degree pitch forward setpoint.	77
A-65	First validation step maneuver with 80 degree pitch forward setpoint.	78
A-66	Second validation step maneuver with 80 degree pitch forward setpoint.	78
A-67	Third validation step maneuver with 80 degree pitch forward setpoint.	78
A-68	Fourth validation step maneuver with 80 degree pitch forward setpoint.	79
A-69	Fifth validation step maneuver with 80 degree pitch forward setpoint.	79
A-70	Sixth validation step maneuver with 80 degree pitch forward setpoint.	79
A-71	Seventh validation step maneuver with 80 degree pitch forward setpoint.	80
A-72	Eighth validation step maneuver with 80 degree pitch forward setpoint.	80
B-1	First validation step maneuver with a front heavy (4.8mm) center of mass and 30 degree pitch forward setpoint.	81
B-2	Second validation step maneuver with a front heavy (4.8mm) center of mass and 30 degree pitch forward setpoint.	82
B-3	Third validation step maneuver with a front heavy (4.8mm) center of mass and 30 degree pitch forward setpoint.	82

B-4	Fourth validation step maneuver with a front heavy (4.8mm) center of mass and 30 degree pitch forward setpoint.	82
B-5	Fifth validation step maneuver with a front heavy (4.8mm) center of mass and 30 degree pitch forward setpoint.	83
B-6	Sixth validation step maneuver with a front heavy (4.8mm) center of mass and 30 degree pitch forward setpoint.	83
B-7	First validation step maneuver with a front heavy (4.8mm) center of mass and 30 degree pitch backward setpoint.	83
B-8	Second validation step maneuver with a front heavy (4.8mm) center of mass and 30 degree pitch backward setpoint.	84
B-9	Third validation step maneuver with a front heavy (4.8mm) center of mass and 30 degree pitch backward setpoint.	84
B-10	Fourth validation step maneuver with a front heavy (4.8mm) center of mass and 30 degree pitch backward setpoint.	84
B-11	Fifth validation step maneuver with a front heavy (4.8mm) center of mass and 30 degree pitch backward setpoint.	85
B-12	Sixth validation step maneuver with a front heavy (4.8mm) center of mass and 30 degree pitch backward setpoint.	85
B-13	Seventh validation step maneuver with a front heavy (4.8mm) center of mass and 30 degree pitch backward setpoint.	85
B-14	First validation step maneuver with a bottom heavy (6mm) center of mass and 30 degree pitch forward setpoint.	86
B-15	Second validation step maneuver with a bottom heavy (6mm) center of mass and 30 degree pitch forward setpoint.	86
B-16	Third validation step maneuver with a bottom heavy (6mm) center of mass and 30 degree pitch forward setpoint.	87
B-17	Fourth validation step maneuver with a bottom heavy (6mm) center of mass and 30 degree pitch forward setpoint.	87
B-18	Fifth validation step maneuver with a bottom heavy (6mm) center of mass and 30 degree pitch forward setpoint.	87
B-19	Sixth validation step maneuver with a bottom heavy (6mm) center of mass and 30 degree pitch forward setpoint.	88
B-20	Seventh validation step maneuver with a bottom heavy (6mm) center of mass and 30 degree pitch forward setpoint.	88
B-21	First validation step maneuver with a bottom heavy (6mm) center of mass and 30 degree pitch backward setpoint.	88
B-22	Second validation step maneuver with a bottom heavy (6mm) center of mass and 30 degree pitch backward setpoint.	89
B-23	Third validation step maneuver with a bottom heavy (6mm) center of mass and 30 degree pitch backward setpoint.	89
B-24	Fourth validation step maneuver with a bottom heavy (6mm) center of mass and 30 degree pitch backward setpoint.	89
B-25	Fifth validation step maneuver with a bottom heavy (6mm) center of mass and 30 degree pitch backward setpoint.	90

B-26	Sixth validation step maneuver with a bottom heavy (6mm) center of mass and 30 degree pitch backward setpoint.	90
B-27	Seventh validation step maneuver with a bottom heavy (6mm) center of mass and 30 degree pitch backward setpoint.	90
C-1	First validation step maneuver with baseline controller and 40 degree pitch backward setpoint.	91
C-2	Second validation step maneuver with baseline controller and 40 degree pitch backward setpoint.	92
C-3	Third validation step maneuver with baseline controller and 40 degree pitch backward setpoint.	92
C-4	Fourth validation step maneuver with baseline controller and 40 degree pitch backward setpoint.	92
C-5	First validation step maneuver with baseline controller and 40 degree pitch forward setpoint.	93
C-6	Second validation step maneuver with baseline controller and 40 degree pitch forward setpoint.	93
C-7	First validation step maneuver with 10 Hz command filter cutoff frequency and 40 degree pitch forward setpoint.	94
C-8	Second validation step maneuver with 10 Hz command filter cutoff frequency and 40 degree pitch forward setpoint.	94
C-9	Third validation step maneuver with 10 Hz command filter cutoff frequency and 40 degree pitch forward setpoint.	95
C-10	Fourth validation step maneuver with 10 Hz command filter cutoff frequency and 40 degree pitch forward setpoint.	95
C-11	Fifth validation step maneuver with 10 Hz command filter cutoff frequency and 40 degree pitch forward setpoint.	95
C-12	Sixth validation step maneuver with 10 Hz command filter cutoff frequency and 40 degree pitch forward setpoint.	96
C-13	Seventh validation step maneuver with 10 Hz command filter cutoff frequency and 40 degree pitch forward setpoint.	96
C-14	Eighth validation step maneuver with 10 Hz command filter cutoff frequency and 40 degree pitch forward setpoint.	96
C-15	First validation step maneuver with 10 Hz command filter cutoff frequency and 40 degree pitch backward setpoint.	97
C-16	Second validation step maneuver with 10 Hz command filter cutoff frequency and 40 degree pitch backward setpoint.	97
C-17	Third validation step maneuver with 10 Hz command filter cutoff frequency and 40 degree pitch backward setpoint.	97
C-18	Fourth validation step maneuver with 10 Hz command filter cutoff frequency and 40 degree pitch backward setpoint.	98
C-19	Fifth validation step maneuver with 10 Hz command filter cutoff frequency and 40 degree pitch backward setpoint.	98
C-20	Sixth validation step maneuver with 10 Hz command filter cutoff frequency and 40 degree pitch backward setpoint.	98
C-21	Seventh validation step maneuver with 10 Hz command filter cutoff frequency and 40 degree pitch backward setpoint.	99

C-22	First validation step maneuver with 256 Hz command filter cutoff frequency and 40 degree pitch forward setpoint.	100
C-23	Second validation step maneuver with 256 Hz command filter cutoff frequency and 40 degree pitch forward setpoint.	100
C-24	Third validation step maneuver with 256 Hz command filter cutoff frequency and 40 degree pitch forward setpoint.	101
C-25	Fourth validation step maneuver with 256 Hz command filter cutoff frequency and 40 degree pitch forward setpoint.	101
C-26	Fifth validation step maneuver with 256 Hz command filter cutoff frequency and 40 degree pitch forward setpoint.	101
C-27	Sixth validation step maneuver with 256 Hz command filter cutoff frequency and 40 degree pitch forward setpoint.	102
C-28	Seventh validation step maneuver with 256 Hz command filter cutoff frequency and 40 degree pitch forward setpoint.	102
C-29	First validation step maneuver with 256 Hz command filter cutoff frequency and 40 degree pitch backward setpoint.	102
C-30	Second validation step maneuver with 256 Hz command filter cutoff frequency and 40 degree pitch backward setpoint.	103
C-31	Third validation step maneuver with 256 Hz command filter cutoff frequency and 40 degree pitch backward setpoint.	103
C-32	Fourth validation step maneuver with 256 Hz command filter cutoff frequency and 40 degree pitch backward setpoint.	103
C-33	Fifth validation step maneuver with 256 Hz command filter cutoff frequency and 40 degree pitch backward setpoint.	104
C-34	Sixth validation step maneuver with 256 Hz command filter cutoff frequency and 40 degree pitch backward setpoint.	104
C-35	Seventh validation step maneuver with 256 Hz command filter cutoff frequency and 40 degree pitch backward setpoint.	104
C-36	First validation step maneuver with rate feedback 600 (PPRZ units) and 40 degree pitch forward setpoint.	105
C-37	Second validation step maneuver with rate feedback 600 (PPRZ units) and 40 degree pitch forward setpoint.	105
C-38	Third validation step maneuver with rate feedback 600 (PPRZ units) and 40 degree pitch forward setpoint.	106
C-39	Fourth validation step maneuver with rate feedback 600 (PPRZ units) and 40 degree pitch forward setpoint.	106
C-40	Fifth validation step maneuver with rate feedback 600 (PPRZ units) and 40 degree pitch forward setpoint.	106
C-41	Sixth validation step maneuver with rate feedback 600 (PPRZ units) and 40 degree pitch forward setpoint.	107
C-42	Seventh validation step maneuver with rate feedback 600 (PPRZ units) and 40 degree pitch forward setpoint.	107
C-43	First validation step maneuver with rate feedback 600 (PPRZ units) and 40 degree pitch backward setpoint.	107
C-44	Second validation step maneuver with rate feedback 600 (PPRZ units) and 40 degree pitch backward setpoint.	108

C-45 Third validation step maneuver with rate feedback 600 (PPRZ units) and 40 degree pitch backward setpoint.	108
C-46 Fourth validation step maneuver with rate feedback 600 (PPRZ units) and 40 degree pitch backward setpoint.	108
C-47 Fifth validation step maneuver with rate feedback 600 (PPRZ units) and 40 degree pitch backward setpoint.	109
C-48 Sixth validation step maneuver with rate feedback 600 (PPRZ units) and 40 degree pitch backward setpoint.	109
C-49 Seventh validation step maneuver with rate feedback 600 (PPRZ units) and 40 degree pitch backward setpoint.	109
C-50 First validation step maneuver with rate feedback 800 (PPRZ units) and 40 degree pitch forward setpoint.	110
C-51 Second validation step maneuver with rate feedback 800 (PPRZ units) and 40 degree pitch forward setpoint.	110
C-52 Third validation step maneuver with rate feedback 800 (PPRZ units) and 40 degree pitch forward setpoint.	111
C-53 Fourth validation step maneuver with rate feedback 800 (PPRZ units) and 40 degree pitch forward setpoint.	111
C-54 Fifth validation step maneuver with rate feedback 800 (PPRZ units) and 40 degree pitch forward setpoint.	111
C-55 Sixth validation step maneuver with rate feedback 800 (PPRZ units) and 40 degree pitch forward setpoint.	112
C-56 Seventh validation step maneuver with rate feedback 800 (PPRZ units) and 40 degree pitch forward setpoint.	112
C-57 First validation step maneuver with rate feedback 800 (PPRZ units) and 40 degree pitch backward setpoint.	112
C-58 Second validation step maneuver with rate feedback 800 (PPRZ units) and 40 degree pitch backward setpoint.	113
C-59 Third validation step maneuver with rate feedback 800 (PPRZ units) and 40 degree pitch backward setpoint.	113
C-60 Fourth validation step maneuver with rate feedback 800 (PPRZ units) and 40 degree pitch backward setpoint.	113
C-61 Fifth validation step maneuver with rate feedback 800 (PPRZ units) and 40 degree pitch backward setpoint.	114
C-62 Sixth validation step maneuver with rate feedback 800 (PPRZ units) and 40 degree pitch backward setpoint.	114
C-63 First validation step maneuver with attitude feedback 3900 (PPRZ units) and 40 degree pitch forward setpoint.	115
C-64 Second validation step maneuver with attitude feedback 3900 (PPRZ units) and 40 degree pitch forward setpoint.	115
C-65 Third validation step maneuver with attitude feedback 3900 (PPRZ units) and 40 degree pitch forward setpoint.	116
C-66 Fourth validation step maneuver with attitude feedback 3900 (PPRZ units) and 40 degree pitch forward setpoint.	116

C-67	Fifth validation step maneuver with attitude feedback 3900 (PPRZ units) and 40 degree pitch forward setpoint.	116
C-68	Sixth validation step maneuver with attitude feedback 3900 (PPRZ units) and 40 degree pitch forward setpoint.	117
C-69	Seventh validation step maneuver with attitude feedback 3900 (PPRZ units) and 40 degree pitch forward setpoint.	117
C-70	Eighth validation step maneuver with attitude feedback 3900 (PPRZ units) and 40 degree pitch forward setpoint.	117
C-71	Ninth validation step maneuver with attitude feedback 3900 (PPRZ units) and 40 degree pitch forward setpoint.	118
C-72	First validation step maneuver with attitude feedback 3900 (PPRZ units) and 40 degree pitch backward setpoint.	118
C-73	Second validation step maneuver with attitude feedback 3900 (PPRZ units) and 40 degree pitch backward setpoint.	118
C-74	Third validation step maneuver with attitude feedback 3900 (PPRZ units) and 40 degree pitch backward setpoint.	119
C-75	Fourth validation step maneuver with attitude feedback 3900 (PPRZ units) and 40 degree pitch backward setpoint.	119
C-76	Fifth validation step maneuver with attitude feedback 3900 (PPRZ units) and 40 degree pitch backward setpoint.	119
C-77	Sixth validation step maneuver with attitude feedback 3900 (PPRZ units) and 40 degree pitch backward setpoint.	120
C-78	Seventh validation step maneuver with attitude feedback 3900 (PPRZ units) and 40 degree pitch backward setpoint.	120
C-79	Eighth validation step maneuver with attitude feedback 3900 (PPRZ units) and 40 degree pitch backward setpoint.	120
C-80	First validation step maneuver with attitude feedback 11700 (PPRZ units) and 40 degree pitch forward setpoint.	121
C-81	Second validation step maneuver with attitude feedback 3900 (PPRZ units) and 40 degree pitch forward setpoint.	121
C-82	Third validation step maneuver with attitude feedback 11700 (PPRZ units) and 40 degree pitch forward setpoint.	122
C-83	Fourth validation step maneuver with attitude feedback 11700 (PPRZ units) and 40 degree pitch forward setpoint.	122
C-84	Fifth validation step maneuver with attitude feedback 11700 (PPRZ units) and 40 degree pitch forward setpoint.	122
C-85	Sixth validation step maneuver with attitude feedback 11700 (PPRZ units) and 40 degree pitch forward setpoint.	123
C-86	Seventh validation step maneuver with attitude feedback 11700 (PPRZ units) and 40 degree pitch forward setpoint.	123
C-87	Eighth validation step maneuver with attitude feedback 11700 (PPRZ units) and 40 degree pitch forward setpoint.	123
C-88	Ninth validation step maneuver with attitude feedback 11700 (PPRZ units) and 40 degree pitch backward setpoint.	124

C-89	First validation step maneuver with attitude feedback 11700 (PPRZ units) and 40 degree pitch backward setpoint.	124
C-90	Second validation step maneuver with attitude feedback 11700 (PPRZ units) and 40 degree pitch backward setpoint.	124
C-91	Third validation step maneuver with attitude feedback 11700 (PPRZ units) and 40 degree pitch backward setpoint.	125
C-92	Fourth validation step maneuver with attitude feedback 11700 (PPRZ units) and 40 degree pitch backward setpoint.	125
C-93	Fifth validation step maneuver with attitude feedback 11700 (PPRZ units) and 40 degree pitch backward setpoint.	125
C-94	Sixth validation step maneuver with attitude feedback 11700 (PPRZ units) and 40 degree pitch backward setpoint.	126

List of Tables

5-1	Summary of reviewed control system research.	30
5-2	Summary of reviewed control system research.	31

Chapter 1

Introduction

Flapping Wing Micro Air Vehicle (FWMAV) research is a prolific research field, with many participants focusing on understanding how best to control these vehicles. These vehicles have been shown to be efficient forward flyers at the small scale in comparison to rotorcraft, while also offering the hovering capability [1]. Controlling these vehicles at the edge of their capability is difficult due to the flapping oscillations, the unusual mechanisms of generating the control moments, nonlinear aerodynamics, and changing control effectiveness depending on the mode of flight. The Micro Air Vehicle Laboratory (MAVLab) in the Aerospace Engineering department of Delft University of Technology has a significant involvement in this field, driving many concurrent past, present, and future projects related to flapping-wing robots [2, 3, 4].

One such project is the DelFly Transformer platform [5] (see Figure 2-1). It is a 29g tailless flapping-wing robot and as such, controlled flight is achieved using only the wings. The hovering flapping frequency is around 16.5 Hz. It is an X-wing configuration utilizing the clap-and-fling effect to increase thrust. The available control inputs are flapping frequency, dihedral/anedral angle, and wing root deflection for yaw moment generation. The research into this class of flying robots is in its very early stages and very few other such platforms exist that achieve stable flight [6, 7, 8]. What is more, the DelFly Transformer has shown outstanding promise in terms of agility and fast forward flight capability [5].

However, the DelFly Transformer prototype has so far been unable to fly in such a way as to fully use the thrust capability of the wings in forward flight due to developing dynamic oscillations at those speeds. Furthermore, the controller has shown instability at certain flight regimes like fast descents. This project aims to push the DelFly Transformer design further in terms of the achievable stable flight conditions as well as contribute information about flight-proven control systems to the body of engineering knowledge on tailless FWMAVs.

The first research goal of the project was to find out which control systems could stabilize the DelFly Transformer in hover and fast forward flight. The second goal was to find out if this

could be done with a single, invariable controller. Since many control systems depend on a model, either during analysis or application, it was decided to validate a simple longitudinal dynamics model for this platform. This process took a considerable portion of the project's time, but the effort was successful in the end in terms of the model being valid for the flight regimes that were to be studied for control system improvement purposes. Furthermore, the model formed the basis for changing the control system such that the platform was able to fly in hover and fast forward flight with the same, invariable controller. However, the project did not get to the stage of exploring different control system types or architectures entirely.

This report is divided into two parts. First, a scientific paper condensing the entirety of the work is presented in Part I. Then, the preliminary studies documenting the research efforts in more detail along with a thorough literature study is presented in Part II.

Part I

Paper

A minimal longitudinal dynamic model of a tailless flapping wing robot for control design

K.M.Kajak*, M.Karasek†, Q.P.Chu‡, G.C.H.E. de Croon§
Delft University of Technology, Kluyverweg 1, Netherlands

ABSTRACT

Tailless flapping wing micro air vehicles (FWMAVs) have the potential of providing efficient flight at small scale, with considerable agility. However, this agility also brings significant control challenges, which are exacerbated by the fact that the aerodynamics and dynamics of flapping wing robots are still only partly understood.

In this article, we propose a novel, minimal dynamic model that is not only validated with experimental data, but also able to predict the consequences of various important design changes. Specifically, the model captures the flapping cycle averaged longitudinal dynamics of a tailless flapping wing robot, taking into account the main aerodynamic effects. The model is validated for airspeeds up to 3.5 m/s (when the forward velocity starts to approximate the wing velocities). It successfully predicts the effects of changes to the center of mass and flight at different pitch angles. Hence, the presented model forms an important step in accelerating the control design of flapping wing robots - which can now be done to a greater extent in simulation. In order to illustrate this, we have used the model to improve our control design, resulting in a change of the maximal stable speed of the tailless DelFly Transformer from 4 m/s to 7 m/s.

1 INTRODUCTION

Flapping wing flight is rare in the context of man-made aircraft, but it is the only form of powered flight among biological fliers. For man-made aircraft, this form of flight is relevant at small scale for several reasons. Fixed wing flight is not suitable for tight quarters flight due to lack of hovering ability, whereas rotorcraft and flapping flyers can hover. Despite this, man-made flapping flyers are rare. Many designs have used aerodynamic dampers to achieve passive stability [1, 2, 3, 4], but tailless designs are more desirable due to more advanced agility. Examples of working tailless designs can be found in [5, 6, 7]. The inherent agility of tailless designs comes at the cost of inherent instability, requiring the wings and an active control system to provide stabilizing control moments [8, 9, 10, 11, 12]. In order to unlock the full potential in terms of agility, dynamic models would be of great use. However, due to the difficulty of flapping wing aerodynamics, such models

are currently still not accurate enough for any sensible control design.

There are multiple efforts to capture the aerodynamic forces acting on flapping wing vehicles, ranging from very complex to quite minimal models. Some work utilizes CFD simulations, e.g. [13, 14, 11], but it is costly in terms of time and effort to set up an accurate simulation. A very popular approach to aerodynamic modeling is the use of quasi-steady blade-element models, where forces on wings are approximated [15, 16, 17]. With these models, treating forces as independent from their time history is the key simplifying assumption. In this type of modelling it is still necessary to take into account flapping kinematics. An additional effect that needs to be accounted for with X-wing configured flappers such as the DelFly [18] is inter-wing interaction and the related clap-and-fling or clap-and-peel effect [19]. This mechanism is one of the more difficult effects to model due to its dependence on the exact movement of the wings [17]. There is yet a simpler class of models, modeling the average aerodynamic forces as linear damping with respect to body velocities [20, 21, 3, 22, 23]. So far, only [23] shows validation with real flight data, though limited to oscillations around the hover condition.

In this article, we propose a novel, minimal dynamic model that is not only validated with experimental data, but also able to predict the consequences of various important design changes. The DelFly Transformer tailless FWMAV prototypes [18] are used to gather flight data for validation. An average aerodynamic force model is extended with the Transformer's control moment generation mechanism and a longitudinal dynamic model is validated at flight conditions between hover and fast forward flight, for different center of mass locations, and for different controller parameters. Furthermore, the model is used to improve the control system of the DelFly Transformer. An appropriately expanded aerodynamic model and the results of a validation campaign are presented. The paper is organized in four parts. Section 2 presents the experimental setup utilized in the course of the validation campaign. Section 3 presents the structure of the developed dynamic model and also the identification of the actuator dynamics. Section 4 describes the open and closed loop model validation procedure and results, as well as presenting the controller architecture. Finally, Section 5 provides an overview of how the model was used to improve the flight controller of the DelFly Transformer prototype.

*Email address: karlmartin.kajak@gmail.com

†Email address: m.karasek@tudelft.nl

‡Email address: q.p.chu@tudelft.nl

§Email address: g.c.h.e.decroon@tudelft.nl

2 EXPERIMENTAL SETUP

The FWMAV used in this paper for flight tests is the DelFly Transformer of the MAVLab of TU Delft [18], seen in Figure 1. It has two separate flapping mechanisms for roll control,

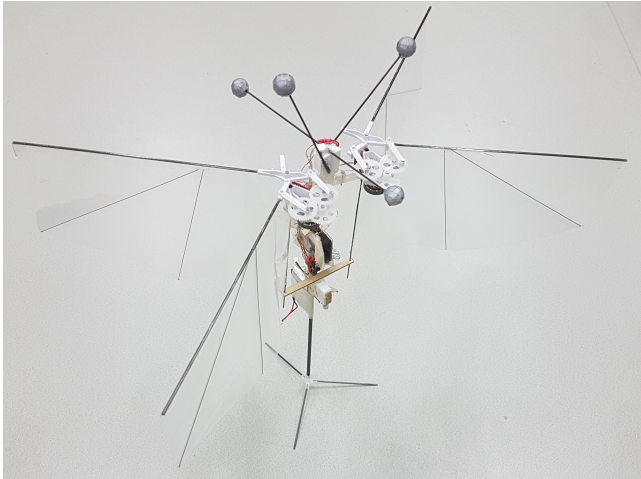


Figure 1: Second prototype of DelFly Transformer

each driving its own wing pair on the left and right side of the robot. A lift/power efficiency enhancement is achieved with the utilization of the clap-and-fling effect [19]. Furthermore, the opposite wing drag forces cancel, reducing body oscillations and the stress on the dihedral servo. Changing the dihedral angle changes the relative orientation of the wings and provides pitch control (see Figure 2). The bottom servo offers yaw control by deflecting the wing surfaces such as to tilt the thrust vector of the wings.

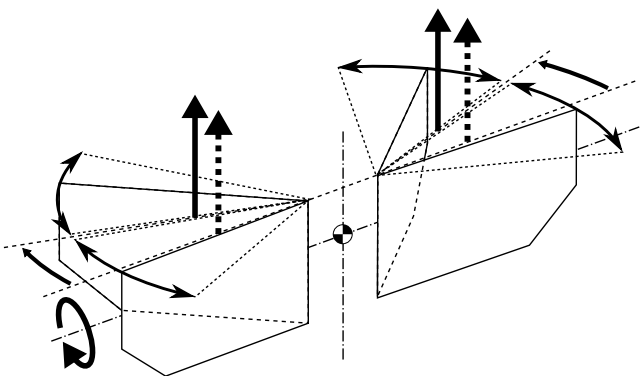


Figure 2: Pitch moment generation mechanism of the DelFly Transformer design.

An SD card is used for logging onboard flight data. Reflective marker balls are used with the OptiTrack motion capture suite. For more details on the design of the first prototype platform see [18]. The second prototype introduces some changes. Firstly, the autopilot is now a lighter (1.5 g) Lisa

MXS with more computational power. Both motor frequencies are logged onboard. The logging rate is also higher compared to Lisa S.

The flights were recorded in two ways. Onboard euler angle estimates and gyro readings along with the radio control set-points, controller reference generator outputs, controller outputs, and motor speeds were recorded onto the SD card at a rate of 100 Hz. Most flights were performed in the CyberZoo facility of the TU Delft Aerospace Engineering faculty. This is a 10x10x7 m volume equipped with 10 Prime 17W cameras from OptiTrack to form a motion capture system. The system tracks markers mounted on the robot and yields position and orientation information. Differentiation also yields information about velocities and accelerations. The OptiTrack data was captured at a rate of 200 Hz.

The flight results shown in Section 5 were gathered with a different OptiTrack system. There were 12 Flex13 cameras, recording at a rate of 120 Hz. The achieved tracking volume had a length of approximately 8 m in the flight direction.

Actuator dynamics were identified with the help of a ATI Nano17 Titanium 6 degree of freedom force/torque sensor and the first prototype DelFly Transformer, as presented in [18]. Compared to the second prototype shown in Figure 1, it has a slightly shorter fuselage and the autopilot board was a Lisa S by 1BitSquared. The platform was mounted onto the sensor and the forces, torques, onboard commands, and also motor frequencies were recorded via a National Instruments data acquisition FPGA.

In order to obtain data about the mismatch between the commanded and real dihedral angle, markers were also put on the gearboxes.

The wind tunnel used to collect data about trimmed flight was the Open Jet Facility (OJF) of Delft University of Technology Aerospace Engineering.

3 MODEL DEVELOPMENT

This section will provide the description of the dynamic model used in the work. Subsection 3.1 provides an analysis of the validity conditions of the model. Subsection 3.2 presents the full nonlinear state derivative equations that are used in the later sections for open and closed loop validation. Subsection 3.3 accounts the identification of the actuator dynamics.

3.1 Theoretical model validity conditions

In the following, the analysis of the stroke-averaged drag force is adapted from [3]. Assuming a wing that flaps with a sawtooth profile with its center of pressure at half the wing length, the constant wing velocity can be written as $U = 2\Phi f \frac{b}{4}$, where Φ is the flapping amplitude in radians, f is the flapping frequency, and b is the wingspan. If u is the freestream velocity, β a force coefficient, and assuming that the wing velocity due to flapping much higher than the free stream airspeed ($U \gg u$), the drag force during the

downstroke is $f_d = -\beta(U + u)^2$ and $f_d = \beta(U - u)^2$ during the upstroke. Since the two strokes have an equal time duration, the average force over a flapping cycle reduces to $\bar{f}_d = \frac{1}{2}\beta[(U - u)^2 - (U + u)^2] = -2\beta Uu$. This simplification does not hold when the assumption $U \gg u$ does not hold, because sign changes occur. Figure 3 compares the quadratic velocity component of the drag force with and without the simplifying assumption that flapping speed is much higher than the freestream airspeed. When the ratio of wing velocity due to flapping and the freestream velocity is higher than 1, the nonlinearity of the drag force becomes apparent. The results in the figure have been produced with $\Phi = 40^\circ$, $f = 16\text{Hz}$, and $b = 0.028\text{m}$.

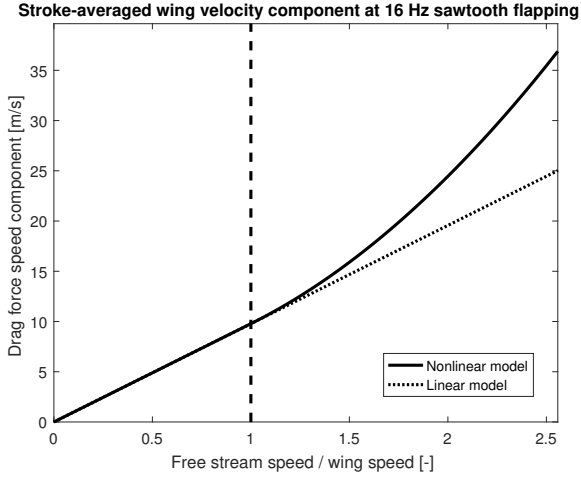


Figure 3: Comparison of simplified and non-simplified stroke-averaged absolute wing velocities during flapping at 16 Hz frequency with different freestream velocities.

3.2 Robot dynamic model

The first order average force models as seen in [20, 21, 3, 22, 23] were shown with the work of [23] to be valid for an analysis of a real robot in the near hover conditions. However, in fast forward flight, there is also a necessity to add a damping force along the thrust axis in order to trim the flight. The flapping flyer is considered rigid and the wings are considered to not have mass for the purposes of this work. This means that the center of mass is also considered to be a fixed location within the flapper body. The standard rigid body equations of motions can be used in this case [24]. The body and earth (flat, non-rotating) frame reference axes, the directional conventions, and other quantities of interest for the derivation of the aerodynamic model are given in Figure 4.

The longitudinal equations of motion of a rigid body are given in Equation 1 and 2.

$$m \begin{bmatrix} \dot{u} + qw \\ \dot{w} - qu \end{bmatrix} = mg_0 \begin{bmatrix} -\sin(\theta) \\ \cos(\theta) \end{bmatrix} + \begin{bmatrix} X \\ Z \end{bmatrix} \quad (1)$$

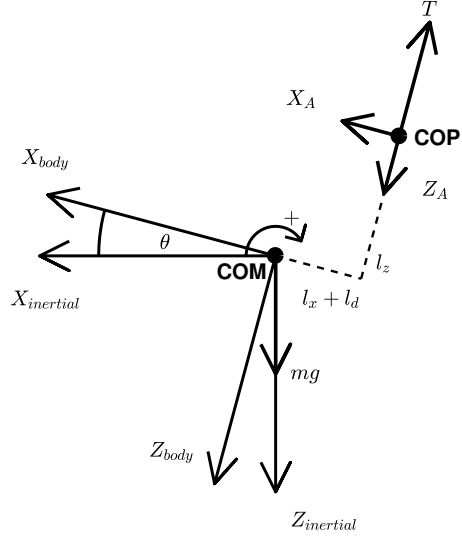


Figure 4: 2D longitudinal free body diagram of a flapping-wing MAV. COP - mean center of pressure, COM - mean center of mass.

$$\ddot{\theta} = \frac{M}{I_{yy}} \quad (2)$$

The lateral dynamics are not simulated within the scope of this investigation, though the extension of the model to all six degrees of freedom is possible. The models for longitudinal body frame aerodynamic forces X and Z and pitch moment M are given in Equations 3 to 7. Dihedral actuator states l_d and \dot{l}_d are marked in bold to highlight the terms specific to the control moment generation mechanism of the Transformer. Equations 3 and 4 express the air velocity of the wing along body axes X and Z , respectively.

$$u_{\text{COP}} = u - l_z \dot{\theta} - \dot{l}_d \quad (3)$$

$$w_{\text{COP}} = w + (\mathbf{l}_d + l_x) \dot{\theta} \quad (4)$$

$$X = -2b_x u_{\text{COP}} \quad (5)$$

$$Z = -2T - 2b_z w_{\text{COP}} \quad (6)$$

$$M = -Xl_z + Z(\mathbf{l}_d + l_x) \quad (7)$$

Each wing is considered to have an average center of pressure, where its mean thrust vector and damping forces act. Body force X is a linear damping force, opposing the wing center of pressure velocity u_{COP} along body axis X_{body} . Body force Z is the sum of the thrust of the two wings and a linear damping force, opposing the wing center of pressure velocity w_{COP} along body axis Z_{body} . The pitch moment M is a result of those forces acting at a distance from the center of mass. Note that the factor two in Equations 5 and 6 signifies the fact that two pairs of wings are present on either side of the robot. The term \dot{l}_d , related to the velocity of the actuator was included, because it had a non-negligible influence

on the dynamics. The parameters of the aerodynamic model are:

b_x, b_z - the aerodynamic force coefficients with respect to an air velocity component along body axis X and Z , respectively.

l_d - the linear displacement of the thrust vector/aerodynamic center from its neutral position.

l_z - the fixed linear offset of the thrust vector/aerodynamic center from the center of mass along the body axis Z .

l_x - the fixed linear offset of the wing neutral position from the center of mass along the body axis X .

T - thrust.

3.3 Actuator dynamics

The thrust to flapping frequency relationship was identified using the ATI Nano17 Titanium 6-DOF force/torque sensor. A single flapping mechanism from the second DelFly Transformer prototype was fixed into the sensor and the thrust force was measured at a variety of flapping frequencies. The thrust

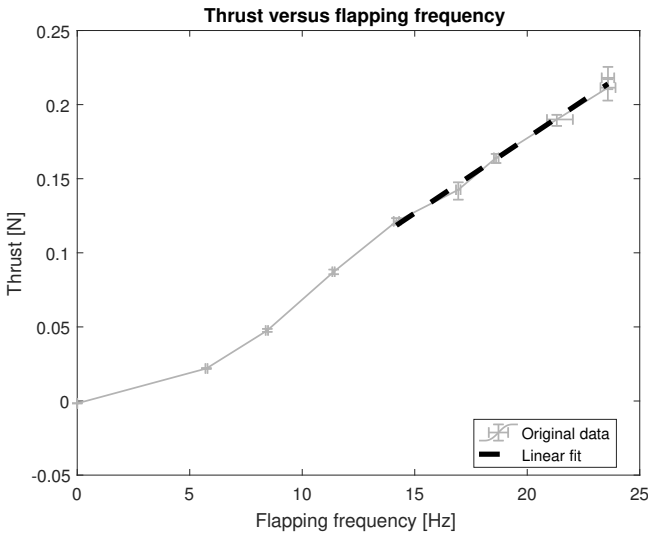


Figure 5: Thrust versus flapping frequency of the second prototype DelFly Transformer.

to flapping frequency relationship was found to be approximately linear near the neighborhood of operational flapping frequencies (~ 17 Hz in hover), and therefore a linear fit of this relationship was incorporated into the dynamic model. The actuator dynamics of the flapping frequency were determined from a different set of experiments on the force balance with the first prototype DelFly Transformer. A pre-programmed pulse train with a minimum 36.7 % a maximum 53 % throttle was sent to the motor controller. The

flapping frequency was recorded using the National Instruments FPGA, by counting the polarity changes of the electronic speed controller. A first order transfer function was estimated on the basis of the unfiltered flapping frequency measurements and a scaled PWM signal. The resulting transfer function is $H_{flap}(s) = \frac{12.56}{s+12.56}$. A simulation with the estimated transfer function is compared with the measurements in Figure 6. The first order function is a very good fit for the response.

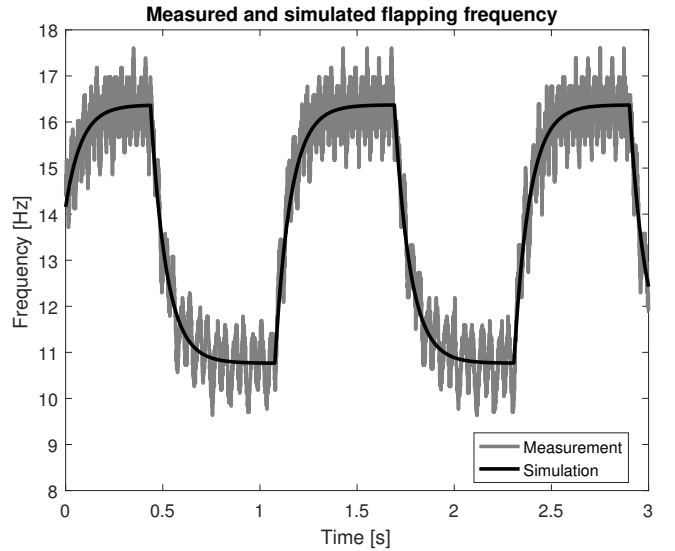


Figure 6: Identified first order flapping dynamics versus measurements.

The dihedral angle actuator dynamics were determined using the same setup as the flapping frequency dynamics, except a pulse train was sent to the dihedral angle servo. The minimum command was 28.2 % and the maximum 67.6 %. A second order transfer function was estimated based on the pitch moment measurement filtered with a fourth order Butterworth filter with a cutoff frequency of 10 Hz and a scaled PWM signal. A second order transfer function was chosen rather than a first order one because the response type resembles at least a second order system. The resulting transfer function is $H_{dihedral}(s) = \frac{554.2}{s^2+30.25s+554.2}$. A simulation of the pitch moment is compared with the filtered measurement in Figure 7. The lateral distance of the mean center of pressure of each wing from the center of mass is obtained as $l_y = \frac{M}{T \sin(\gamma)}$, where T is the thrust average over the whole two second measurement, M is the steady state of the filtered pitch moment achieved at the end of each pulse, and γ is the achieved dihedral angle during at the end of each pulse.

An additional effect was found to be influencing the dihedral angle of the wings, specific to the mechanical design of the DelFly Transformer. During maneuvers, the measured dihedral angle of the wings is different from the command. This is likely due to some mechanical play and/or elasticity, but it

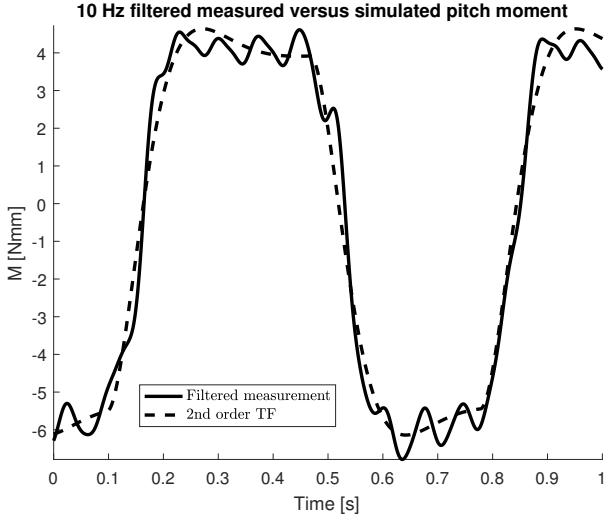


Figure 7: 10 Hz filtered measurement of the pitch moment versus estimated 2nd order transfer function.

could also be that the servo struggles against the aerodynamic loads in forward flight. Due to mechanical play being involved there is also evidence of hysteresis and random movement of the dihedral control mechanism within the allowance of this play. The actual angle of the dihedral differs from the commanded angle by an amount that correlates quite well with the body axis velocity u , as seen in Figure 8. Therefore, the simulations in the present work add a corrective factor on top of the dihedral.

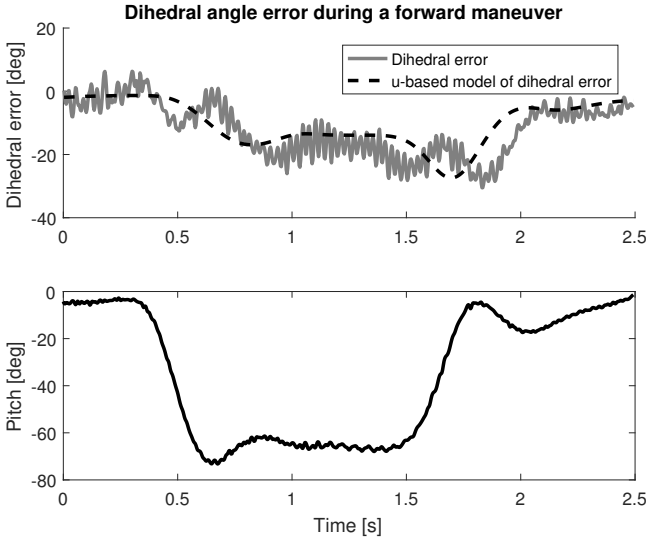


Figure 8: Comparison of measured and modeled hinge error.

The actuator dynamics as used in the present work are given

in Equations 8 to 14.

$$\ddot{\gamma}_1 = -2\zeta\omega_n\dot{\gamma}_1 - \omega_n^2\gamma_1 + \omega_n^2\gamma_c \quad (8)$$

$$\gamma_2 = \gamma_1 + c_{ucorr}\frac{\pi}{180}u \quad (9)$$

$$\dot{\gamma}_2 = \dot{\gamma}_1 + c_{ucorr}\frac{\pi}{180}\dot{u} \quad (10)$$

$$l_d = -l_y\sin(\gamma_2) \quad (11)$$

$$\dot{l}_d = -l_y\cos(\gamma_2)\dot{\gamma}_2 \quad (12)$$

$$\dot{f} = \frac{1}{\tau}(f_c - f) \quad (13)$$

$$T = 2(c_1f + c_2) \quad (14)$$

The definitions of the actuator dynamics parameters are as follows:

γ_c - Dihedral angle command in radians (bounded between $-/+ 18$ degrees).

f_c - Flapping frequency command in Hz.

ω_n - Natural frequency of second order dihedral angle servo dynamics.

ζ - Damping ratio of the second order dihedral angle servo dynamics.

γ_1 - Dihedral angle before velocity correction.

γ_2 - Dihedral angle after velocity correction.

c_{ucorr} - Dihedral angle velocity correction coefficient.

l_y - The fixed offset of an individual wing's thrust and aerodynamic force vectors from the center of mass along the body axis Y .

l_d - The variable linear offset of the thrust vector from the wing neutral position.

τ - Time constant of the first order flapping frequency dynamics.

c_1, c_2 - Coefficients of the linear thrust to flapping frequency shown in Figure 5.

3.4 Obtaining force coefficients

Due to the fact that a stable flying robot was available, the force coefficients were obtained from flight data. Alternatively, force coefficients b_x and b_z can be obtained via, for example, damped pendulum tests as in [23] or even with wind tunnel tests.

The first prototype of the DelFly Transformer was flown by a human pilot at the mouth of an open jet wind tunnel in trim condition at various velocities between 1 - 2.4 m/s. The velocity reading of the wind tunnel was not reliable below this range and above that it becomes difficult for the pilot to keep

the robot in steady flight in front of the center of the contraction section output in the open jet test section. Assuming zero accelerations in Equations 5 and 6, one can substitute the measured values of velocity and pitch angle to obtain the force coefficients necessary to trim the flight. The generated thrust also has to be known, of course. For this, the relationship shown in Figure 5 was used with the flapping frequency recorded by the autopilot to approximate thrust. For each trim condition the measured velocity, pitch angle, and flapping frequency data was averaged over a period of several seconds, depending on the duration of relatively steady flight that the pilot was able to achieve. These averaged quantities were then used to fit a least squares linear solution to the trim points. The solutions represent the linear force coefficients b_x and b_z in Equations 5 and 6. A comparison of the obtained linear model and the body velocities measured at trim conditions in the wind tunnel is shown in Figure 9. The measured

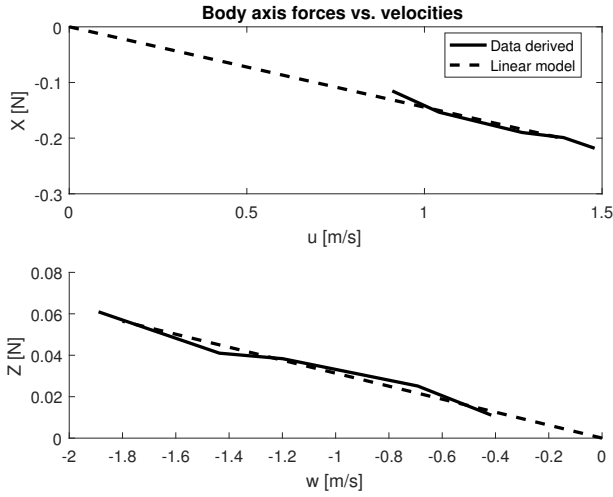


Figure 9: Measured and linearly modeled forces on the first DelFly Transformer prototype during trimmed flight conditions

data does not cover behavior of coefficient b_x below 0.9 m/s for body velocity u , but this force coefficient has been demonstrated to be dominantly linear at these velocities in the work of [3, 23]. Force coefficient b_z is also nearly linear in the covered velocity range as predicted by analytical formulations in [12] for the case of vertical climb/descent.

4 MODEL VALIDATION

This section presents the validation efforts of the open and closed loop model. Subsection 4.1 deal with the procedure and results of the open loop validation. The controller architecture is given in subsection 4.2. Subsection 4.4 accounts the closed loop validation procedure and Subsection 4.5 presents the results.

4.1 Open loop validation

The state derivatives and the dihedral angle output from the developed model were compared to data recorded in flight, as seen in Figure 10. It is important to note that in this test case the states of the model are not simulated, but the states recorded via the OptiTrack motion capture system are plugged into Equations 1 to 7. The resulting state derivatives are then compared to filtered state derivatives derived from OptiTrack data recorded of a flight of the first DelFly Transformer prototype. The derived state derivatives were filtered with a fourth order Butterworth filter with a cutoff frequency of 5 Hz. This filter cutoff frequency is low enough to exclude flapping oscillations, but high enough to show the body dynamics. Qualitatively speaking, all state derivatives and even the dihedral angle follow their expected trends well and it was decided to move on to validation of the closed loop simulation. The parameters used here are the same as in Table 1, except the parameter l_z , which is 11 mm in this case. This is because the first prototype had its center of mass closer to the aerodynamic center. Further it is important to note that the actuator dynamics transfer function bandwidth had to be increased in order to match the peaks in the acceleration. While the originally identified transfer function had a natural frequency of approximately 24 rad/s, it had to be increased to 40 rad/s to achieve this goal (see Figure 11).

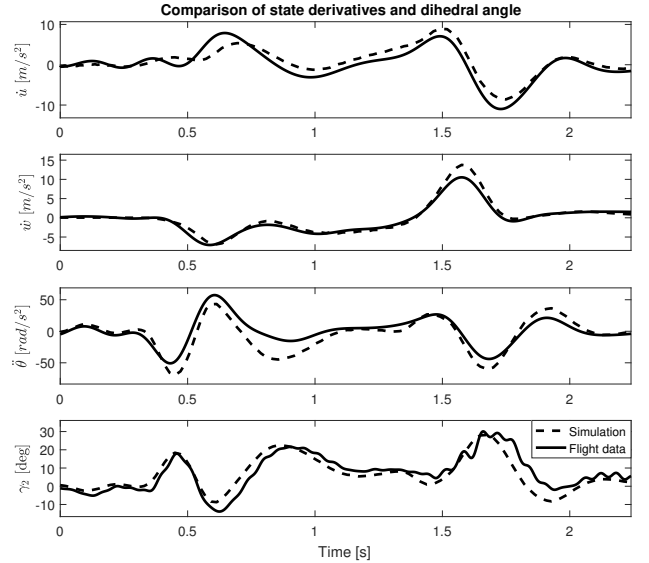


Figure 10: State derivatives and hinge angle (flight with first prototype DelFly Transformer)

4.2 Controller

The DelFly Transformer prototypes are in this work being stabilized by a fixed-gain parallel feedback architecture, which involves attitude and rate feedback. This is the standard controller architecture in the open-source Paparazzi UAV version

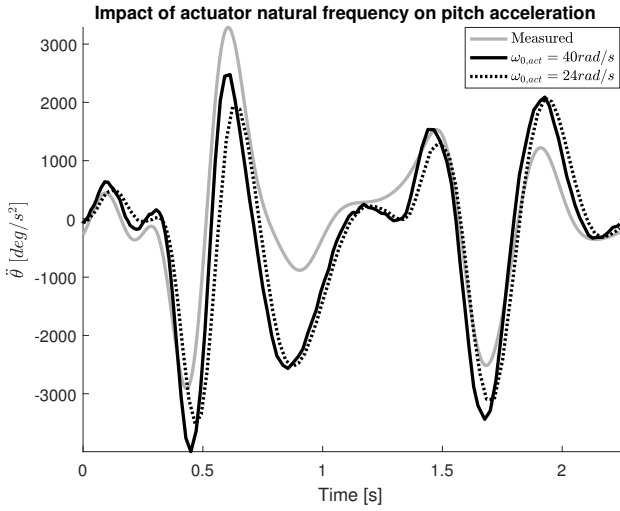


Figure 11: Comparison of effect of 24 and 40 rad/s actuator natural frequency on pitch acceleration

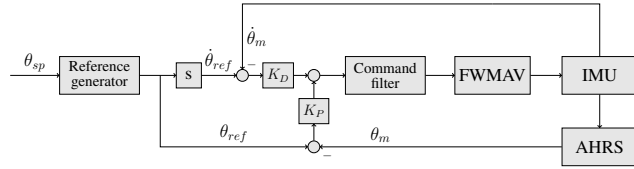


Figure 12: Controller architecture

5.10 autopilot software, with the addition of the command filter. The controller layout is shown in Figure 12. The final command is filtered by a second order biquad implementation filter before being sent to the actuators due to the noise in the gyro rate measurements and AHRS attitude estimates. The setpoint is smoothed via a second order reference generator, which generates reference attitudes and rates.

4.3 Model parameter identification

Before the model is analyzed for fitness, the parameters need to be identified. The aerodynamic parameters b_x and b_z were kept the same as for the first prototype robot, for which it was possible to extract approximate trim curve data from flights in a wind tunnel. The parameter l_x in Equations 5 to 7 is zero for a configuration where the center of mass is aligned with the line of action of the thrust vector, meaning the platform is well trimmed. The mass can be measured. The two remaining parameters that have to be identified is the moment of inertia and the parameter l_z . For this purpose, a particle swarm global optimization routine was used to minimize the sum of the squares of the residuals between the simulation output pitch angle and OptiTrack-recorded pitch angle. The velocity states were excluded from the optimization as l_z and the moment of inertia should mainly influence attitude dynamics. Thus a complicated cost function with weights was also

avoided. The maneuvers that were used for this are given in Figure 13. These maneuvers were chosen for several reasons. Firstly, the OptiTrack recordings had no tracking losses. Furthermore, there were minimal differences between the IMU and OptiTrack attitude estimates. The set of maneuvers also has a certain variety - there are maneuvers of various durations and amplitudes. Lastly, the maneuvers achieve a significant pitch attitude, which hopefully minimizes the effects of the measurement errors and the mechanical imperfections and maximizes the contribution of the aerodynamic model to the dynamic behavior. A summary of all parameter values used in the simulations for this section is given in Table 1.

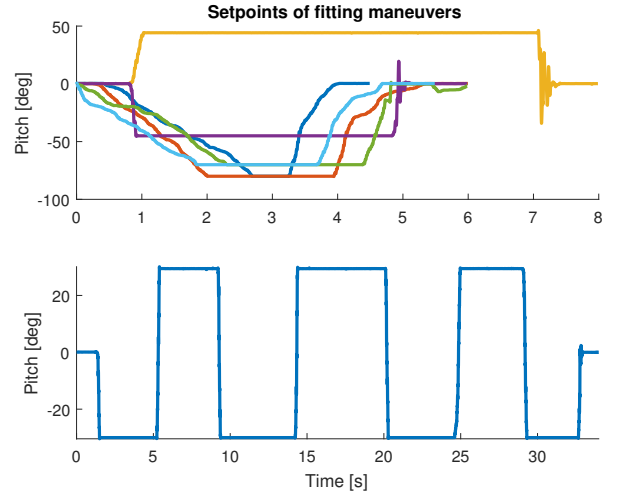


Figure 13: Model fitting maneuver setpoints

4.4 Closed loop validation procedure

The recorded flight data from a second prototype DelFly Transformer was used to validate the closed loop simulation. Datasets were gathered with three goals in mind. The first dataset was collected to confirm that the effects of physical changes to the flying prototype such as the relative positioning of the center of mass to the center of pressure reveal a similar effect in the physical model. The second dataset was collected in order to confirm that the model predicts flight at a variety of pitch angles. A third dataset was collected to validate the performance of the model with respect to changes in the control system parameters. For each test condition, at least 5 maneuvers were executed with the DelFly Transformer. Each maneuver was also simulated using the onboard recordings of pitch command as model input, while the model throttle input was fixed at the hovering trim level. The mean and the standard deviation was calculated for the measured and simulated states of each maneuver. The flights of all datasets included step-like pitch commands, limited to various maximum pitch setpoints. All maneuvers were executed starting from a near-hover condition. These commands were given manually

Table 1: Overview of parameters of closed loop simulation used in validation maneuvers of Section 4.4

Parameter	Value	Unit	Definition	Source
b_x	0.0722	$[N\frac{s}{m}]$	Aerodynamic damping coefficient for body axis X .	Obtained from flight data (Section 3.4).
b_z	0.0157	$[N\frac{s}{m}]$	Aerodynamic damping coefficient for body axis Z .	Obtained from flight data (Section 3.4).
l_x	0	$[mm]$	Nominal position of thrust T and damping force Z from center of mass along body axis X .	Assumed 0 for well balanced platform.
l_y	81	$[mm]$	Nominal position of a single wing's thrust T and damping force Z from center of mass along body axis Y .	Derived from force balance tests (Section 3.3).
l_z	27.1	$[mm]$	Nominal position of damping force X from center of mass along body axis Z .	Flight data fitting (Section 4.4).
I_{yy}	1.2595e-4	$[kgm]$	Moment of inertia about body axis Y .	Flight data fitting (Section 4.4).
ζ	0.634	$[-]$	Dihedral actuator 2nd order transfer function damping ratio.	Force balance tests (Section 3.3).
ω_n	40	$[\frac{rad}{s}]$	Dihedral actuator 2nd order transfer function natural frequency.	Manually tuned during open loop validation (Section 4.1).
c_{ucorr}	10	$[deg\frac{s}{m}]$	Dihedral angle correction for body velocity u .	Determined from flight data (Section 3.3).
c_1	0.0114	$[\frac{N}{Hz}]$	Slope of linear thrust to flapping frequency relationship.	Determined from force balance data (Section 3.3).
c_2	-0.0449	$[N]$	Zero frequency thrust of the linear thrust to flapping frequency relationship.	Determined from force balance data (Section 3.3).
τ	0.0796	$[s]$	Time constant of 1st order flapping frequency actuator dynamics.	Determined from force balance data (Section 3.3).
K_P	0.5105	$[-]$	Attitude feedback gain.	Flight prototype.
K_D	0.0654	$[s]$	Rate feedback gain.	Flight prototype.
f_{cut}	15	$[Hz]$	Cutoff frequency of the second order Butterworth low-pass digital biquad command filter.	Flight prototype.

to maintain control of the robot at all times and to avoid flying into the sides of the motion tracking arena. Figure 14 shows a comparison of remote controlled setpoints and the resulting onboard references for a set of 45 degree pitching maneuvers. The maneuvers were aligned in time at the point where their pitch references (not remote controlled setpoints) reached 10 degrees. There is not a significant difference in the generated references. This is also confirmed by the fact that an averaged maneuver (over several attempts at the same maneuver) actually resembles individual maneuvers well.

4.5 Closed loop validation results

This section presents a comparison of the simulation output and flight data. The standard deviation and mean of the measured state as well as the simulation is plotted for each dataset. Each dataset contains five or more maneuvers.

The first dataset was collected to study the change of dynamic behavior with respect to changes to the physical parameters of the platform. Three flights were recorded

while executing 30 degree maximum pitch setpoint step maneuvers. One flight was executed in a well balanced configuration (thrust aligned with center of mass to trim the robot for hovering), another one in a "front heavy" configuration (c.g. approximately 4.8 mm toward the nose, causing a nose heavy situation), and lastly a "bottom heavy" configuration (c.g. approximately 6 mm lower than in the balanced configuration).

A comparison of the actual flown and simulated maneuvers with a balanced center of mass, a nose heavy center of mass, and a center of mass that is further away along the fuselage compared to the nominal (bottom heavy) are shown in Figures 15. The simulated and real robot both behave as expected. The nose heavy configuration dips in furthest into the pitch maneuver and has a steady state error, tending to pitch more than commanded. The bottom heavy configuration has the most trouble achieving its setpoints, which is expected, since the control moment is competing against a stronger stabilizing aerodynamic moment due to forward flight. Furthermore,

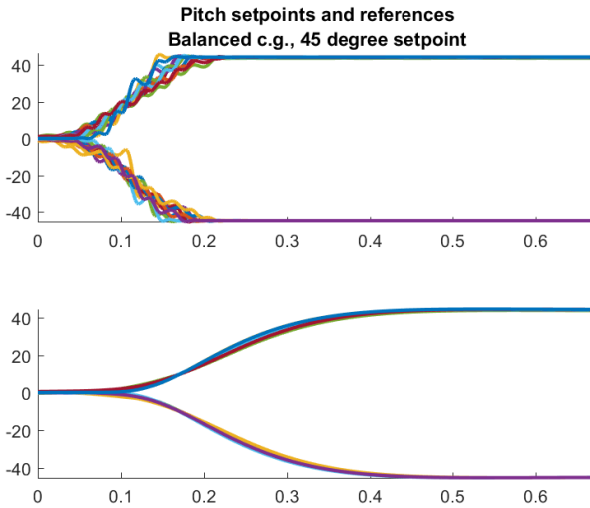


Figure 14: Comparison of 45 degree pitching maneuver setpoints and references

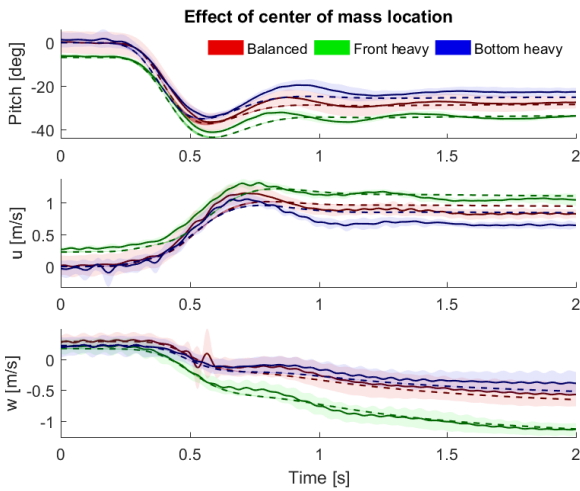


Figure 15: Averaged 30 degree forward pitching maneuvers in balanced/nose heavy/bottom heavy configurations. Solid lines correspond to mean measured states, dashed lines to mean simulated states. Color belts around lines correspond to standard deviation.

it has no significant steady state error. The balanced configuration also has no significant steady state error. There is some higher order oscillation that is not captured by the model, but it is not of a high amplitude.

The second dataset was collected to show the representativeness of the model at different regimes of flight, whether it is near hover or fast forward flight. Figure 16 shows the comparison of the pitch attitude of the simulation and the real robot in response to commanding pitch step maneuvers of various amplitudes. The pitch angle seems to be represented rather

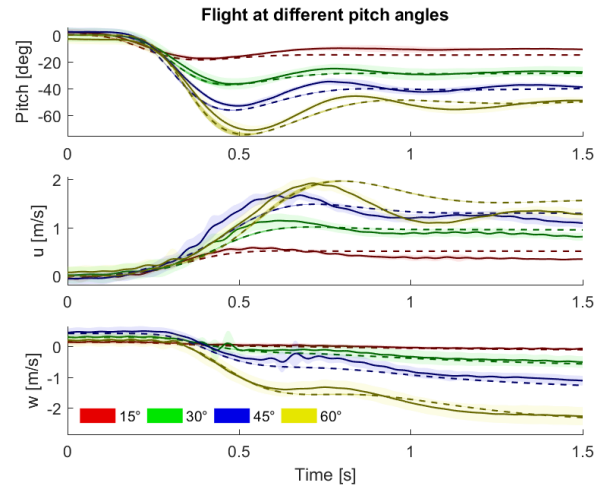


Figure 16: Comparison of forward pitching maneuvers in balanced configuration. Solid lines correspond to mean measured states, dashed lines to mean simulated states. Color belts around lines correspond to standard deviation.

well for all maneuvers, less so for the 15 degree pitching maneuver. The body velocities match rather well also, with the oscillating errors coming from the higher order oscillations in pitch angle that are not captured by the model. The real damping force seems to be stronger at 60 degree pitch attitude, as body velocity u is overestimated by the model.

The final dataset consists of tests performed with varying pitch attitude and rate feedback gains, as well as the command filter cutoff frequency. A comparison of flights with different attitude feedback gains is given in Figure 17. The

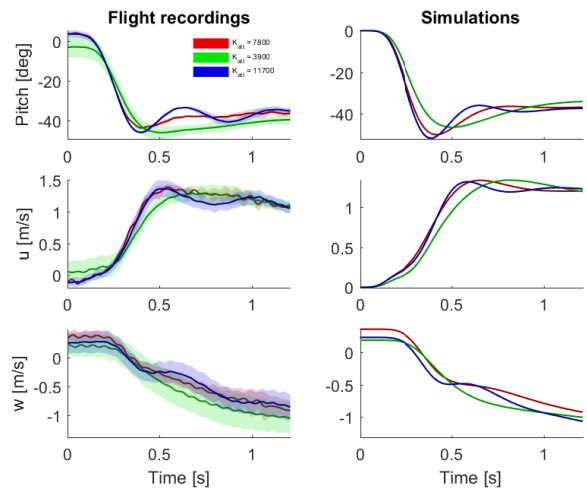


Figure 17: Comparison of flights with different attitude feedback gains. Solid lines correspond to mean states. Color belts around lines correspond to standard deviation.

model correctly predicts more lax pitch angle following with a weaker gain and additional oscillations from a gain that is too high. Figure 18 shows a comparison of flights performed with different rate feedback gains. The model correctly pre-

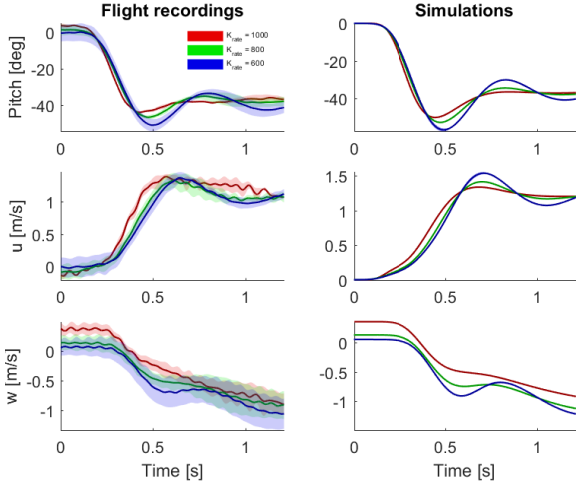


Figure 18: Comparison of flights with different rate feedback gains. Solid lines correspond to mean states. Color belts around lines correspond to standard deviation.

dicts the trend of higher damping seen in flight from a higher gain and the introduction of transient oscillations at lower gain levels. The same study was conducted with the command filter cutoff frequency. Figure 19 shows a comparison of flights and simulations with respect to changes in the command filter cutoff frequency. The model again seems to cor-

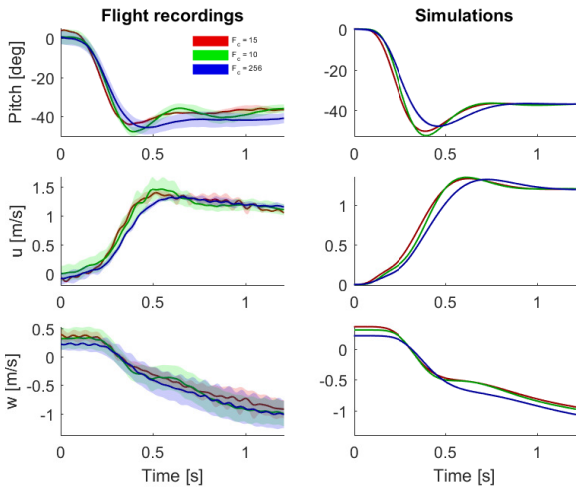


Figure 19: Comparison of flights with different command filter cutoff frequencies. Solid lines correspond to mean states. Color belts around lines correspond to standard deviation.

rectly predict the trend, though the actual robot seems closer to instability overall. One thing that is not captured here is the behavior change due to noise at higher cutoff frequencies. According to the model the best solution is not to have the filter (fastest control loop), but that is not likely to be a viable solution with the vibrations introduced to the sensor due to the flapping. With the present mechanical design, the dihedral actuator was already wobbling back and forth at a cutoff of 256 Hz (considerably higher than the nominal 15 Hz) and it starts to wobble at a much lower frequency even. Therefore, a 15 Hz filter has been used to avoid unnecessary inputs to the servo, while keeping the delay low enough for stabilization.

4.6 Analysis of model performance

In general, despite its simplicity, the model was able to capture the dominant dynamic effects very well and the simulated states were in a good agreement with the measurements. The small differences observed can be attributed to unmodeled dynamics, imperfect measurement techniques, and imperfect testing conditions. These are:

- There is a time-dependent error between the IMU attitude estimate and the OptiTrack-based attitude measurement, which can at times reach a magnitude of up to 5 degrees. It is thought to be the effect of noise on the attitude estimation algorithm, but this has not been studied systematically. This error causes the control signal to sometimes be stronger or weaker, depending on the sign of the pitch angle error.
- There is time-independent error of a few degrees between the IMU attitude estimate and the OptiTrack measurement in a steady, non-flapping, non-flying state across the datasets. This is thought to come from the misalignment of the body frame as defined in OptiTrack, the possible plastic deformation of the marker appendages due to handling and crashes, and the bias estimations of the onboard attitude estimation algorithm.
- The listing of unmodeled dynamics in an exhaustive way is not possible, but some of them have revealed themselves. Firstly, there is a mechanical looseness in the load path between the dihedral angle servo and the wings. An elastic deformation and the use of a proportional feedback of the servo actuator controller is modeled well by a linear dependence on u , but a looseness should be modeled by a hysteresis term. The hysteresis model is not included in this work. Secondly, the thrust generated is somehow influenced by the flight states, because of the changing conditions of how much air is being ingested. This would of course have an effect on the attitude dynamics, as predicted by the current model.

- The maneuvers have not been executed from a perfectly still position. The air in the testing area is not always still, which may cause some chaotic drifting at times, especially at very low speeds. Furthermore, the ability to hover in a perfectly still manner is degraded by the occasional drifting of the IMU attitude estimate (probably due to noise), the mechanical looseness of the dihedral actuator, as well as the subtle wear of the dihedral actuator over time.
- The last point is related to the imperfections of the platform itself. Firstly, the rotational axes of the wings are not perfectly aligned with the wing root attachments below. This has some effect on tilting the wing plane. Some of the thrust might not be aligned with the fuselage. Furthermore, the model assumes that the wing plane normal is perpendicular to the fuselage. This would show up as a trim condition not aligned with the fuselage and as an effectively different angle of attack from what the model would predict. Lastly, the assembly and repairs of the components of the craft is a delicate process that causes manufacturing variations and evolution of the aerodynamic characteristics over time as wing tears are fixed, mechanism components replaced, and so on. For example, the dihedral angle controlling servo gearing tends to degrade over time as it is subjected to harsh pitch maneuvers. This leads to odd pitching dynamics before the gearing breaks. Though care was taken to minimize all of these effects within the collection of datasets, the Transformer prototype is still delicate in this respect.

5 CONTROLLER IMPROVEMENT FOR FAST FORWARD FLIGHT

The model was further used to determine a better controller for the DelFly Transformer. The initial pitch stability performance of the DelFly Transformer was such that a divergent pitch oscillation would develop as the pilot gave a maximum thrust command along with a 70 degree forward pitch command. This command is such that the platform in reality flies level with the ground. This phenomenon was captured with the OptiTrack motion capture system. Figure 20 shows the pitch attitude and speed during this maneuver. The motion tracking data has limited coverage, since the platform flies quickly through a limited tracking area. During the maneuver, the aircraft develops a pitch oscillation with an amplitude of approximately 30 degrees and a frequency of approximately 1 Hz.

It was discovered that an increased rate feedback gain would improve the stability of the closed loop simulation in fast forward flight. In order explain this, the closed loop model was linearized at a trim condition in fast forward flight between the reference generator output and pitch rate output in order to examine the influence of the rate feedback on the stability of pitch rate. The trim point corresponds to the eventual

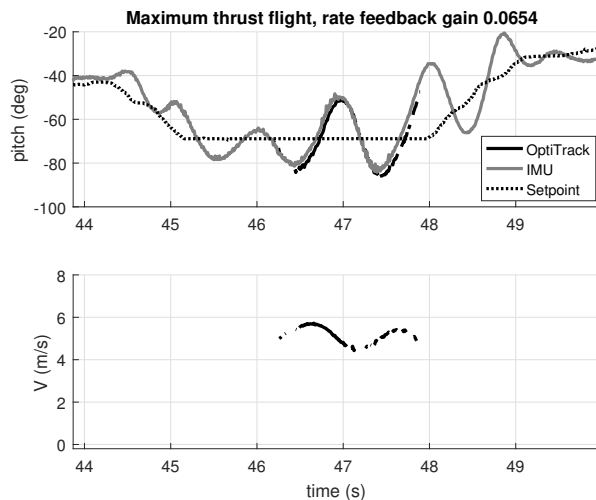


Figure 20: Pitch oscillation developing at full thrust with rate feedback gain of 0.0654.

steady state condition of the model in response to a 70 degree forward pitch command and a full thrust command at 22 Hz flapping frequency. This condition lies outside of the range of flight conditions validated in Section 4, where the maximum speed at 60 degree forward flight was approximately 3 m/s. The flight prototype, with this command, flies level to the horizontal at around 6 m/s. The simulation, with this command, achieves 7.6 m/s with a climb rate of 3.4 m/s. Clearly, the trim state is no longer accurately represented at this flight condition, as the analysis in Section 3 also showed. However, as the following analysis of the linearized closed loop model shows, the evolution of the system dynamics with rising speeds is still helpful for determining the appropriate set of gains for stable flight.

The values of the states and inputs corresponding to the linearization point are given in Table 2.

State/Input	Value	Unit
u	1.5471	m/s
w	-7.4546	m/s
θ_{ref}	-70	deg
$\dot{\theta}_{ref}$	0	deg/s
$\dot{\theta}$	0	deg/s
θ	-51.4974	deg
f	22	Hz
$\dot{\gamma}$	0	deg/s
γ	24.9174	deg

The z-plane poles and zeros shift with a change of the rate feedback gain, as shown in Figure 21. With the original rate feedback gain of 0.0654, the system poles that correspond to the 1 Hz oscillation seen in flight are unstable. Increasing the gain to 0.1635 stabilizes these poles, while the actuator dynamics poles become less damped. This specific number originated from flight tests where the rate feedback gain was progressively increased rather than from an analysis of the linearized system. A slightly higher gain could be more suitable as the damping ratio would be equal for the oscillatory actuator and aerodynamic poles of the linear system.

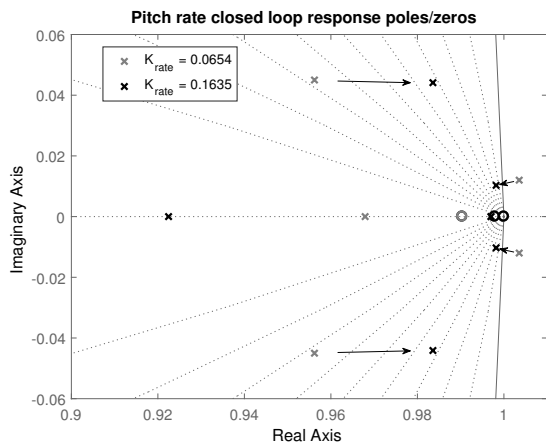


Figure 21: Shifting of z-plane system poles with increasing rate feedback gain.

The results of the nonlinear closed loop simulation with this rate feedback gain are shown in Figure 22. The platform is initially commanded to track zero pitch and 16.5 flapping frequency, which corresponds to the hovering frequency. Then, the thrust command is maximized and the pitch attitude setpoint is changed to -70 degrees simultaneously. The developing oscillation with the weaker rate feedback gain also has a 1 Hz frequency as seen in flights with the prototype. The oscillation is worsened by saturation of the actuator command bounds. The higher rate feedback gain smooths out the pitch response and avoids saturation of the actuator command. The rate feedback gain was increased to 0.1635 on the prototype DelFly Transformer as well. A maximum throttle level flight was conducted through the motion capture area again. The resulting flight is shown in Figure 23. The pitch attitude is stable and damped and as a result the robot also reaches stable speeds as high as 6.7 m/s during the recorded maneuvers. What is more, the higher gain stabilizes the robot well in hover also, though worse than before.

The model was helpful in determining the necessary changes to the controller to obtain a fixed gain controller for the DelFly Transformer that stabilizes flight in conditions ranging from hover to 6.7 m/s. However, there are notable dif-

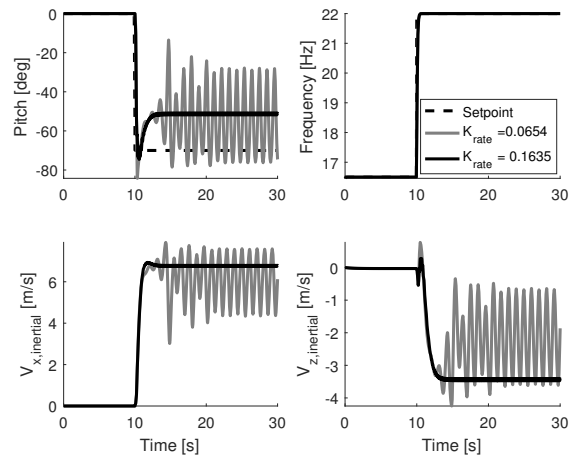


Figure 22: Comparison of effect of different rate feedback gains during a maximum thrust, 70 degree forward pitch setpoint maneuver.

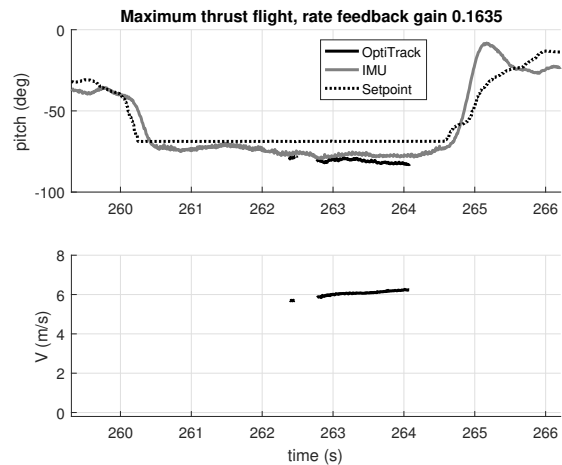


Figure 23: Stable full thrust level flight with rate feedback gain of 0.1635.

ferences between the flight conditions of the model and the prototype Transformer at these fast speed conditions. Firstly, the trim pitch angle of the model in response to a 70 degree forward pitch setpoint and maximum flapping frequency of 22 Hz is -51.5 degrees whereas the real robot even overshoots the command to a -78 degrees at times - a nearly 30 degree difference. Furthermore, while the model achieves a similar horizontal speed of 6.8 m/s, it also climbs vertically at a near 3.4 m/s, giving a total velocity of approximately 7.6 m/s. A common assumption that is made in work utilizing average flapping force models is that the speed of the wing due to flapping is much faster than the flight velocity [20, 21, 3, 22, 23]. At its maximum speed, the DelFly Transformer flaps

at about 22 Hz and its wing span is 35 centimeters, yielding a wing tip velocity of approximately 4 m/s assuming a saw-tooth flapping profile. Clearly, this assumption is violated in the tests conducted in this work. In order to more accurately study the flight of tailless flapping wing platforms at these forward speeds, the aerodynamic model has to be expanded beyond linear forces.

6 CONCLUSIONS AND RECOMMENDATIONS

A longitudinal dynamic average force model for a tail-less flapping wing micro air vehicle was developed and validated for flight conditions between hover and forward flight, different center of mass locations, and controller parameters. Furthermore, it was used to improve the flight controller of the prototype DelFly Transformer, yielding a fixed gain controller that stabilizes flight in hover and at forward flight speeds up to 6.7 m/s.

Firstly, the proposed model predicts state derivatives recorded during real flights with the DelFly Transformer well. More importantly, it was also shown to predict well the trends in the longitudinal dynamic states of a closed loop simulation with various center of mass positions, various controller parameters, and also in terms of flight at various forward attitude levels. However, at speeds near and beyond the maximum wing tip velocity, the trim pitch angle and speed of the model developed a significant difference with respect to the flight of the DelFly Transformer prototype. Nevertheless, the dynamic trend shown by the model was informative enough to help improve the flight controller.

Further research should look into the best choice of maneuvers to identify the model parameters from flight data in case one has access to a stable flight platform. Moreover, it should be studied to what extent the model is useful in case the user does not have a stable platform yet and needs to gather all parameters from non-flight tests. Furthermore, the actuator dynamics for the dihedral actuator should be studied with data recorded in flight to compare the difference with static measurements on the force balance. This is necessary to determine the optimal way of obtaining the dihedral angle dynamics as the static tests employed in Section 3.3 resulted in dynamics with a bandwidth that was too low. Also, modifications to the force model should be sought that could improve the representative accuracy at flight speeds past the maximum wing tip velocity.

REFERENCES

- [1] G. C. H. E. de Croon et al. "Design, aerodynamics, and vision-based control of the DelFly". In: *International Journal of Micro Air Vehicles* 1.2 (June 2009), pp. 71–97.
- [2] Charles Richter and Hod Lipson. "Untethered Hovering Flapping Flight of a 3D-Printed Mechanical Insect". In: *Artificial Life* 17.2 (Apr. 2011), pp. 73–86.
- [3] Z. E. Teoh et al. "A hovering flapping-wing microrobot with altitude control and passive upright stability". In: *2012 IEEE/RSJ International Conference on Intelligent Robots and Systems*. IEEE, Oct. 2012, pp. 3209–3216.
- [4] Quoc-Viet Nguyen, Woei-Leong Chan, and Marco De-biasi. "An insect-inspired flapping wing micro air vehicle with double wing clap-fling effects and capability of sustained hovering". In: *Bioinspiration, Biomimetics, and Bioreplication 2015* © 2015 SPIE. Ed. by Akhlesh Lakhtakia, Mato Knez, and Raúl J. Martín-Palma. Mar. 2015.
- [5] Matthew Keennon, Karl Klingebiel, and Henry Won. "Development of the Nano Hummingbird: A Tailless Flapping Wing Micro Air Vehicle". In: *50th AIAA Aerospace Sciences Meeting including the New Horizons Forum and Aerospace Exposition*. January. Reston, Virginia: American Institute of Aeronautics and Astronautics, Jan. 2012, pp. 1–24.
- [6] Pakpong Chirarattananon, Kevin Y. Ma, and Robert J. Wood. "Perching with a robotic insect using adaptive tracking control and iterative learning control". In: *The International Journal of Robotics Research* 35.10 (Sept. 2016), pp. 1185–1206.
- [7] Hoang Vu Phan, Taesam Kang, and Hoon Cheol Park. "Design and stable flight of a 21g insect-like tailless flapping wing micro air vehicle with angular rates feedback control". In: *Bioinspiration & Biomimetics* 12.3 (Apr. 2017), p. 036006.
- [8] Mao Sun, Ji Kang Wang, and Yan Xiong. "Dynamic flight stability of hovering insects". In: *Acta Mechanica Sinica* 23.3 (June 2007), pp. 231–246.
- [9] Imraan Faruque and Sean J. Humbert. "Dipteran insect flight dynamics. Part 1 Longitudinal motion about hover". In: *Journal of Theoretical Biology* 264.2 (May 2010), pp. 538–552.
- [10] Imraan Faruque and Sean J. Humbert. "Dipteran insect flight dynamics. Part 2: Lateral-directional motion about hover". In: *Journal of Theoretical Biology* 265.3 (Aug. 2010), pp. 306–313.
- [11] Na Gao, Hikaru Aono, and Hao Liu. "Perturbation analysis of 6DoF flight dynamics and passive dynamic stability of hovering fruit fly *Drosophila melanogaster*". In: *Journal of Theoretical Biology* 270.1 (Feb. 2011), pp. 98–111.
- [12] Bo Cheng and Xinyan Deng. "Translational and Rotational Damping of Flapping Flight and Its Dynamics and Stability at Hovering". In: *IEEE Transactions on Robotics* 27.5 (Oct. 2011), pp. 849–864.

- [13] Mao Sun and Ji Kang Wang. “Flight stabilization control of a hovering model insect”. In: *Journal of Experimental Biology* 210.15 (Aug. 2007), pp. 2714–2722.
- [14] Yanlai Zhang and Mao Sun. “Dynamic flight stability of a hovering model insect: lateral motion”. In: *Acta Mechanica Sinica* 26.2 (May 2010), pp. 175–190.
- [15] Sanjay P. Sane and Michael H. Dickinson. “The aerodynamic effects of wing rotation and a revised quasi-steady model of flapping flight.” In: *The Journal of experimental biology* 205.Pt 8 (Apr. 2002), pp. 1087–1096.
- [16] Matěj Karásek and André Preumont. “Flapping Flight Stability in Hover: A Comparison of Various Aerodynamic Models”. In: *International Journal of Micro Air Vehicles* 4.3 (Sept. 2012), pp. 203–226.
- [17] Sophie F. Armanini et al. “Quasi-steady aerodynamic model of clap-and-fling flapping MAV and validation using free-flight data”. In: *Bioinspiration & Biomimetics* 11.4 (June 2016), pp. 1–25.
- [18] Matej Karasek et al. “A bio-inspired free-flying robot elucidates how fruit flies control rapid banked turns”. In: (*under review*) (2018).
- [19] Torkel Weis-Fogh. “Quick Estimates of Flight Fitness in Hovering Animals, Including Novel Mechanisms for Lift Production”. In: *J. Exp. Biol.* 59.1 (1973), pp. 169–230.
- [20] M. Sun. “Dynamic flight stability of a hovering bumblebee”. In: *Journal of Experimental Biology* 208.3 (2005), pp. 447–459.
- [21] Floris van Breugel, William Regan, and Hod Lipson. “From insects to machines”. In: *IEEE Robotics & Automation Magazine* 15.4 (Dec. 2008), pp. 68–74.
- [22] L. Ristroph et al. “Active and passive stabilization of body pitch in insect flight”. In: *Journal of The Royal Society Interface* 10.85 (2013), pp. 20130237–20130237.
- [23] A. Roshanbin et al. “COLIBRI: A hovering flapping twin-wing robot”. In: *International Journal of Micro Air Vehicles* March (Mar. 2017), pp. 1–13.
- [24] Robert Stengel. *Flight dynamics*. Princeton, NJ : Princeton University Press, 2004, p. 169.

Part II

Preliminary studies

Chapter 2

Introduction to the preliminary research

This part of the report presents more detail about the results shown in Part I, as well as a literature study. Section 3 gives an account of some successful tail-less FWMAV designs. Section 4 presents a review of literature dealing with modeling of FWMAVs. Several state-of-the-art techniques are identified and described in this section. Section 5 deals specifically with control systems. A literature survey of the state-of-the-art of control system developments in theory and practice is presented, followed by a development of candidate control system concepts that will be deployed on the DelFly Transformer platform in the scope of this project. Lastly, Section 6 documents preliminary aerodynamic model development and validation.

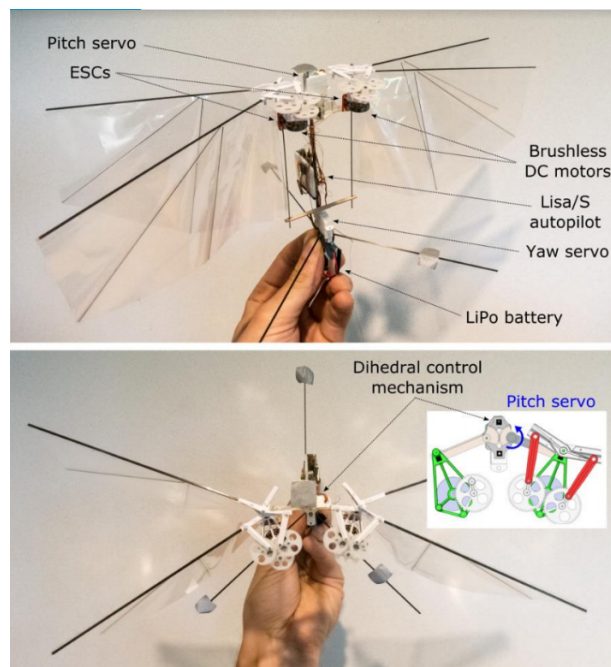


Figure 2-1: DelFly Transformer first prototype

Existing tail-less FWMAVs

This section presents some information about the characteristics of some tail-less FWMAVs that have achieved flight successfully. The KUBeetle in Figure 3-1 was developed at the BIMiLab of Konkuk University in South Korea [8]. It weighs 21 grams and flaps at around 30-35 Hz frequency. Its control system is based on combined rate and attitude feedback. It has demonstrated hovering flight. The Nano Hummingbird in Figure 3-2 was produced by AeroVironment [7]. It weighs less than 10 grams and flaps at 30 Hz frequency. The control system is based on rate feedback only. It has demonstrated hovering, fast forward, and sideways flight. The RoboBee in Figure 3-3 is a product of the Wyss Institute at Harvard University [6]. It is unique in this list of robots due to its piezoelectric wing actuators. It is also relatively small, weighing 80 mg. The nominal flapping frequency is around 110-120 hz. It feature a unique adaptive control system for attitude and position in order to account for uncertainties influencing its flight dynamics. However, its power as well as control system are off-board the robot. The RoboBee has demonstrated hovering flight only.

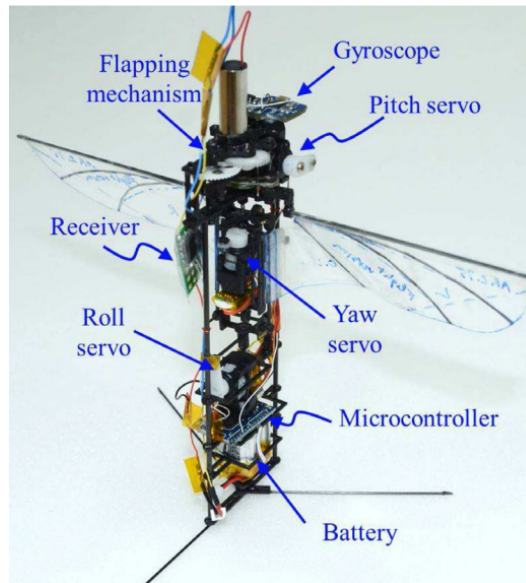


Figure 3-1: KUBeetle [8]

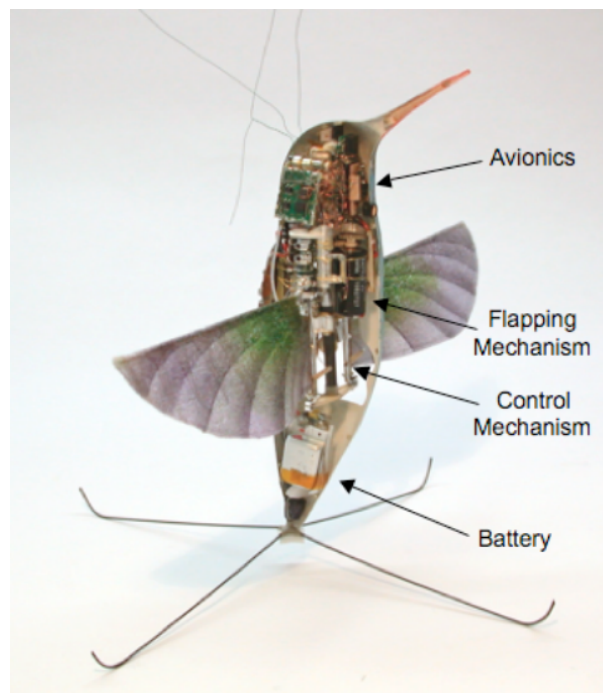


Figure 3-2: Nano Hummingbird [7]

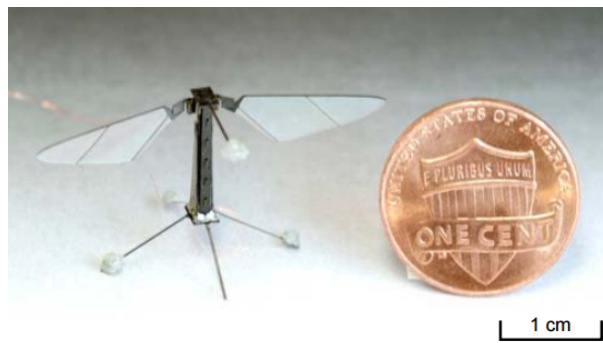


Figure 3-3: RoboBee [6]

Chapter 4

Modeling

The research aim is control-focused, but modeling of a tail-less FWMAV is closely related to control system design. The availability of a reliable model helps to achieve stable flight of a flying platform in the first place, but also to decide how the control system parameters should change to accommodate flight in other flight conditions such as fast forward flight. Depending on the fidelity of the model it could also be used to study the performance of different controller types. Some control system types necessarily require a model and thus a model opens up new possibilities when considering control systems. Therefore, a part of the project is dedicated to reviewing previous work in modeling in an effort to establish the simplest possible dynamic model of a tailless FWMAV. Section 4-1 presents a review of FWMAV modeling methods.

4-1 Previous work in FWMAV modeling

The modeling of the flight dynamics of a FWMAV requires several elements, depending on the complexity of the model. A model can be derived from fundamentals (fluid dynamics and multi-body flexible dynamics) or from high-level approximations (first order polynomials). This section presents the work performed to date in the research field of FWMAV modeling.

Flapping-wing aerodynamic modeling is an area of active research due to its complex nature. Some work utilizes CFD simulations, e.g. [9, 10, 11]. From the perspective of this project, this class of models can be disregarded, because they are too costly to utilize for control system synthesis. A trial-and-error based tuning approach combined with flight tests on a real platform would arguably produce results faster and provide at least as much insight into the behavior of the flapping flyer.

A very popular approach to aerodynamic modeling is the use of quasi-steady blade-element models [12, 13, 14]. The descriptions of aerodynamic forces and moments in these models are composed of several elements, depending on the complexity of the model. The basis

of the model is usually a steady-state component, which can be likened to a fixed wing traveling through air in steady conditions. The other components are supplements to the steady component in order to model various unsteady effects that flapping flight relies on to produce extra lift. These effects include delayed stall, rotational circulation, added mass, wake capture, etc [15]. A specific unsteady mechanism that the DelFly Transformer tailless FWMAV utilizes is the clap-and-fling effect, first discovered by Weis-Fogh [16]. As the DelFly Transformer flies, its wings clap together and fling apart once every flapping cycle. This enables the flapping wings to create additionally a suction effect during fling and also a jet of air during the clap. The net effect is that higher thrust is produced than without this phenomenon.

The quasi-steady/blade-element models sacrifice accuracy for simplicity and required computational resources as compared to computational fluid dynamics model. Despite requiring a less involved mathematical description of the aerodynamics, the model requires a description of the wing kinematics. Identifying the parameters of the models describing these effects requires rather involved system identification activities [14], especially to properly model the clap-and-fling effect.

The forces and moments can be averaged over each flapping-cycle, which results in simpler models that depend on fewer wing movement parameters. Out of all forms of quasi-steady models, the flap-averaged model is most suitable for control work. Average force based models can be expressed also without any description on wing kinematics. The works of [17, 18, 19, 20, 21] utilize (and demonstrate the validity of) velocity-linear force models. The highest level of validation for this model class can be found in the work of [21], where the flight data of a real flight prototype is found to agree well with the linear-force model in a near-hover oscillating condition.

Chapter 5

Control

This chapter develops the control system concepts that will be studied on the DelFly Transformer platform. First, a review of the various control approaches that have been studied so far is presented in Section 5-1. Then, the major control system types are analysed for relevance in Section 5-2. The finishing Section 5-3 presents the control system concepts that will be deployed as well as the reasoning behind them.

A multitude of methods are available to produce the necessary aerodynamic forces and moments for flapping wing maneuvers that involve changing the various wing kinematic parameters during flapping [22]. Rather than these control force/moment generation mechanisms, this review focuses rather on fundamental control theories in the context of flapping wing MAVs. Studies of biological flapping flyers suggest that some natural flyers employ linear control techniques to stabilize flight [23, 24, 25, 26, 27]. Linear control techniques have also been studied relatively extensively in control engineering research for flapping flyers [28, 29, 30, 24, 9, 31, 32]. Nonlinear control methods have also seen employment. [33] and [34] develop control laws based on sliding mode control. [35] employ robust nonlinear control. [36] utilize bounded, nonlinear state feedback with quaternions. [37] present a neural network control in . Central pattern generators have been employed as well as analog neuromorphic devices [38, 39]. Most real tail-less flight prototypes fly linear controllers [8, 5]. The Robobee flies using an adaptive sliding mode controller[6]. This means that a lot of validation work on real flight platforms for theoretical controllers is yet to be done.

5-1 Detailed review of control studies

Table 5-1 shows the comparison of the reviewed FWMAV control system research. Subsections 5-1-1 to 5-1-17 discuss in detail the interesting characteristics of the reviewed control system studies.

Table 5-1: Summary of reviewed control system research.

Authors	Dynamic model	Control	Technique	Inputs	Validation type
Deng, Schenato et al [40, 30]	DTLTI (3DOF)	Linear	LQR/LQG	Flap amplitude, Angle of Attack	Simulation
Doman et al. [41, 28, 42, 43, 29, 44]	NLTV (6DOF)	Linear	Pseudo-inverse al-location	Split-/Quarter-cycle frequency modulation, wing bias	Simulation
Serrani [45, 46, 35]	NLTV (3DOF)	Nonlinear robust	Time scale separation	Flap frequency, Stroke plane	Simulation
Sun and Wang [9], Xiong and Sun [31]	LTI (3DOF)	Linear	Modal decomposition, LQR	Flap amplitude and Angle of Attack, Offset and Difference	Simulation
Riffai et al. [36, 47]	NLTV (6DOF)	Nonlinear	Bounded feedback	Flap amplitude, Angle of Attack	Simulation
Cheng and Deng [24]	LTI (3DOF)	Linear	Linear gains: PD	Flap amplitude/Wing bias, Stroke plane	Simulation
Cheng [48]	NLTV (3DOF)	Nonlinear	Neural adaptive	Flap amplitude/Wing bias, Stroke plane	Simulation
Geder et al. [32]	NLTV (6DOF)	Linear	Linear gains: PID	Flap amplitude/Wing bias, Stroke plane	Simulation

Table 5-2: Summary of reviewed control system research.

Authors	Dynamic model	Control	Technique	Inputs	Validation type
Gallagher, Boddhu, et al. [49, 39], Chung and Dorothy [38]	-	Nonlinear	Evolvable oscillator	Flap amplitude, Angle of Attack	Simulation
Li and Duan [50, 51]	-	Nonlinear	H ∞ / Extended State Observer + Nonlinear PD	Flap amplitude, Angle of Attack	Simulation
Jun-Seong Lee et al. [52]	NLTV (3DOF)	Linear	LQR	Stroke plane, Flapping frequency	Simulation
Maria-Belmonte et al. [53]	NLTV (3DOF)	Nonlinear	Active disturbance rejection	Generic aerodynamic forces	Simulation
Guo et al. [37]	NLTV (6DOF)	Nonlinear	Fuzzy neural network	Angle of attack, stroke timing	Simulation
Du et al. [54]	LTI (6DOF)	Linear	LQR	Flapping frequency, body asymmetry	Simulation
Bluman et al. [34]	NLTV (3DOF)	Nonlinear	Sliding mode control	Flapping amplitude, stroke plane, wing bias	Simulation
Keennon et al. [7]	N/A	N/A	N/A	Wing rotation and twist	Real platform
Chirarattananon, Ma, Wood, et al. [55, 56, 6, 57, 33, 58, 59]	NLTV (6DOF)	Nonlinear	Sliding mode control and Lyapunov adaptation	Flap amplitude, Stroke angle, Split-cycle stroke velocity modulation	Real platform

5-1-1 Deng, Schenato et al.

The stabilization system of Deng, Schenato, et al [40, 30] relies on halteres, ocelli, optical flow estimates, and a magnetic compass. It outputs required torques and forces that would reject disturbances and maintain the selected flight mode. These forces and torques are passed to the wing trajectory controller, which takes as input these torques and forces, and generates a wing trajectory to achieve that. Unfortunately, none of the wing trajectory parameters that the authors wish to control are available on the DelFly transformer. Specifically, the wing trajectory controller relies on changing stroke angle amplitude and offset, timing of rotation, mean angle of attack, and upstroke-to-downstroke wing speed ratio. The parameterisation of wing trajectories is developed on the basis of quasi-steady aerodynamics, modeling delayed stall and rotational lift contributions. Then, there is a another mapping that converts the trajectories into actuator voltages. This sort of control structure does not make sense for the DelFly, since the wing trajectory controller is not applicable. It can be modified to be applicable by using a controllability matrix that could be obtained from flight experiments.

The stabilization is based on output-feedback LQR control law. The authors first theoretically construct a stabilizing state-feedback pole-placement controller, and then perform closed-loop system identification based on the prediction error method (PEM). Then, discrete-time linear quadratic gaussian optimal controller design software was used to devise a controller. An LQG controller can then be applied similarly. However, in comparison to classical PD-control there is no specific expectation of an expansion of the region of attraction, since the authors only demonstrate stability in hover and in simulation.

5-1-2 Doman et al.

The control system developed in [41, 28] relies on independent wing actuation and manipulation of vehicle center of gravity. The controlled parameters are flapping frequency and split-cycle parameter on both wings. The split-cycle parameter quantifies the extent to which wing upstroke is impeded and downstroke is advanced. Splitting the flapping cycle allows to generate a force bias during the flapping cycle, allowing the generation of forces and moments with the modulation of this parameter. The change in body forces and moments is, linearly expressed, a product of a control effectiveness matrix (evaluated at a trim point) and the control parameters (i.e. split-cycle parameter, flapping frequency, and also the displacement of the bob-weight in the present case). In order to calculate the necessary parameters while knowing what the moment perturbations must be, the authors use a pseudoinverse of the control effectiveness matrix. The control effectiveness quantities are derived from a quasi-steady model lacking the effects of a leading-edge vortex, wake-capture, and also clap-and-pling. The calculated control parameters are fed to oscillators of piezoelectric actuators.

Further work in [42] treats split-cycle constant-period frequency modulation, which is not of interest for application on the DelFly. Later work in [60] utilizes the method developed in [42] to control a FWMAV. A further development in [44] explores the quarter-cycle wingbeat

modulation concept, where control actions are changed twice as frequently as in the [42] approach.

In conclusion, Doman and Oppenheimer mainly focus on control moment generation strategies than controllers. There is not much to apply on the DelFly Transformer, since the treated strategies are not applicable.

5-1-3 Serrani et al.

The work in [45, 46] presents the development of a globally stabilizing bounded state feedback altitude control law for a cycle-averaged FWMAV vehicle model, specifically the RoboBee as presented in [56]. The authors argue that since the system behaves as a chain of integrators, it appears natural to resort to the nested saturation approach pioneered by Teel in [61, 62]. In [46] the authors develop globally stabilizing longitudinal position control of a 3-DOF FWMAV. [35] expands work in [46] to a different 3-DOF FWMAV configuration in terms of the controllers and present position and pitch angle control law.

The pitch dynamics is controlled via a nonlinear PD-feedback of the pitch angle in order to achieve robust stability. The gains of this feedback law are parameterised using information about the assumed magnitude of uncertainties and disturbances on the system. The aerodynamic model that the authors use does not take into account outside influence on the angle of attack of the wings, which becomes influential in fast flight. The robustness of such a controller, then, comes under question when considering application on the DelFly Transformer.

5-1-4 Sun, Wang, Xiong, et al.

[9] prove via simulation that a hovering insect can be stabilized in hover via state feedback. Unfortunately their approach is also using the body velocity states, which are not available on the DelFly. [31] expands on previous work with further study of wing kinematics on achieved control moments and forces, but does not provide a new controller structure. This type of control system is not applicable on the DelFly Transformer, since body velocities are not known. A state observer might be able to provide estimates of the body velocities in order to deploy this method, but the computational burden will increase.

5-1-5 Rifaï et al.

The work of [36] focuses on the development of bounded state feedback law, taking into account linear and angular movement, with the Robobee [56] vehicle model as the validation platform. The control law applies quaternions for attitude description. It is a cascaded control law, with attitude control being the inner loop and position control being the outer loop. The attitude control is a nonlinear bounded output feedback law. In contrast to single-gain PD-control of attitude, the gains in this law are replaced by saturation functions in order to bound the calculated control torques. This type of law could actually be applied to the DelFly Transformer, but there is currently no need for specifically taking into account

saturation. Without the saturation functions, the controller would be a PD-based quaternion attitude controller. [47] develops an attitude control law that requires the technological equivalents of a 3-axis rate gyro, a 3-axis accelerometer, and 3-axis magnetometer. It is similar to the work in [36], but the orientation description is now vector based. The sensor measurements are also cycle-averaged. In [63] the approach is tested on a quadrotor. The control law is seen to be very oscillatory. In the case of the quadrotor these signals were filtered out by the DC-motors as they behave like low-pass filters. In the case of the pitch actuator of the DelFly this might turn out to be a problem, depending on the frequency content of the oscillation.

Both types of attitude control could be applied to the DelFly Transformer. The main benefits would be the elimination of the singularity due to the Euler angle implementation. It would not, however, solve the problem of control effectiveness and stability characteristics changing strongly between different flight regimes of the DelFly Transformer. It is also uncertain whether the noisy control signal would deteriorate the control performance.

5-1-6 Cheng and Deng

[24] conclude with their studies that PD feedback control of attitude is sufficient to control a fruit fly in various flight regimes. There is nothing novel to conclude from this work as compared to what is implemented on the DelFly Transformer already.

5-1-7 Geder et al.

[32] Also implement a PID-based controller on a simulation model.

5-1-8 Bayandor et al.

[64] present an adaptive control law. It is designed to learn aerodynamic contribution to the equations of motion as developed in their paper. However, the considered system is merely a set of multi-link wings fixed onto a base. The controller is meant to track the trajectories of similar biological fliers. This type of control is unsuitable for the DelFly in the presented form, since the DelFly does not have the degrees of freedom in the wings that would benefit from this approach. Furthermore a flying platform with this control design has not been shown to be able to fly, either in simulation or in real life.

5-1-9 Gallagher et al., Chung and Dorothy

[49, 39] present the designs of evolvable oscillators that could generate the right control inputs for hovering the Harvard RoboFly. This does not apply to the DelFly, since its wings cannot generate complex trajectories in the same way as the RoboFly, but rather has wings directly geared to a DC-motor. Furthermore, the kinematics and aerodynamics of the RoboFly change rather quickly during flight, since they lifetime of its wings is quite short. For this reason, it is very necessary to adapt the wing motion controller

during flight. This is not relevant for the DelFly, since it has rather durable wings. However, it might be interesting in the future if the survivability of the platform is to be enhanced.

[38] also present a nonlinear oscillator designs for controlling wing kinematics.

5-1-10 Li and Duan

[51] presents the design of an attitude controller based on an Active Disturbance Control scheme. It is a PD-based system, where the gains are learned. This scheme requires the measurements of wing force, which is not available on the DelFly and is therefore inapplicable.

[50] present the design of a nonlinear adaptive H_∞ controller. However, it is meant to control the wing kinematics and therefore does not apply to the DelFly.

5-1-11 Jun-Seong Lee et al.

[65] present an LQR-based pitch attitude controller using the stroke plane angle. Full state feedback is used, therefore an observer would be necessary to obtain body velocities for this approach.

5-1-12 Maria-Belmonte et al.

[53] present a longitudinal trajectory tracking controller based on active disturbance rejection control and generalized proportional integral observers. The idea is that the desired system behavior is mathematically described and the rest of the system dynamics is treated as a disturbance, which the negative feedback will be designed to suppress. However, the approach needs a lot of further development since the inputs to the system were generic aerodynamic forces. Furthermore, it is attitude control that is sought in this project, not trajectory control. It is not clear how well this approach would work with attitude control.

5-1-13 Guo et al.

[37] present a fuzzy neural network based controller designed to regulate wing angle of attack and wing rotation timing. Though this type of controller can work with changes made to the control inputs, the nonlinear mapping for the feedback gains is perhaps unnecessarily complex. Secondly, the training of this mapping will be an issue for application for different flight regimes.

5-1-14 Du et al.

[54] present an LQR-based full state feedback controller utilizing iterative learning tuning to change the gain matrix entries in order to achieve a stabilizing controller. With output feedback, this approach could be used if a sufficiently good simulator of the DelFly becomes available. Since the work shows a convergence of the gain in 30 iterations, doing the training on a real platform would be time-consuming and potentially dangerous.

5-1-15 Bluman et al.

[34] present a sliding-mode control system designed to stabilize the pitch axis of a bumblebee. The presented controller is not directly applicable to the DelFly due to the fact that it uses body velocity components in its sliding variable, which would require some sort of observer. Furthermore, the validation simulation does not include actuator dynamics. It is worth noting that the controller is able to reject a relatively large disturbance in hover, but it is unclear how it would behave with actuator dynamics and in fast forward flight.

5-1-16 Keennon et al.

The AeroVironment Nano Hummingbird is another tailless platform that flies successfully [7]. The authors note that 'closed-loop control' is applied on body rates to stabilize the platform, but they do not provide details. It is likely that it is proportional feedback of rates.

5-1-17 Wood et al.

[56] presents the design of a tethered robotic fly, which handles control off-board. The platform uses piezoelectric actuators to move the wings. The applied flight controller consists of three modules: attitude, lateral position, and altitude controllers. A Lyapunov function is used to derive an attitude control law that is asymptotically stable under simplifying assumptions. The control law is analogous to a PD-controller, where the proportional term is related to error of reference orientation, and the derivative term counters angular velocity - acting as a rotational dampener. The gains are experimentally tuned. In the body attitude controller, an integral term is added to achieve a zero-torque state due to manufacturing imbalances between the wings.

[6] offers an alternative approach to [56], where instead of separately identifying uncertainties of the controlled system, an adaptive controller is proposed. It is again composed of an attitude, a lateral, and an altitude controller. Control actions are still calculated off-board. The design of the attitude-controller is again Lyapunov based, but it is distinct from [56]. A sliding control approach is used to derive a control and adaptation law. The yaw orientation is not controlled. Torques are calculated to oppose angular velocity as well as the attitude error, meaning the controller is similar to proportional and derivative feedback. The law also accounts uncertainties in the estimates of moments of inertia as well as torque offsets due to manufacturing variability. What is also remarkable is that no particular representation of rotation is used, which avoids singularities. The approach is proven with flight tests in hover and landing.

[66] offers a strategy to experimentally tune PID-controllers for feedback stabilization of altitude, pitch, and roll.

[57] builds on [6]. The controllers are the same as in [6], but the contribution of the document is a deeper analysis of additional flight tests.

[33] Develops a new single-loop adaptive controller that abandons the principle of time separation previously present in [6, 57], where a cascaded controller was designed. The altitude and attitude controllers are integrated as one loop.

[58] presents a control strategy that was developed with the goal of achieving aggressive maneuvers. Since in previous efforts actuators and aerodynamics were not modeled, the trajectory-following commands are generated with the help of an iterative learning controller to achieve the desired perching maneuvers. While the iterative learner is a key component of the presented controller in performing desired maneuvers without an accurate aerodynamic model, it is not an interesting component for the project at hand, because the focus is not on specific maneuvers, but rather on the whole flight envelope. The also discuss a solution to add yaw control to the sliding surface, which in previous designs was not deemed important for trajectory following.

[59] states that the controller in [58] is already equipped to handle gust force disturbances as well, due to considering acceleration error. However, for torque countering, adaptive and least-square estimation are considered. The combination of the two proposed schemes showed the capability to reject disturbances successfully, with varying applied wind profiles applied to the platform. Though this capability is interesting for future developments, the aim of this thesis is to develop a stabilization system allowing aggressive maneuvers first and foremost.

5-2 General aircraft stabilizing control approaches

This section briefly discusses stabilizing control approaches in the aerospace context in general, in order to contextualize the work that was presented in Section 5-1.

Gain scheduling control

Gain scheduling in combination with linear or nonlinear control methods are a staple of modern aircraft control [67]. Due to its simplicity it is likely that it will also be suitable for use on the DelFly Transformer. The deciding factor will be whether the measured/estimated variables available to the DelFly are suitable as gain-scheduling variables.

Adaptive (non)linear control

Adaptive control has been used for flight control purposes for over half a century now [68]. There are many forms of adaptive control, with different levels of complexity. Broadly speaking, they can be divided into direct and indirect adaptive control approaches, where direct approaches adapt controller parameters and indirect approaches adapt a model online. However, the adaptability of an adaptive control approach does not guarantee stability. For this reason, robust adaptive laws have emerged as a field of research. Emerging robust solutions are able to bound the adapted parameters and also the output, theoretically. The benefit of indirect adaptation is that it can reveal uncertainties of a system. For instance, an experiment with a controller that adapts the control effectiveness of the actuators can reveal the control effectiveness behavior in different regimes of flight. A direct adaptation mechanism could reveal the necessary controller gains so that the adaptation can be removed

or if simple gain scheduling cannot be used, it can still yield a stabilizing controller with a large area of attraction.

5-3 Proposed control system candidates for implementation on the DelFly

This section develops the conceptual candidate control systems that are likely to solve the limited flight envelope issues with the DelFly.

Firstly, a solution is needed for the issue of a singularity with the Euler angle implementation. While the singularity can be shifted to different orientations depending on the order of rotations of the angles, there is no convenient location where this can be shifted without becoming a problem later. Rather, a solution can be sought from other descriptions of orientation. Quaternions are a handy solution to this issue and was already used in other work by Rifaï et al. in [36]. Direction Cosine Matrix (DCM) based descriptions are also suitable, since there is a lack of a singularity. However, in this case, there are a total of 9 differential equations to solve in order to update all entries of the DCM compared to the 4 of the quaternion-based orientation description. Therefore any control systems for a very maneuverable FWMAV should use one of these or potentially even more complex (Modified Rodriguez Parameters, etc.) attitude descriptions to retain the ability of stable flight in any orientation.

Due to the changing of the aerodynamic control effectiveness and stability characteristics of the DelFly in different flight regimes, constant-gain control laws may not provide stability in flight regimes far removed from hover. For instance, in fast descents, roll instability has been observed on the DelFly. Furthermore, once the Euler singularity is solved, higher forward flight speeds will become available. The gain values that have been used thus far will not be optimal. Furthermore, the current gain settings might even cause instability in the fast forward flight regime. The same issue might be present in fast sideways flight.

From the practical control system viewpoint, the optimal solution will be minimal in terms of needed computational power and memory use. It should also be easy, safe and quick to tune. From this perspective, one of the candidates that should be pushed to its limits is definitely still a single-gain linear controller. The slightly more complex solution of a linear controller with gain scheduling is also a highly interesting solution. If this still is not possible or is working poorly, then an adaptive approach could be able to provide a larger operational envelope. Furthermore, the adaptation can reveal characteristics of the platform in flight that are difficult to measure such as its moment of inertia or any control asymmetries due to manufacturing variability. Some adapted parameters do not change appreciably after convergence and can then be fixed (it is likely that the moment of inertia is one such parameter).

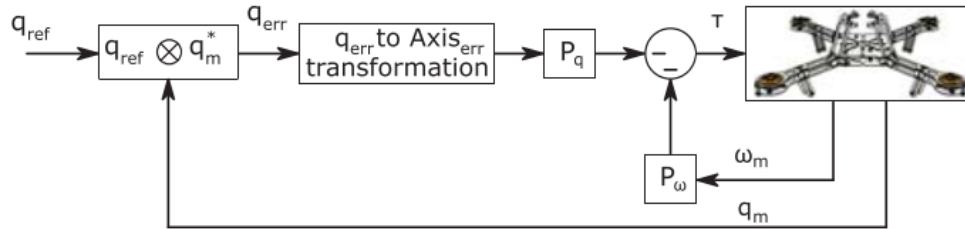


Figure 5-1: Quaternion attitude/rate controller layout as presented in [69]

5-3-1 Single-gain quaternion-based attitude feedback

The PD-control of attitude will have to be changed to a quaternion-based representation, such as the one presented in [69], also shown in Figure 5-1. In the case shown in Figure 5-1 the rate reference is zero, but in the case of the DelFly Transformer the reference generator gives a rate reference too. Then, once a wider flight envelope becomes available without attitude singularities, the DelFly platform will have to be pushed in flight tests to those areas of the flight envelope that were previously unavailable in order to be able to characterize the performance of the control system. The preliminary model can be used to try to improve the set gains in order to attempt to improve the controller.

5-3-2 Gain-scheduled quaternion-based attitude feedback

The most primitive controller as presented in Section 5-3-1 and shown in Figure 5-1 will be changed to have a variable gain. It is not obvious which variables or what type of scheduling would be most effective, but a good start would be to use the flapping frequency and the pitch angle. Since the actual horizontal flight speed depends on how long the aircraft has been inclining off the vertical, some sort of gain-changing low pass filter or delay might be necessary. Flight tests will reveal how this configuration compares to the single-gain controller.

5-3-3 Adaptive feedback control

There are many forms of adaptive control. The attitude control system as presented in [57] is interesting from the perspective that it has a large area of attraction, but it does not model actuators or aerodynamics. Aerodynamics and actuator dynamics will play a significant role in the trimmed flight of the DelFly at fast velocities, which is why this approach is not likely to work directly without modifications. The first major difficulty is that though one could model the aerodynamics and use this knowledge in control law design, the relevant velocity states are not measured. The second major difficulty is that the aerodynamic force due to oncoming air significantly influences the effectiveness of the wing dihedral actuator. At high forward flight speeds, the current controller is having to command more extreme servo positions to force the wings to take the required position. In order to avoid having to model the whole system, the incremental nonlinear dynamic inversion (INDI) approach of [70] is chosen as the adaptive controller to be deployed. See the corresponding controller layout as in Figure 5-2.

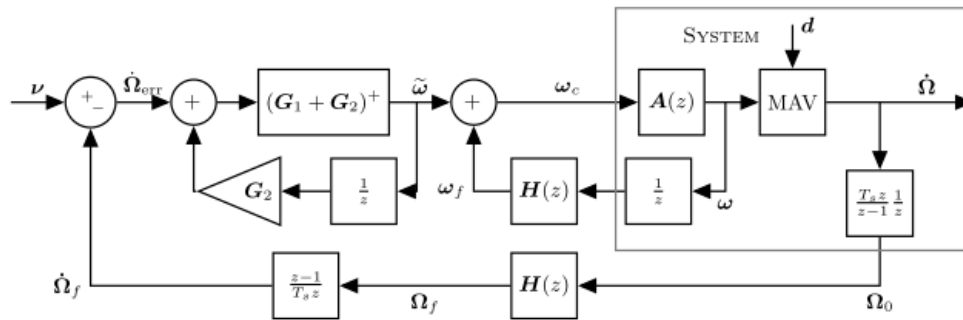


Figure 5-2: INDI controller layout as presented in [70]. $A(z)$ denotes actuator dynamics, $H(z)$ is a second order measurement filter.

The major challenges of INDI are its dependence on a noisy angular acceleration reading and delays due to having to filter signals. Smeur et al. managed to demonstrate solutions on a quadrotor, but the approach has not been characterized on a FWMAV platform. A further boon of deploying this particular technique is that the Aerospace Engineering faculty of Delft University of Technology has experts in this technique that can be of help with solving issues that may arise.

Model development for DelFly Transformer tailless FWMAV

This section presents the development of the aero- and flight dynamics models of the DelFly Transformer. The preliminary work focuses on the development and validation of longitudinal dynamics. If the longitudinal model can be validated and its performance characterized, then an expansion into a full 6-degree-of-freedom model is not a conceptual leap.

Section 6-1 describes the measurement of thrust force as well as the identification of flapping frequency actuator dynamics. Section 6-2 presents the identification of the pitch control actuator dynamics. Section 6-3 documents the process of extracting aerodynamic model parameters from flight data. Section 6-4 gives the full nonlinear system equation of motion. Section 6-5 presents the process and results of validating the aerodynamic model on the basis of flight data.

6-1 Thrust force and thrust actuator dynamics

In order to measure the thrust force produced by a single flapping mechanism (the wings on one side of the body only), the mechanism was mounted on the force/torque sensor. Recordings of the electronic speed controller motor polarity change intervals were also available for calculating motor speed. The range of minimum to maximum PWM commands was divided into multiple setpoints and the generated thrust force was measured for 2 seconds at a measurement rate of 10 kHz. The force measurements were filtered with a Butterworth low-pass filter with a cut-off frequency equal to the flapping frequency estimated using the mean motor speed and the gear ratio of the mechanism. Fluctuations of the motor speed were used to identify individual flap cycles and their period/frequency. The force measurements were then cycle-averaged.

Figure 6-1 shows the relationship between the thrust and the flapping frequency. The markers of the plot are centered on the mean force and flapping frequency of each measurement. Error

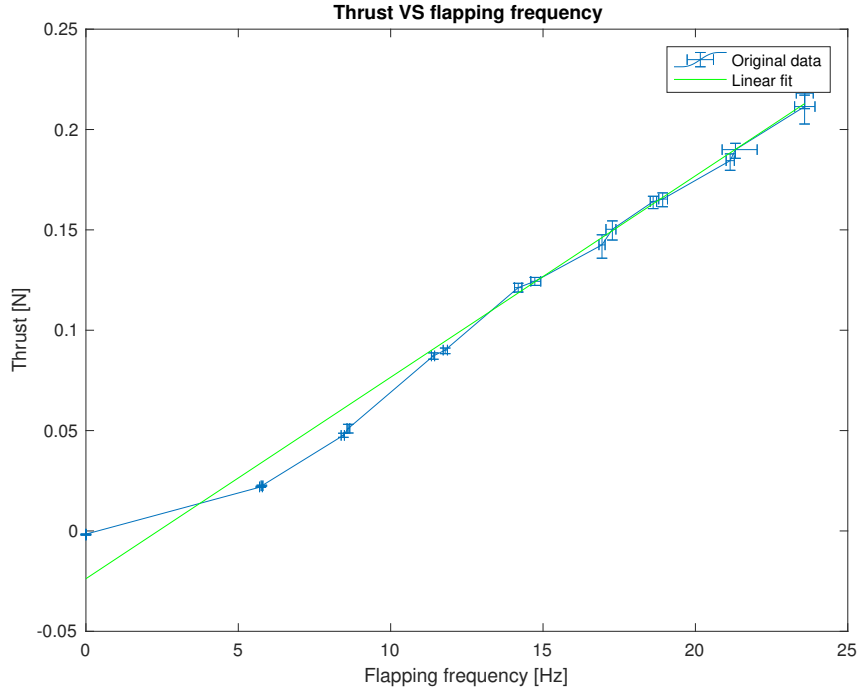


Figure 6-1: Thrust versus flapping frequency.

bars represent their standard deviation. Additionally, a linear function is fitted to data above 13 Hz, a region representative of the nominal operating point of the DelFly Transformer. This linear fit will be used in further work to relate flapping frequency to a thrust force. The expression for this function is $T = c_1 f + c_2$, where T is thrust in newtons, f is flapping frequency in Hz . The values of the constants are $c_1 = 0.0100358$ and $c_2 = -0.0237866$. Note that this expression calculates the thrust for one wing pair only.

Figure 6-2 presents the relationship between mean cycle-averaged flapping frequency and the mean PWM signal sent to the electronic speed controller driving the motor. The separate measurement series are distinguished as the red and blue lines. There are less data points for the series represented by the red line, because the wing root became dislodged from the flapping mechanism due to missing glue for fixation. After gluing the root to the mechanism, a new series of measurements was recorded, represented by the blue line. This seems to have influenced the generated flapping frequency to an extent. Especially around the nominal hovering frequency of 16.5 Hz the trend does not behave linearly. Furthermore, the generated frequency will be slightly different in flight. For truly representative data, it should be collected from flight tests.

In the following, the identification of the flapping frequency actuator dynamics is described. The MATLAB System Identification toolkit was used to estimate a suitable transfer function for the flapping frequency. The output data was the unfiltered flapping frequency and the

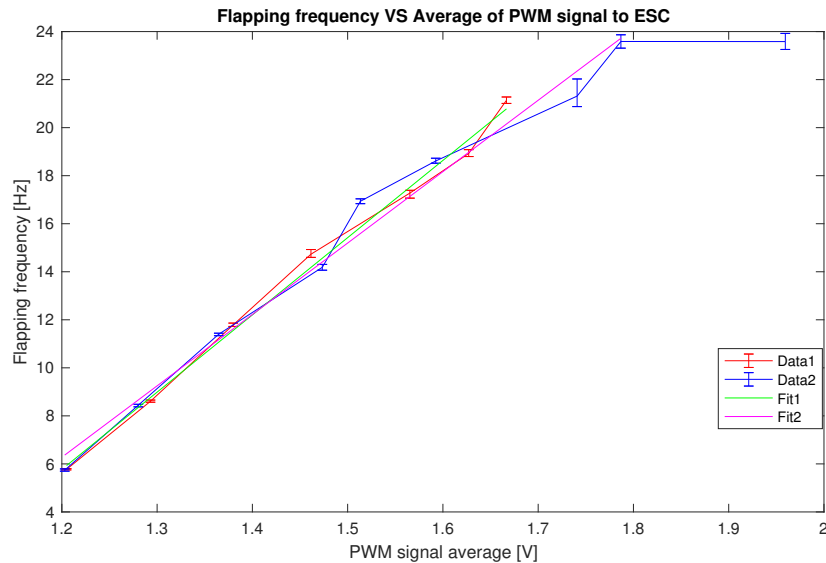


Figure 6-2: Flapping frequency versus average PWM signal

input data was an approximately scaled PWM signal. This means that the 4 Hz Butterworth filtered measurement of flapping frequency was used to roughly estimate the steady state of the flapping frequency command, as shown in Figure 6-3.

The resulting best estimate transfer function is $T(s) = \frac{12.41}{s+12.39}$, simulated in Figure 6-4. Higher order transfer functions did not improve the result. In order to remove the meaningless steady state error, the transfer function that is used in further work is $T(s) = \frac{12.39}{s+12.39}$. This transfer function represents the non-dimensional dynamics of the flapping frequency.

6-2 Pitch moment actuator dynamics

This section presents the identification procedure for the pitch control actuator dynamics. Pitch moment measurements were the basis for calculating a leverage arm based on the principle that a torque is equal to a force multiplied by its leverage arm. Therefore a leverage arm can be calculated from dividing a torque with a force. The output data used for identification is the unfiltered moment divided by the mean measured force, with an approximately scaled moment command as input. On the real platform, the actuator does not change this arm proportionally, but rather via a sinusoidal relationship. The assumption was made here that this would not have a significant impact on the validity of the model. Figure 6-5 shows a comparison of two different estimated transfer functions with a 5 Hz Butterworth-filtered version of the calculated leverage arm for easier comparison. The green line represents a 1st order transfer function and the gray line represents a 2nd order transfer function. The 2nd order transfer function fits the trend of the calculated and filtered pitch leverage arm.

The resulting transfer function is $T(s) = \frac{525.7}{s^2+30.55s+558.8}$. The steady-state error is removed by changing the transfer function to $T(s) = \frac{558.8}{s^2+30.55s+558.8}$.

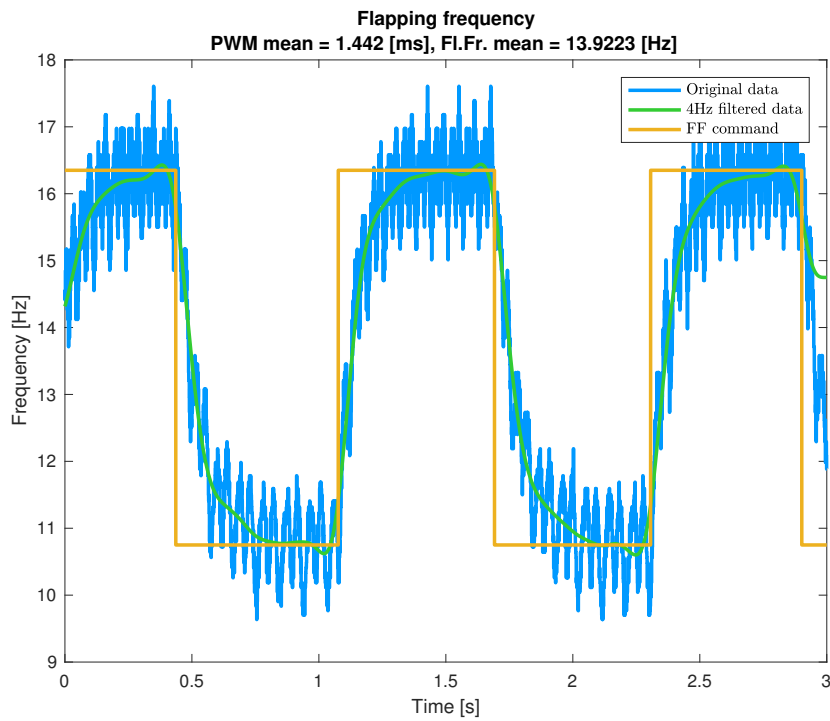


Figure 6-3: Approximately scaled flapping command function versus the original and filtered measurement.

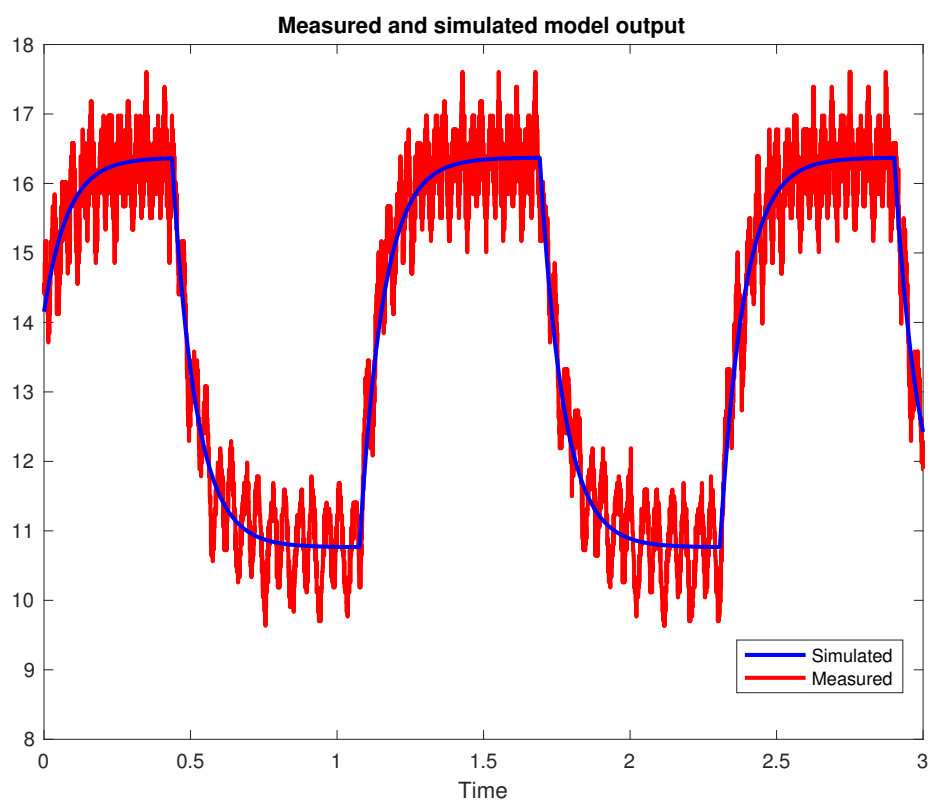


Figure 6-4: Measured (black) and simulated (blue) flapping frequency.

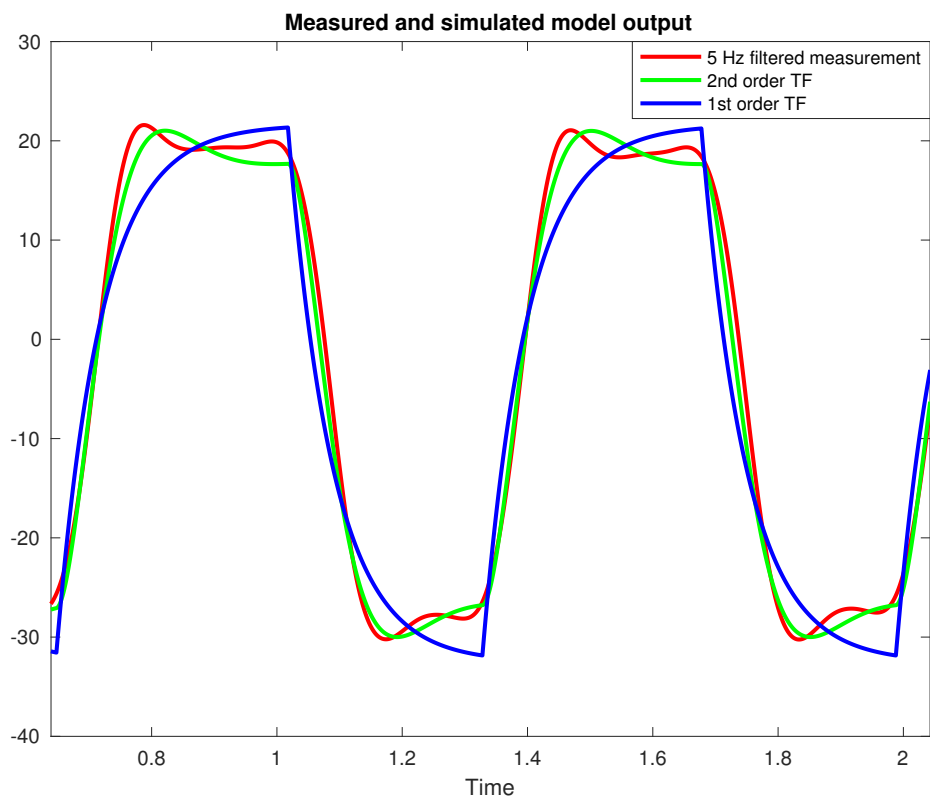


Figure 6-5: Filtered, calculated pitch leverage arm (red) and simulated pitch leverage arms (blue - 1 pole, green - 2 poles).

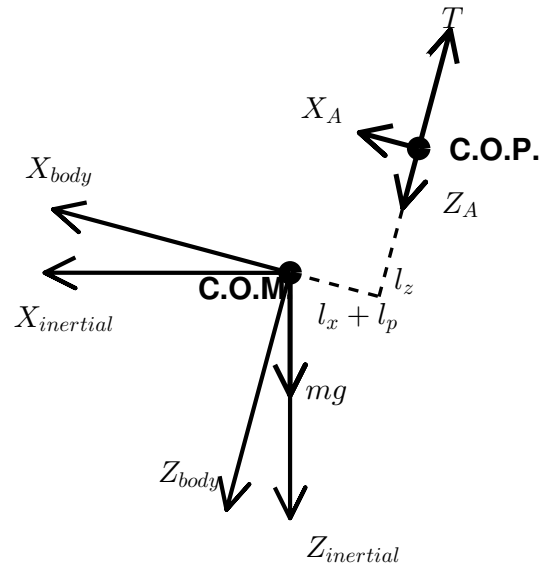


Figure 6-6: Free body diagram for Equations 6-1. C.O.M. - center of mass, C.O.P. - center of pressure.

6-3 Experimental study of aerodynamic forces

This section presents the development of the structure of the aerodynamic model. Data was available from flight tests conducted previous to this project. The DelFly Transformer was flown against the wind in the Open Jet Facility of TU Delft Aerospace Engineering. The goal of these tests was to achieve trimmed flight at known airspeeds. Onboard state estimation data was recorded as well as the windspeed. Six different trim points are identifiable in the data at windspeeds of 1, 1.25, 1.75, 2, 2.4, and 2.7[m/s]. A limitation of the data is that there are no data points below 1[m/s] due to the inaccuracy of the windtunnel airspeed control. Furthermore, trimmed flight of any duration was very difficult to achieve for the pilot. However, these data points can be obtained from tests in the CyberZoo.

The mean flapping frequency and pitch angle of each trim data window was calculated. Following that, and assuming a force and moment balance per each trim condition, Equations 6-1 can be used to solve for aerodynamic forces L, D in the aerodynamic reference frame and X, Z in the body reference frame. The free body diagram accompanying the equations is shown in Figure 6-6. The thrust is known via the relationship to the flapping frequency identified in Section 6-1. The pitch attitude has been recorded using the onboard IMU of the DelFly Transformer. The mass of the platform is also known.

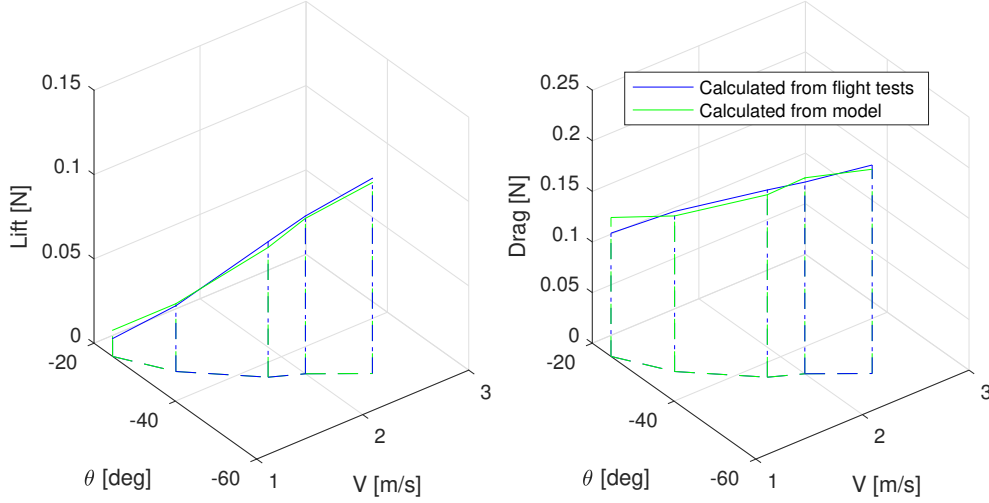


Figure 6-7: Lift and drag versus airspeed and pitch angle (measurements - blue, model - green).

$$\begin{aligned}
 + \leftarrow \sum F_{x,inertial} &= T \sin(\theta) - D = 0 \\
 + \downarrow \sum F_{z,inertial} &= -T \cos(\theta) + mg - L = 0 \\
 + \swarrow \sum F_{x,body} &= mg \sin(-\theta) + X = 0 \\
 + \searrow \sum F_{z,body} &= mg \cos(-\theta) - T + Z = 0
 \end{aligned} \tag{6-1}$$

Assuming that both body forces X and Z are proportional to the product of the respective body velocities u and w some constants b_x and b_z , one can use the least squares technique to find these constants. This assumption at least holds for the body axis x according to the work of [19]. Dividing by two to account for the fact that these constants should apply for one wing pair, $b_x = -0.07219$ and $b_z = -0.01567$. The resulting fit with the data points is shown in Figures 6-7 and 6-8. Since there is a difference between the thrust produced by the wings in this flight data and the thrust relationship established on the force balance, an extra constant offset is required for force equilibrium: $Z = b_z w + b_{z,0}$. In this case it is $b_{z,0} = 0.02994$, which means that the wings in the flight test are producing on average $0.03N$ more thrust than the identified relationship on the force balance. This term is not included in the full nonlinear flight dynamic model since it is liable to change and likely does not influence angular dynamics significantly.

6-4 Full nonlinear longitudinal model

Rigid body dynamic equations are used to model the flight dynamics, as for conventional fixed-wing aircraft [71]. As determined in Section 6-3, the aerodynamic forces along X and

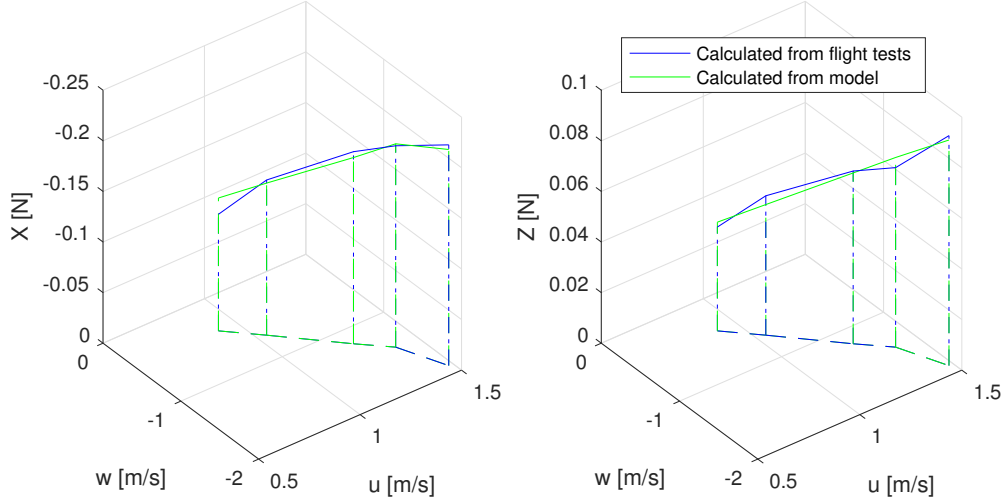


Figure 6-8: Aerodynamic body frame forces versus body velocities (measurements - blue, model - green).

Z body axes can be modeled with a linear relationship of the corresponding velocities.

In order to assemble the equations of motion, the force and moment balance needs to be established. The free body diagram of a 3-degree-of-freedom FWMAV is presented in Figure 6-9. Here, thrust is denoted as $T = c_1 f + c_2$, where c_1 and c_2 are the constants of a linear function as determined in Section 6-1. X_A and Z_A stand for aerodynamic forces along the X - and Z -axes of the body, respectively. l_x is the constant distance from the average center of mass to the average center of pressure of the wings along the X -axis of the body. l_p represents displacement in the same direction as l_x , and this is the distance that pitch control actuator varies. l_z is the constant distance from the average center of mass to the average center of pressure of the wings along the Z -axis of the body.

$$\begin{aligned}
 + \swarrow \sum F_{x,body} &= m\dot{u} \\
 + \searrow \sum F_{z,body} &= m\dot{w} \\
 + \circlearrowleft \sum M_{y,body} &= I_{yy}\ddot{\theta}
 \end{aligned} \tag{6-2}$$

Summing forces and moments and using Equations 6-2, the nonlinear state derivatives can be extracted. These are given in Equations 6-3.

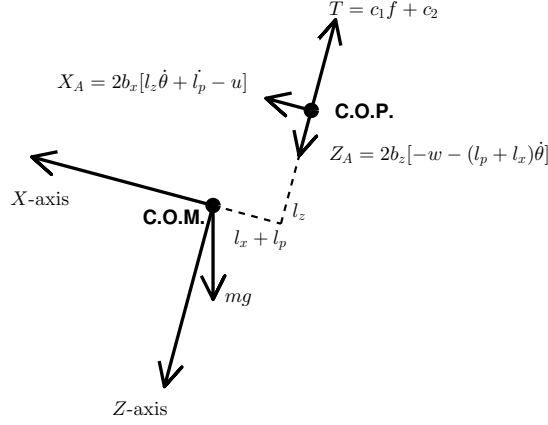


Figure 6-9: Free body diagram of the FWMAV, longitudinal forces only. C.O.M. - center of mass, C.O.P. - center of pressure.

$$\begin{aligned}
 \dot{u} &= -\sin(\theta)g - \frac{2b_x u}{m} + \frac{2l_z b_x \dot{\theta}}{m} + \frac{2b_x \dot{l}_p}{m} \\
 \dot{w} &= \cos(\theta)g - \frac{2c_1 f}{m} - \frac{2c_2}{m} - \frac{2b_z w}{m} - \frac{2b_z(l_p + l_x)\dot{\theta}}{m} \\
 \ddot{\theta} &= [2b_x l_z u - 2b_x l_z^2 \dot{\theta} - 2b_x l_z \dot{l}_p - 2c_1 f(l_p + l_x) \\
 &\quad - 2c_2(l_p + l_x) - 2b_z w(l_p + l_x) - 2b_z(l_p + l_x)^2 \dot{\theta}] / I_{yy}
 \end{aligned} \tag{6-3}$$

The transfer function for flapping frequency was identified to be $T(s) = \frac{12.35}{s+12.35}$ in Section 6-1. In the time domain, this represents $\dot{f} + 12.35f = 12.35f_c$, where f_c is the commanded flapping frequency. This flapping frequency command can be related to the PWM commands via the relationships in Figure 6-2, though these do not incorporate the effect of oncoming airspeed on the achieved flapping frequency. The transfer function for l_p or the portion of the pitch moment leverage arm that can be varied by the actuator was identified to be $T(s) = \frac{558.8}{s^2+30.55s+558.8}$. In the time domain this represents $\ddot{l}_p + 30.55\dot{l}_p + 558.8l_p = 558.8l_{p,c}$, where $l_{p,c}$ is the commanded value. The pitch moment leverage arm can be calculated via $l_{p,c} = l_y \sin(\Gamma)$, where l_y is the nominal distance of the center of pressure of a wing pair from the center of mass along the body y -axis and Γ is the dihedral angle.

6-5 Model validation

This section presents the conducted model validation efforts. A previously collected dataset from flight tests conducted in the CyberZoo of the TU Delft Aerospace Engineering department was used to compare model output to actual flight. The OptiTrack system was used to

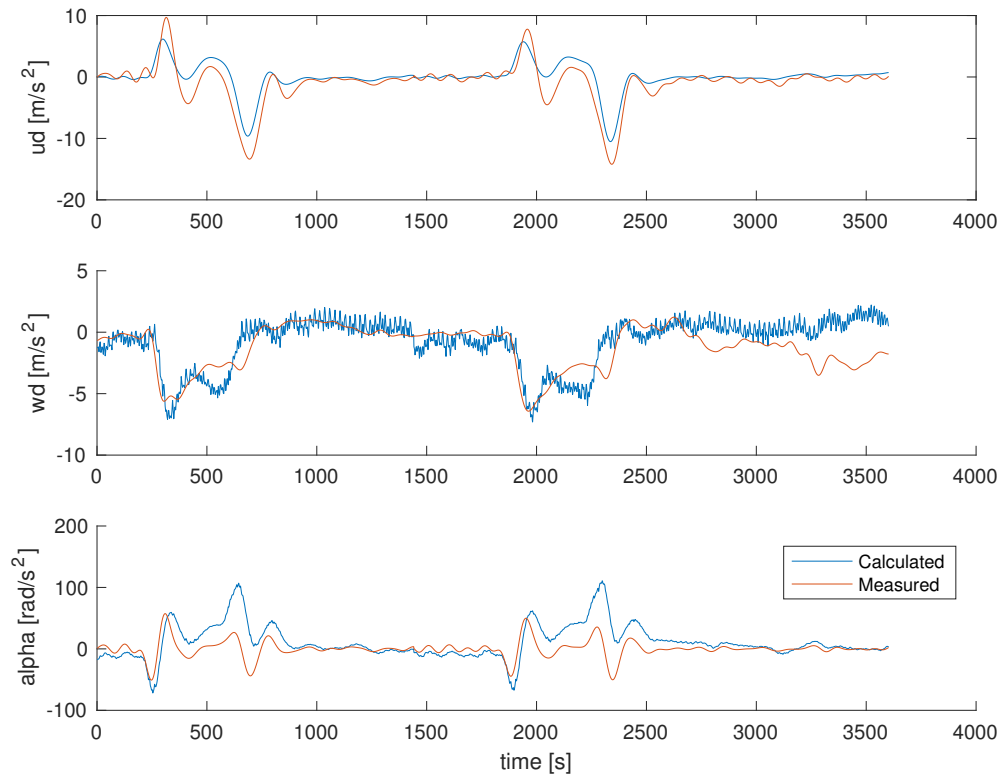


Figure 6-10: Model fit with previously identified values. X-axis is data point index

measure the position and attitude of the DelFly Transformer in time. OptiTrack is a motion capture system based on a grid arrangement of cameras. Differentiation leads to estimates of translational and rotational velocities and accelerations. All states were low pass filtered at 50 Hz with a Butterworth filter. In order to compare model output and the OptiTrack-derived accelerations, linear and angular accelerations from the model were calculated with Equations 6-3 using the OptiTrack-derived states. The comparison between the OptiTrack-derived and model output accelerations is given in Figure 6-10.

It was found that the actuator command was not appropriate to use for calculating the real position of the pitch actuator, because the actual dihedral angle differs strongly from the command. This could be due to some compliance or play in the mechanical design. Another reason could be that the aerodynamic force generated from oncoming air as the DelFly pitches forward is strong enough to be quite a difficulty for the pitch servo, which has to give stronger commands to achieve stability. A new attempt at validation was made after using measurements of the actual position of the wing hinges. Furthermore, the second pitch maneuver in 6-10 was disqualified from the comparison since the hinge location fix was lost by OptiTrack for this maneuver. The first pitch maneuver is the same. Figure 6-11 shows that the model is now in better agreement in terms of the angular accelerations. The noisy output of the calculation is the result of using an optitrack-derived hinge angle, which was noisier than the states, but was still filtered with 50 Hz Butterworth low pass filter. The

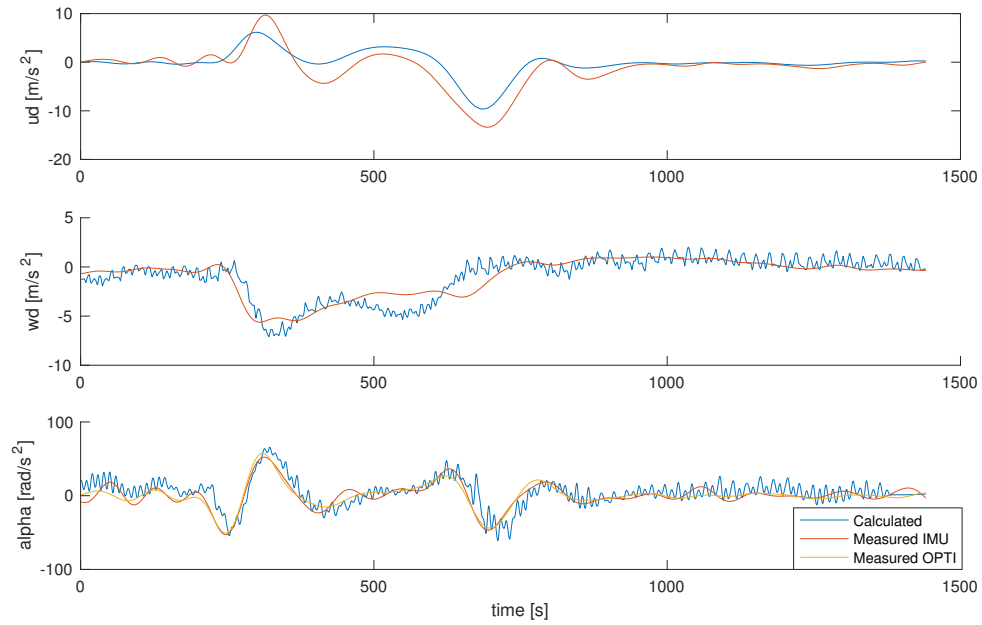


Figure 6-11: Model fit with previously identified values and actual hinge position. X-axis is data point index

linear acceleration state derivative \dot{u} shows the correct trend, but \dot{w} shows a discrepancy. It is not clear where this comes from.

Appendix A

Individual flight maneuvers - dataset I

A-1 Maneuvers with 15 degree pitch setpoints

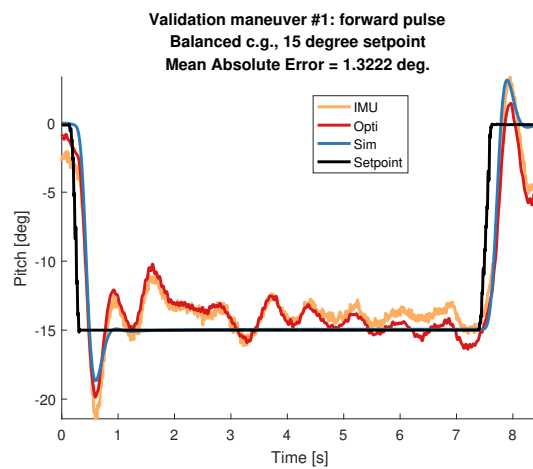


Figure A-1: First validation step maneuver with 15 degree pitch forwardsetpoint.

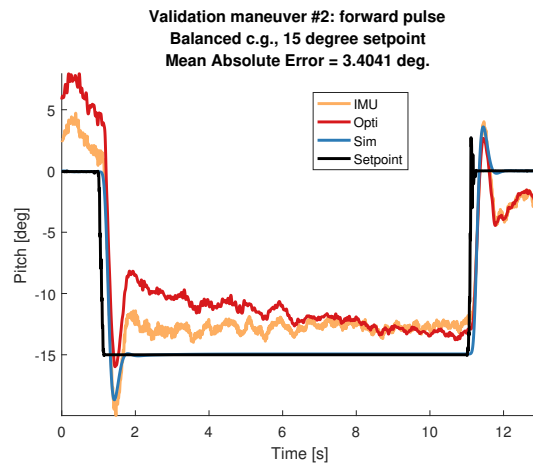


Figure A-2: Second validation step maneuver with 15 degree pitch forward setpoint.

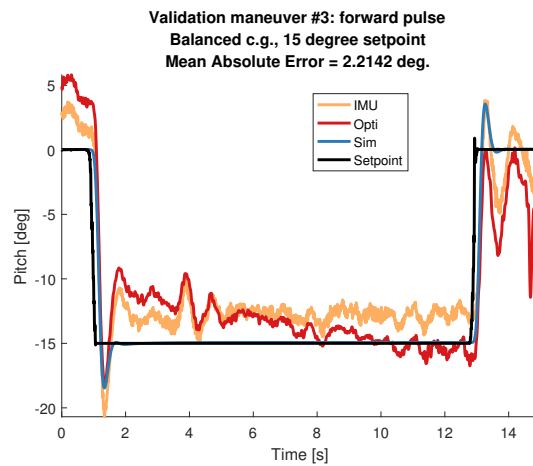


Figure A-3: Third validation step maneuver with 15 degree pitch forward setpoint.

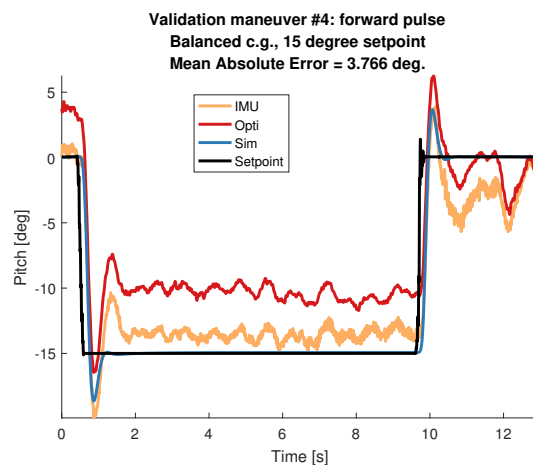


Figure A-4: Fourth validation step maneuver with 15 degree pitch forward setpoint.

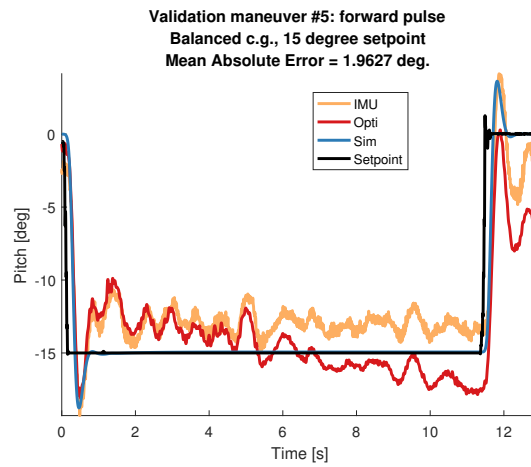


Figure A-5: Fifth validation step maneuver with 15 degree pitch forward setpoint.

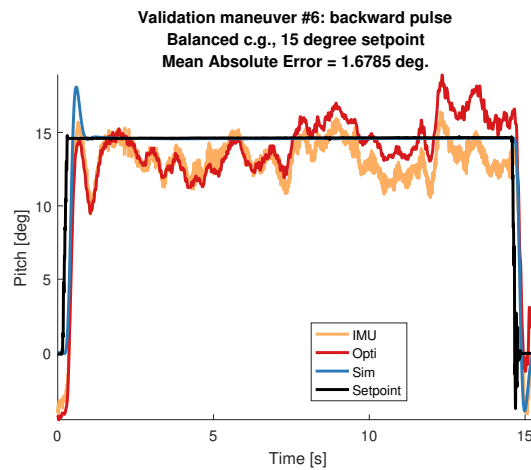


Figure A-6: First validation step maneuver with 15 degree pitch backward setpoint.

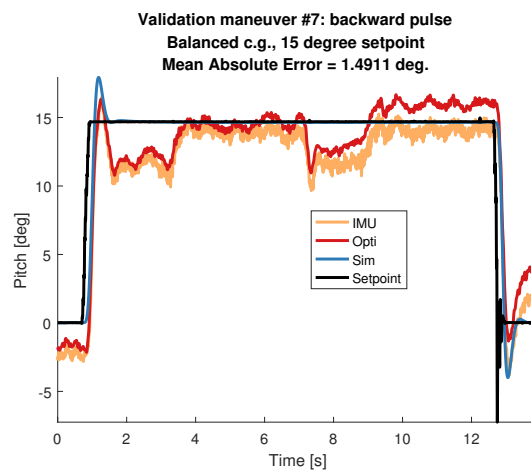


Figure A-7: Second validation step maneuver with 15 degree pitch backward setpoint.

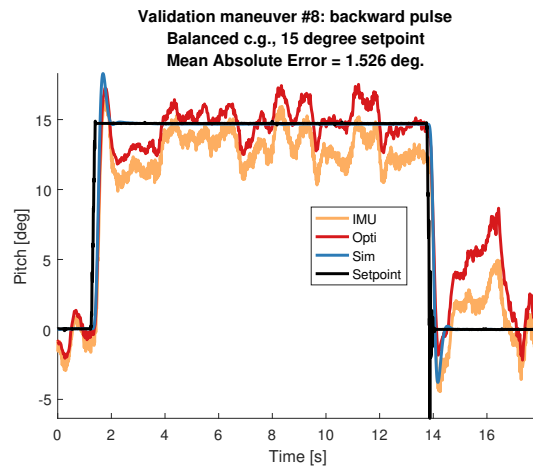


Figure A-8: Third validation step maneuver with 15 degree pitch backward setpoint.

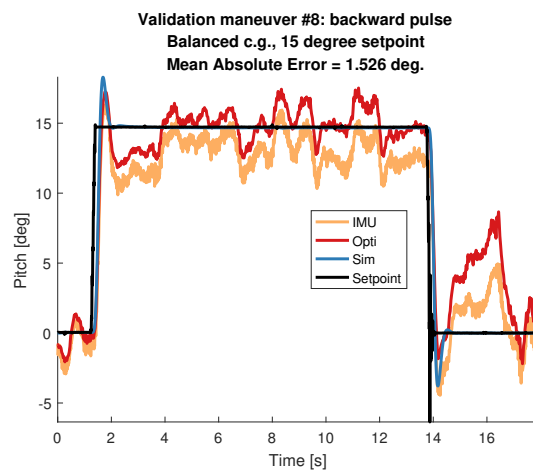


Figure A-9: Fourth validation step maneuver with 15 degree pitch backward setpoint.

A-2 Maneuvers with 30 degree pitch setpoints

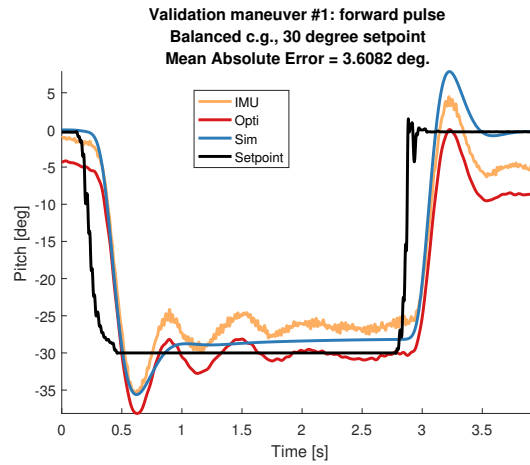


Figure A-10: First validation step maneuver with 30 degree pitch forward setpoint.

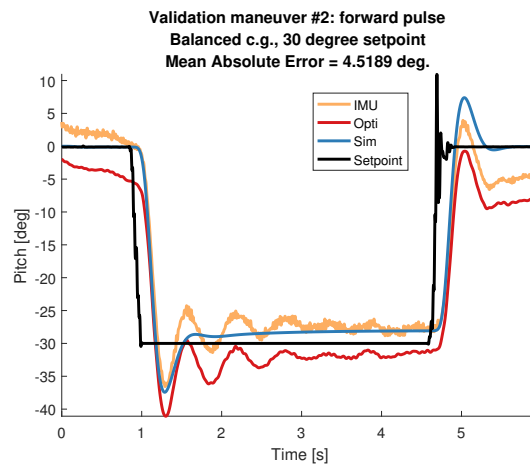


Figure A-11: Second validation step maneuver with 30 degree pitch forward setpoint.

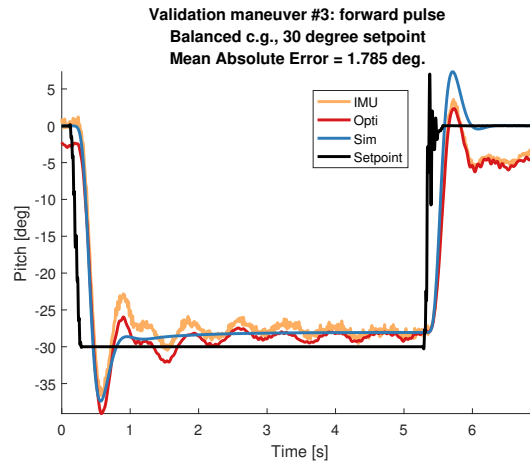


Figure A-12: Third validation step maneuver with 30 degree pitch forward setpoint.

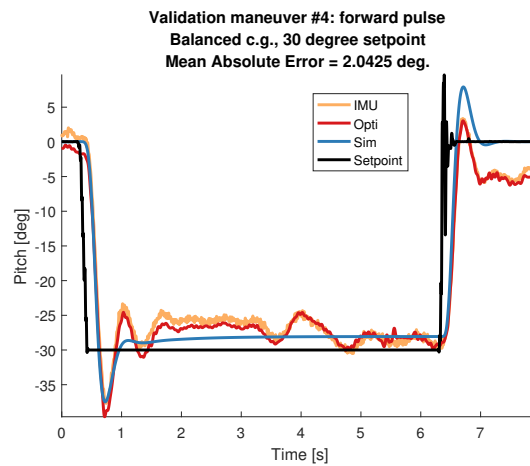


Figure A-13: Fourth validation step maneuver with 30 degree pitch forward setpoint.

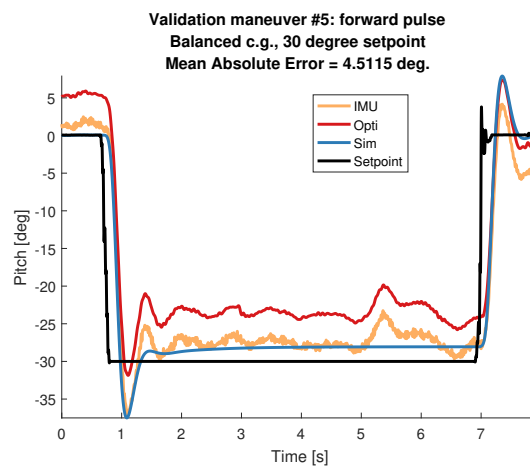


Figure A-14: Fifth validation step maneuver with 30 degree pitch forward setpoint.

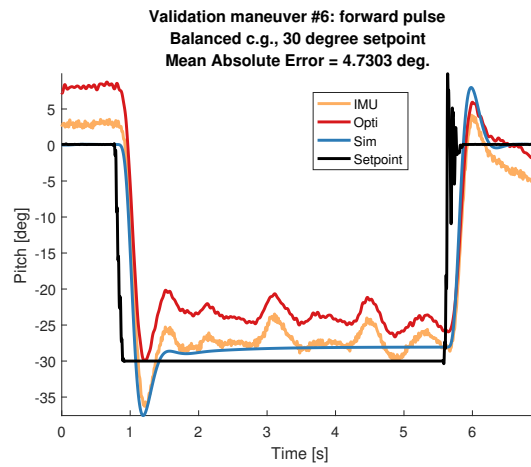


Figure A-15: Sixth validation step maneuver with 30 degree pitch forward setpoint.

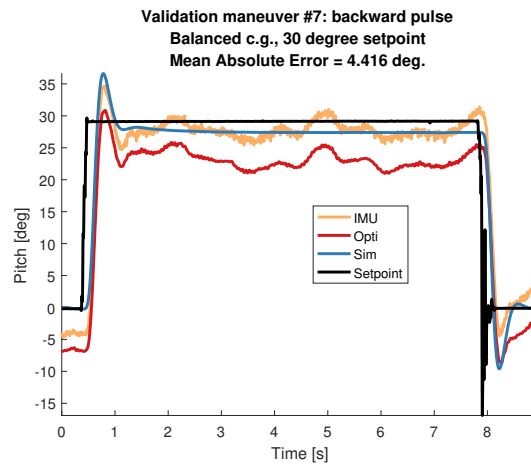


Figure A-16: First validation step maneuver with 30 degree pitch backward setpoint.

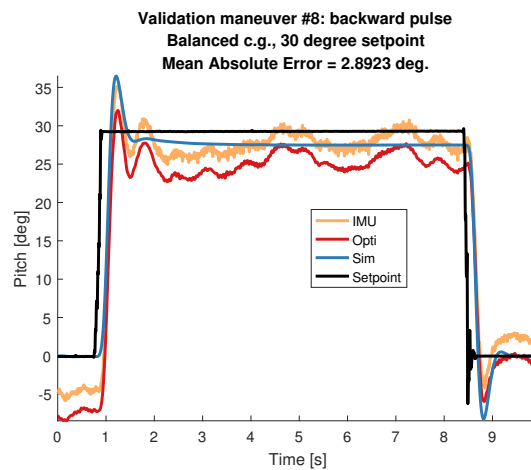


Figure A-17: Second validation step maneuver with 30 degree pitch backward setpoint.

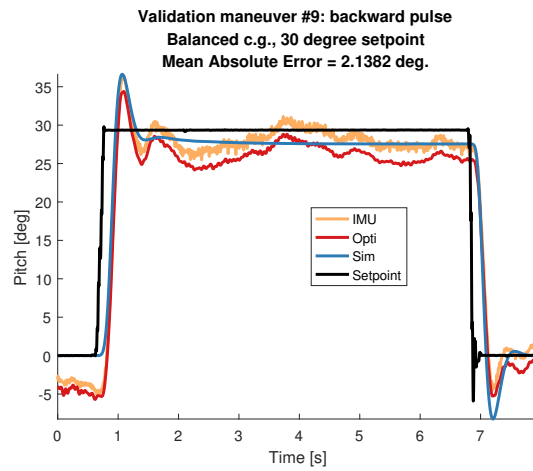


Figure A-18: Third validation step maneuver with 30 degree pitch backward setpoint.

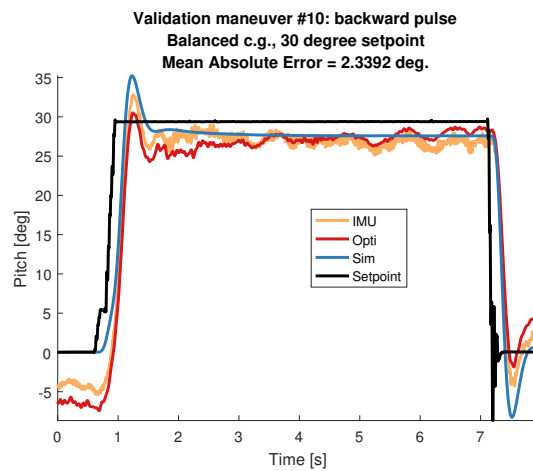


Figure A-19: Fourth validation step maneuver with 30 degree pitch backward setpoint.

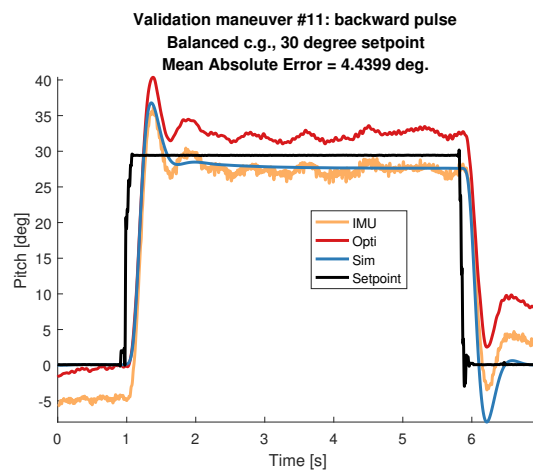


Figure A-20: Fifth validation step maneuver with 30 degree pitch backward setpoint.

A-3 Maneuvers with 45 degree pitch setpoints

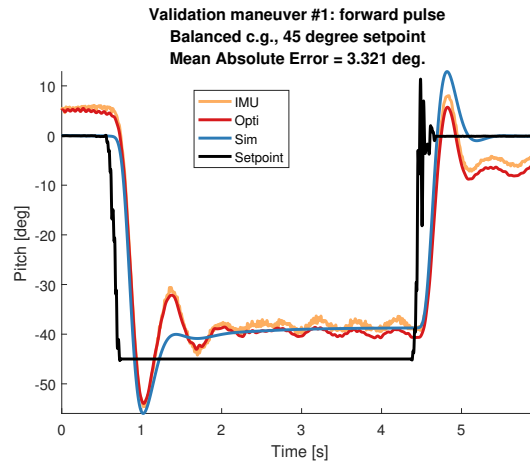


Figure A-21: First validation step maneuver with 45 degree pitch forward setpoint.

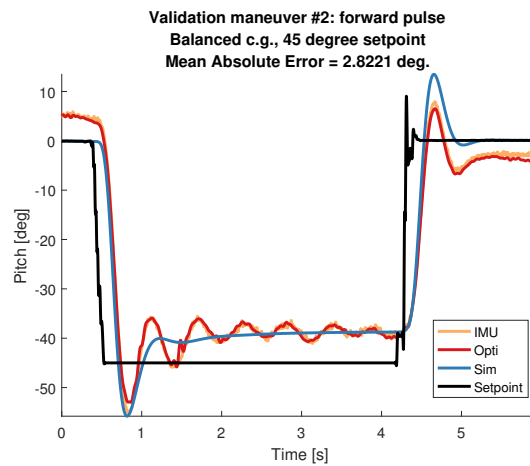


Figure A-22: Second validation step maneuver with 45 degree pitch forward setpoint.

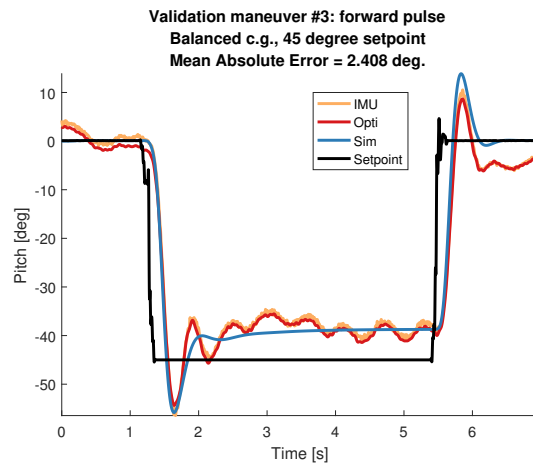


Figure A-23: Third validation step maneuver with 45 degree pitch forward setpoint.

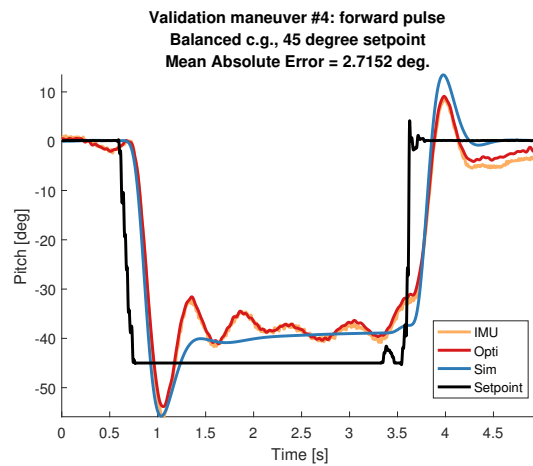


Figure A-24: Fourth validation step maneuver with 45 degree pitch forward setpoint.

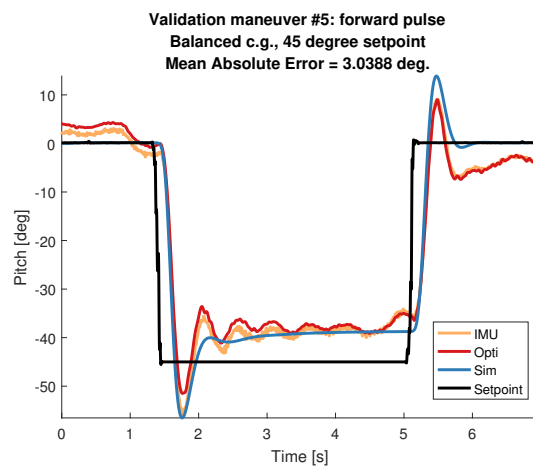


Figure A-25: Fifth validation step maneuver with 45 degree pitch forward setpoint.

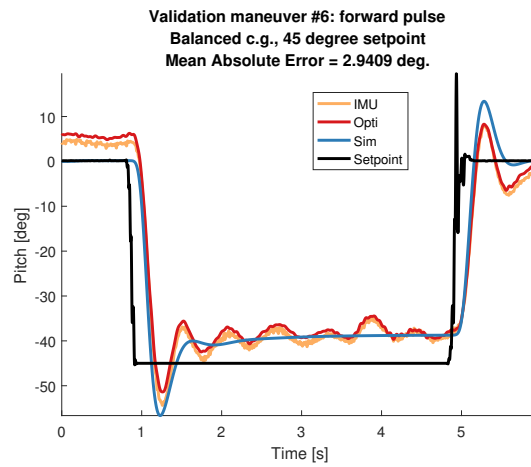


Figure A-26: Sixth validation step maneuver with 45 degree pitch forward setpoint.

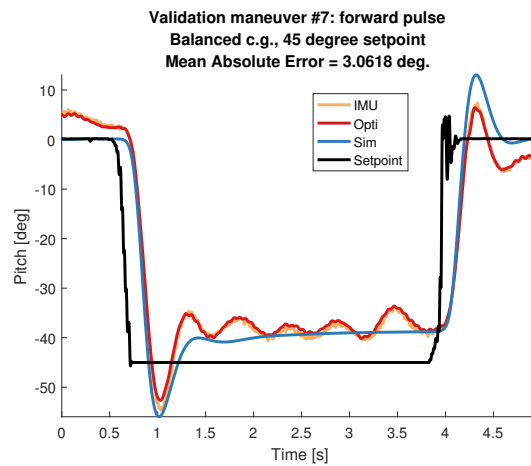


Figure A-27: Seventh validation step maneuver with 45 degree pitch forward setpoint.

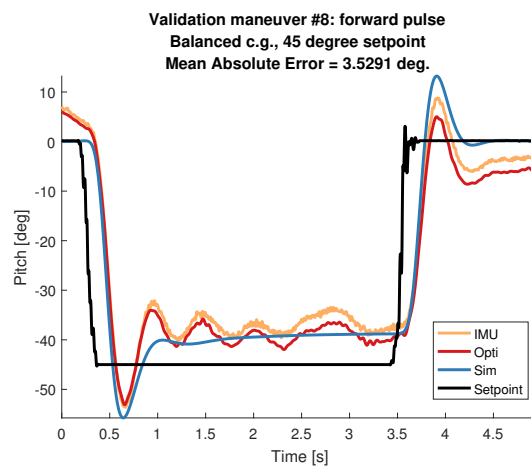


Figure A-28: Eighth validation step maneuver with 45 degree pitch forward setpoint.

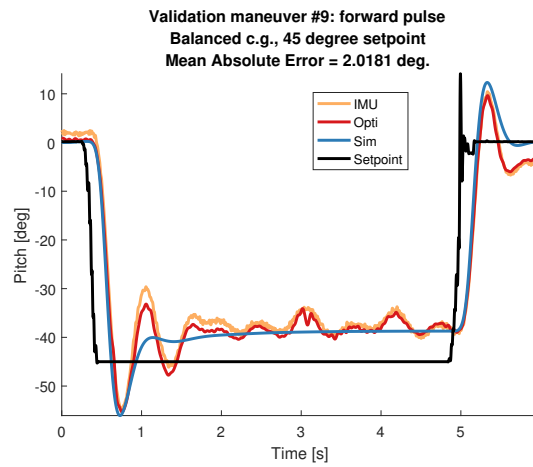


Figure A-29: Ninth validation step maneuver with 45 degree pitch forward setpoint.

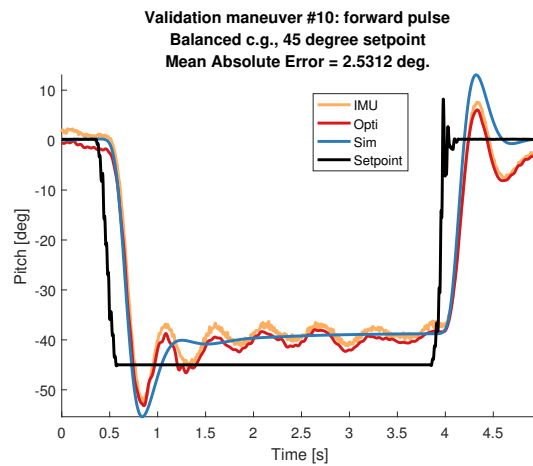


Figure A-30: Tenth validation step maneuver with 45 degree pitch forward setpoint.

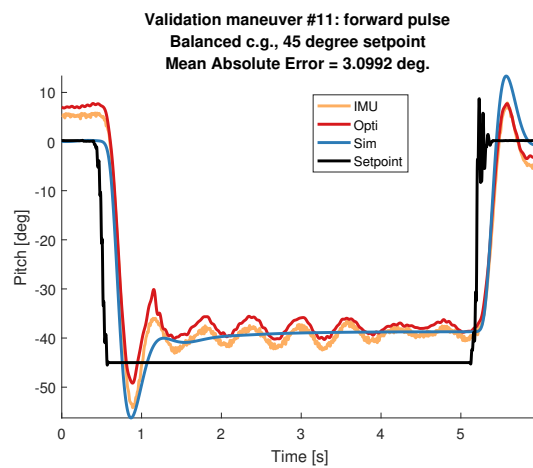


Figure A-31: Eleventh validation step maneuver with 45 degree pitch forward setpoint.

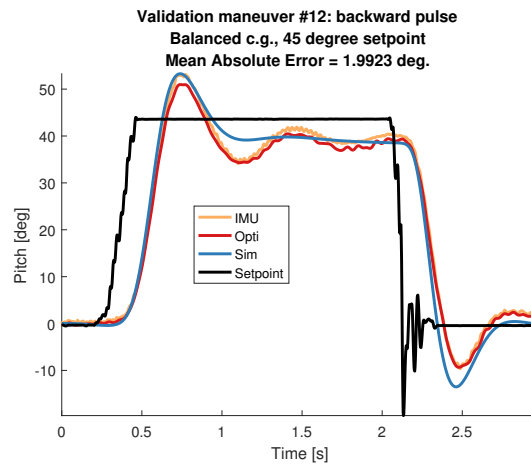


Figure A-32: First validation step maneuver with 45 degree pitch backward setpoint.

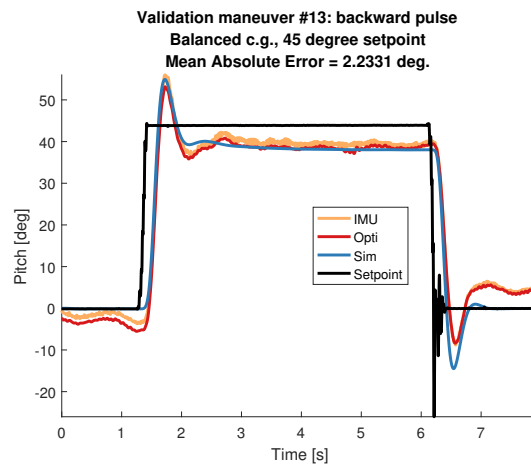


Figure A-33: Second validation step maneuver with 45 degree pitch backward setpoint.

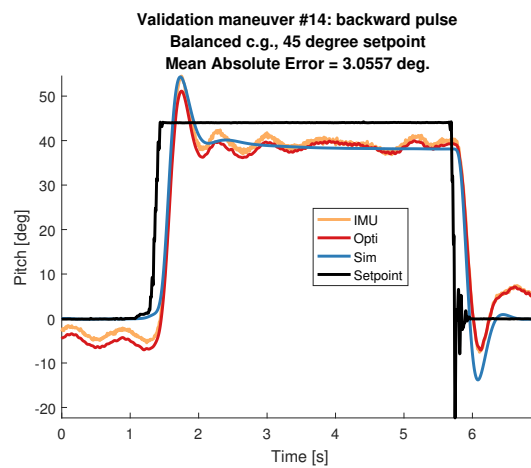


Figure A-34: Third validation step maneuver with 45 degree pitch backward setpoint.

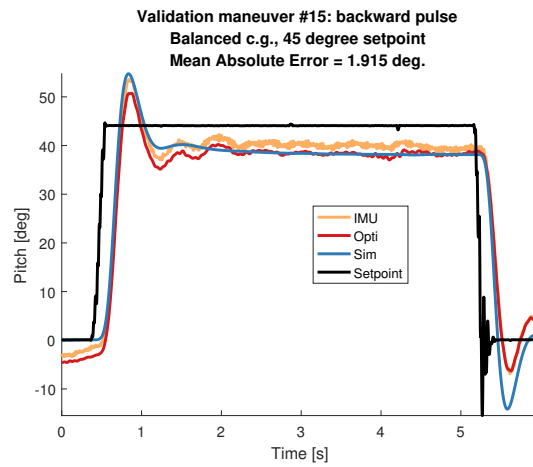


Figure A-35: Fourth validation step maneuver with 45 degree pitch backward setpoint.

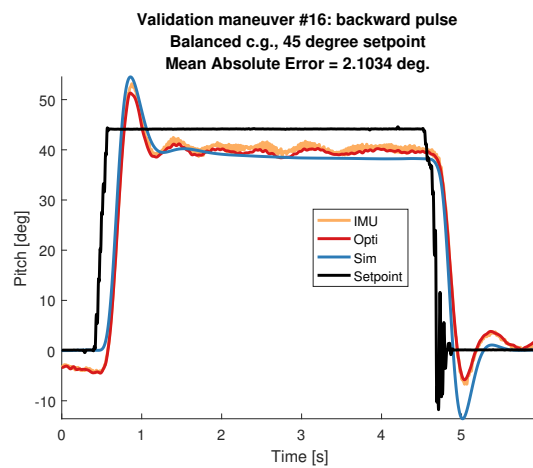


Figure A-36: Fifth validation step maneuver with 45 degree pitch backward setpoint.

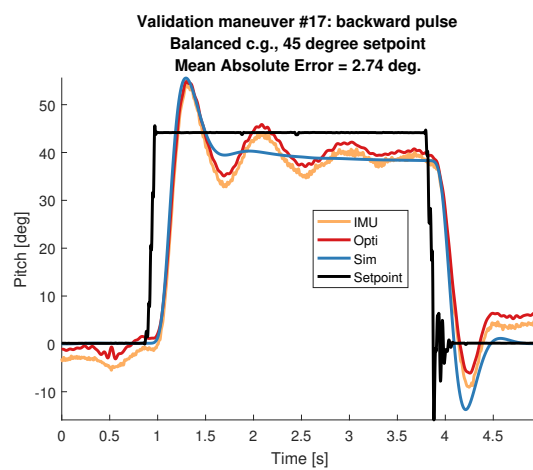


Figure A-37: Sixth validation step maneuver with 45 degree pitch backward setpoint.

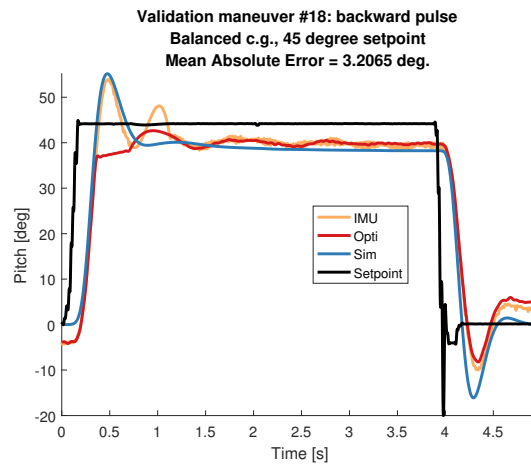


Figure A-38: Seventh validation step maneuver with 45 degree pitch backward setpoint.

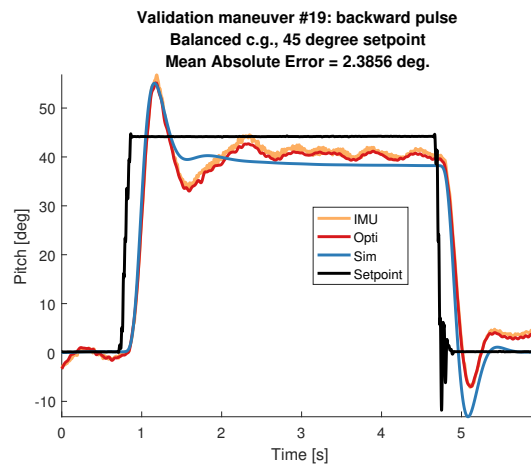


Figure A-39: Eighth validation step maneuver with 45 degree pitch backward setpoint.

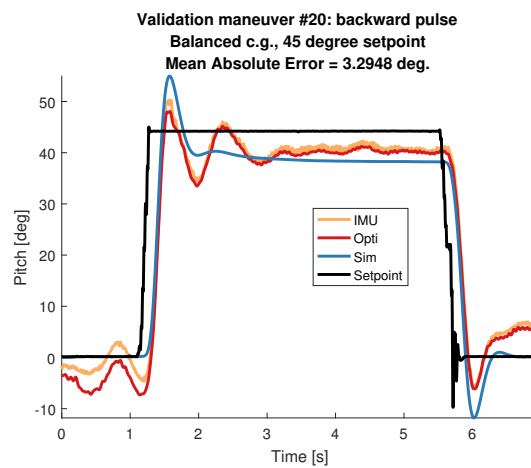


Figure A-40: Ninth validation step maneuver with 45 degree pitch backward setpoint.

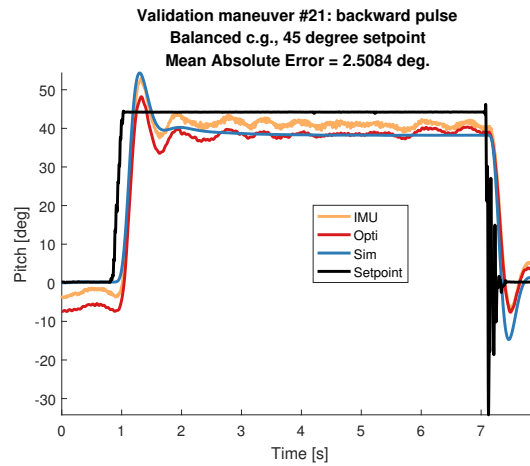


Figure A-41: Tenth validation step maneuver with 45 degree pitch backward setpoint.

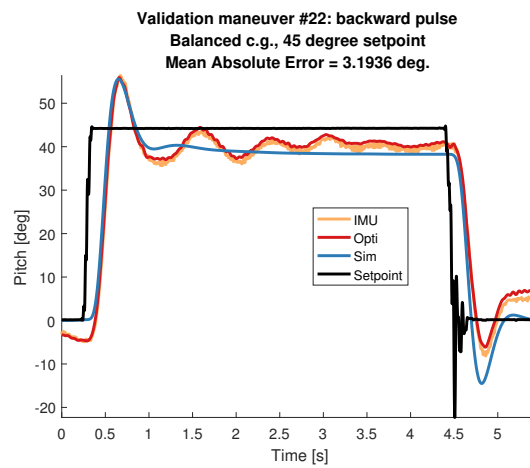


Figure A-42: Eleventh validation step maneuver with 45 degree pitch backward setpoint.

A-4 Maneuvers with 60 degree pitch setpoints

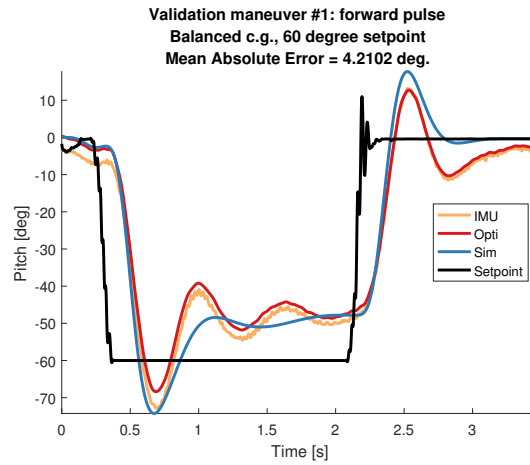


Figure A-43: First validation step maneuver with 60 degree pitch forward setpoint.

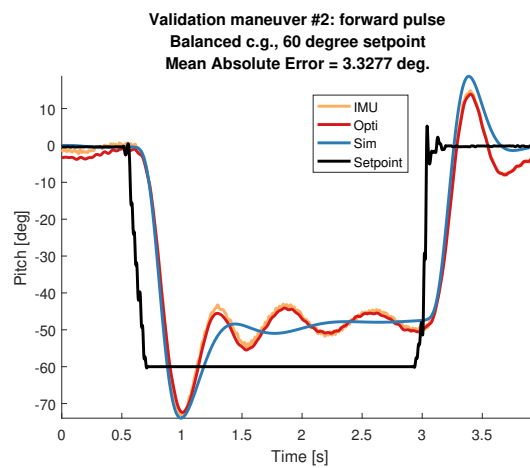


Figure A-44: Second validation step maneuver with 60 degree pitch forward setpoint.

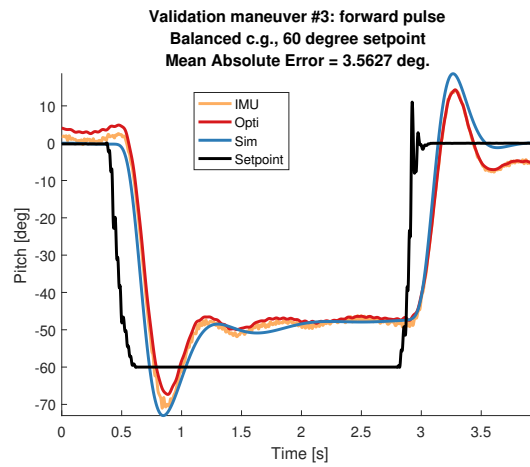


Figure A-45: Third validation step maneuver with 60 degree pitch forward setpoint.

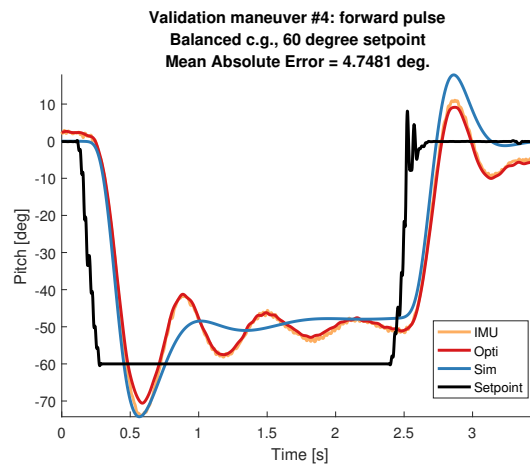


Figure A-46: Fourth validation step maneuver with 60 degree pitch forward setpoint.

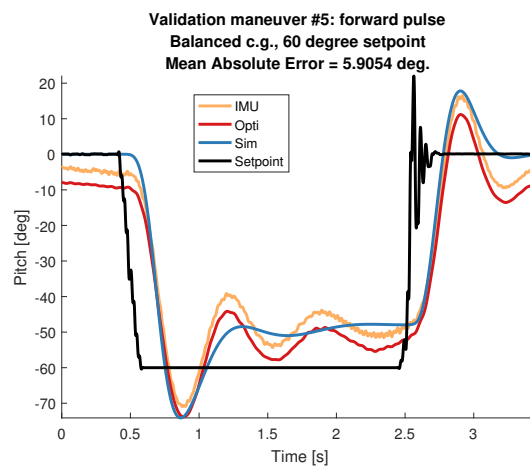


Figure A-47: Fifth validation step maneuver with 60 degree pitch forward setpoint.

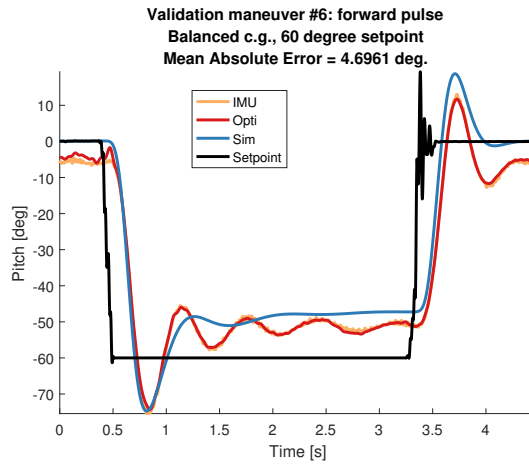


Figure A-48: Sixth validation step maneuver with 60 degree pitch forward setpoint.

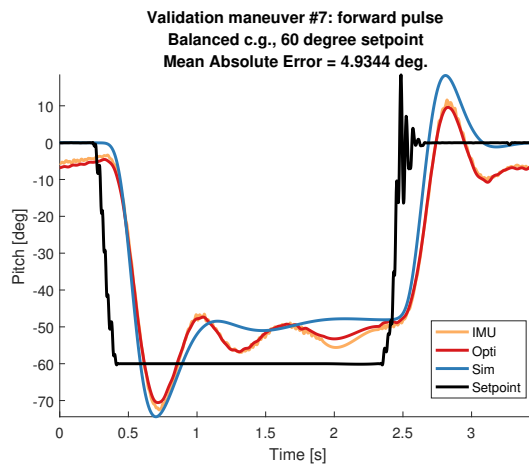


Figure A-49: Seventh validation step maneuver with 60 degree pitch forward setpoint.

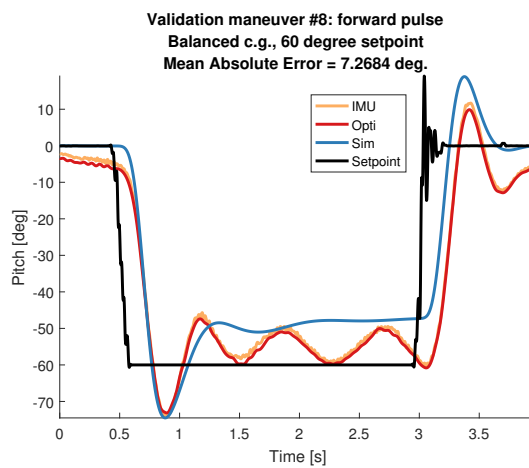


Figure A-50: Eighth validation step maneuver with 60 degree pitch forward setpoint.

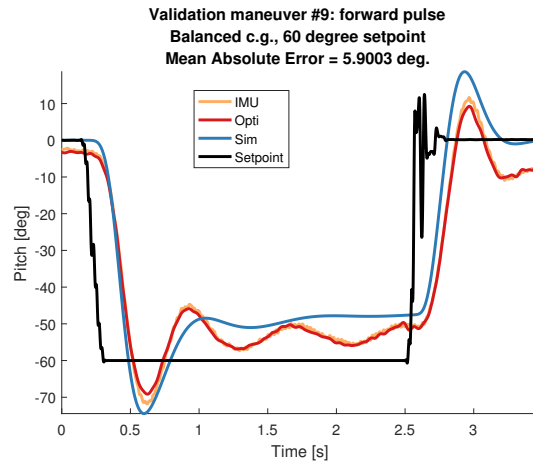


Figure A-51: Ninth validation step maneuver with 60 degree pitch forward setpoint.

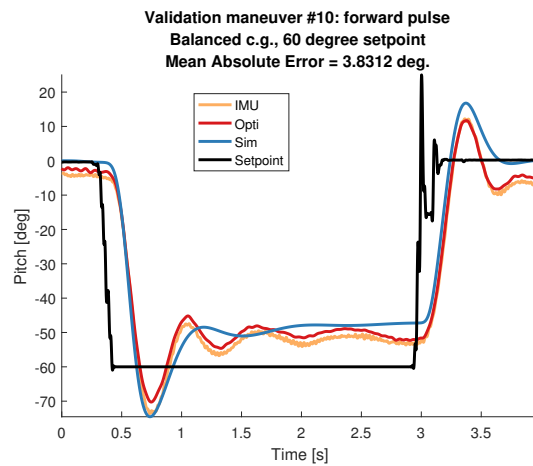


Figure A-52: Tenth validation step maneuver with 60 degree pitch forward setpoint.

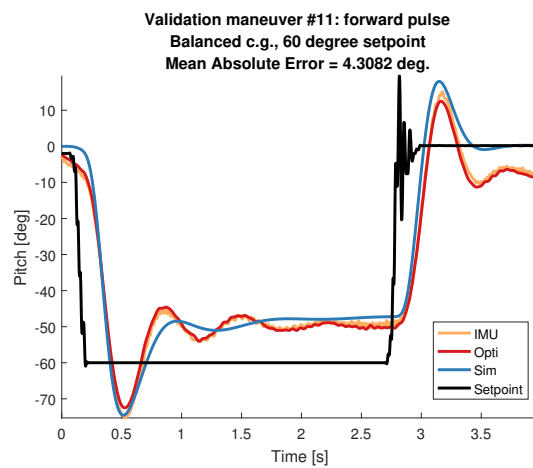


Figure A-53: Eleventh validation step maneuver with 60 degree pitch forward setpoint.

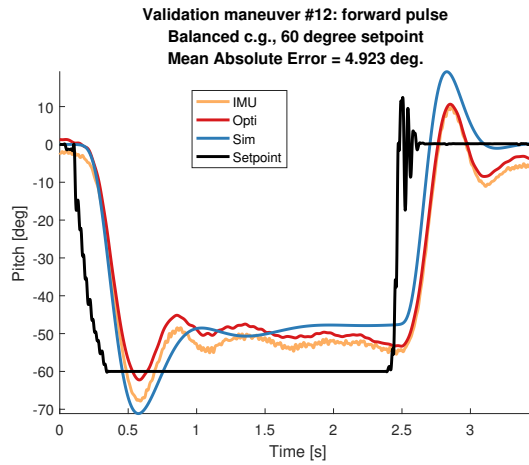


Figure A-54: Twelfth validation step maneuver with 60 degree pitch forward setpoint.

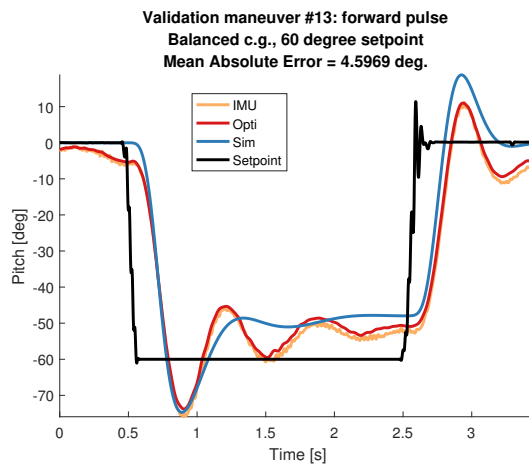


Figure A-55: Thirteenth validation step maneuver with 60 degree pitch forward setpoint.

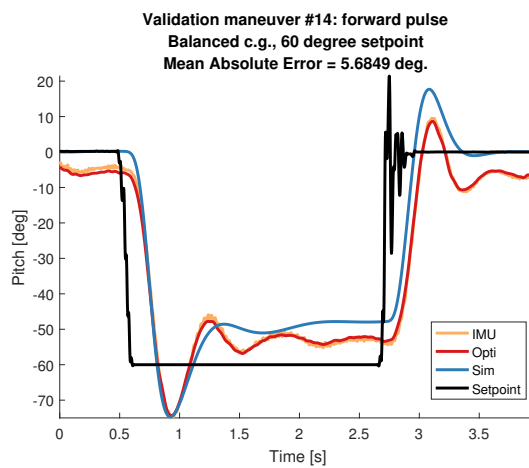


Figure A-56: Fourteenth validation step maneuver with 60 degree pitch forward setpoint.

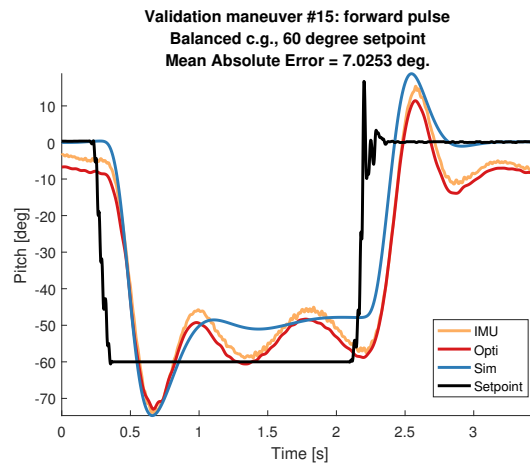


Figure A-57: Fifteenth validation step maneuver with 60 degree pitch forward setpoint.

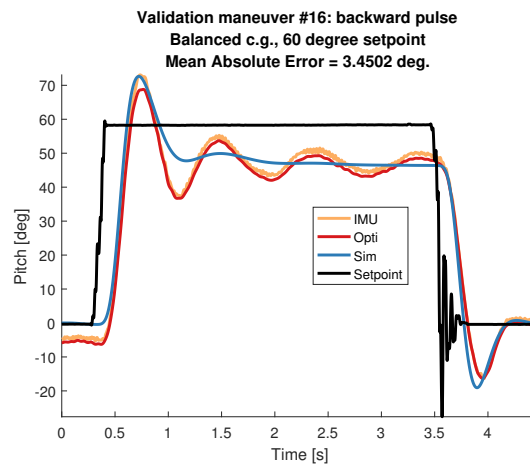


Figure A-58: First validation step maneuver with 60 degree pitch backward setpoint.

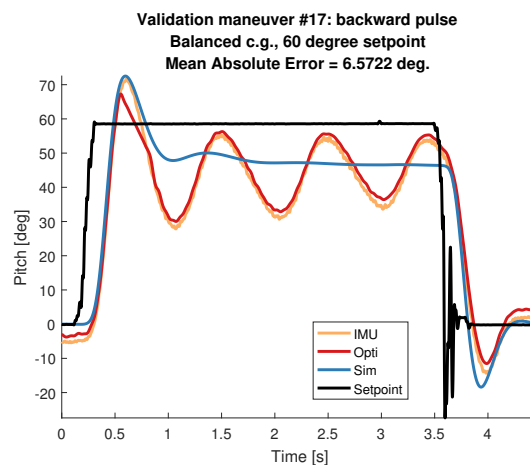


Figure A-59: Second validation step maneuver with 60 degree pitch backward setpoint.

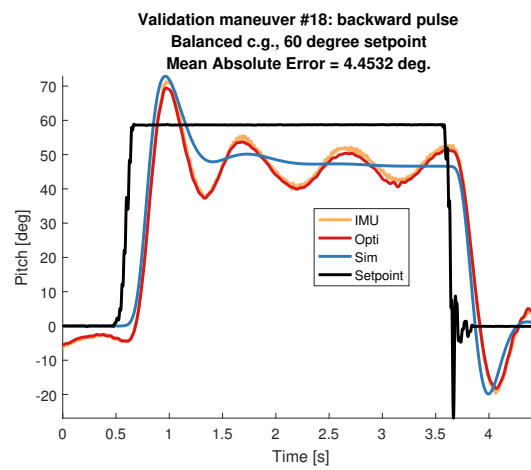


Figure A-60: Third validation step maneuver with 60 degree pitch backward setpoint.

A-5 Maneuvers with 70 degree pitch setpoints

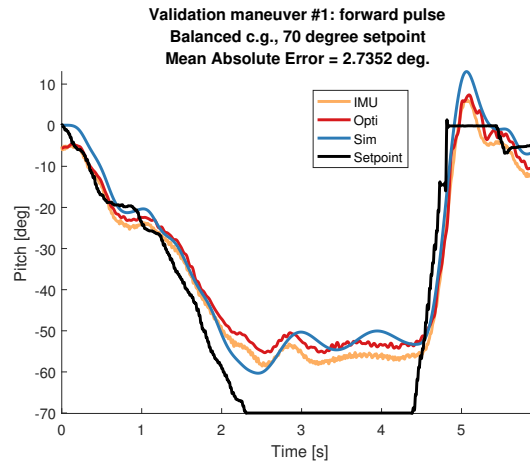


Figure A-61: First validation step maneuver with 70 degree pitch forward setpoint.

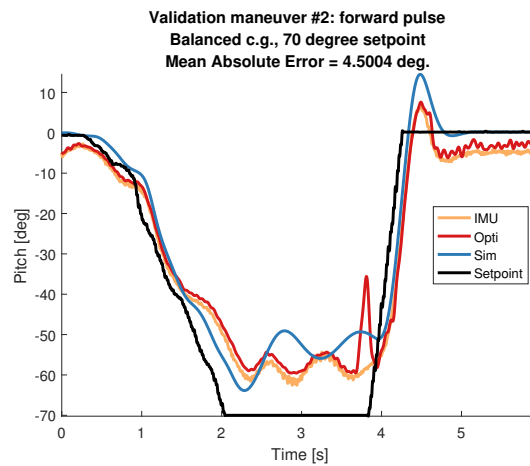


Figure A-62: Second validation step maneuver with 70 degree pitch forward setpoint.

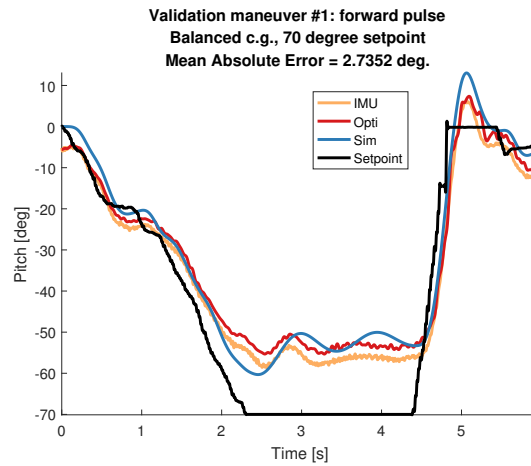


Figure A-63: Third validation step maneuver with 70 degree pitch forward setpoint.

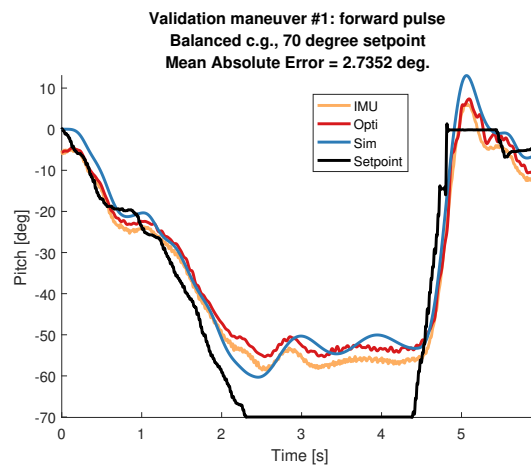


Figure A-64: Fourth validation step maneuver with 70 degree pitch forward setpoint.

A-6 Maneuvers with 80 degree pitch setpoints

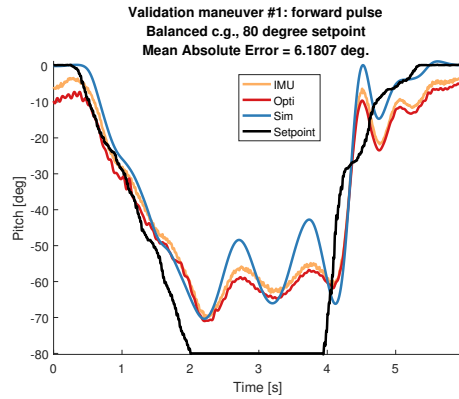


Figure A-65: First validation step maneuver with 80 degree pitch forward setpoint.

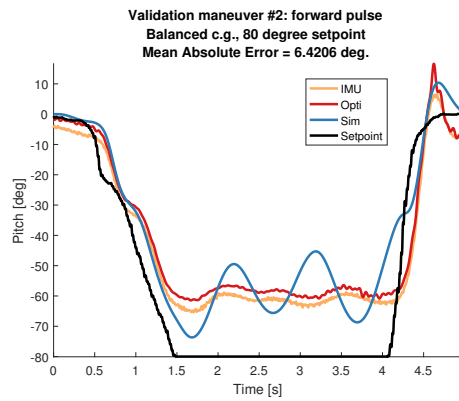


Figure A-66: Second validation step maneuver with 80 degree pitch forward setpoint.

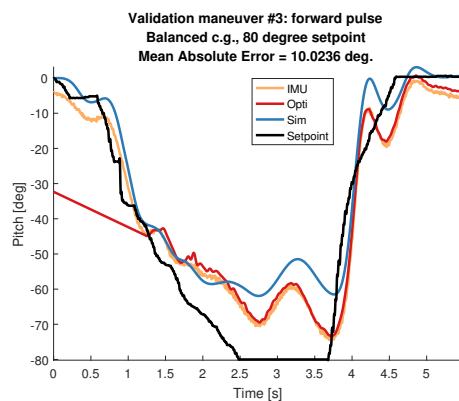


Figure A-67: Third validation step maneuver with 80 degree pitch forward setpoint.

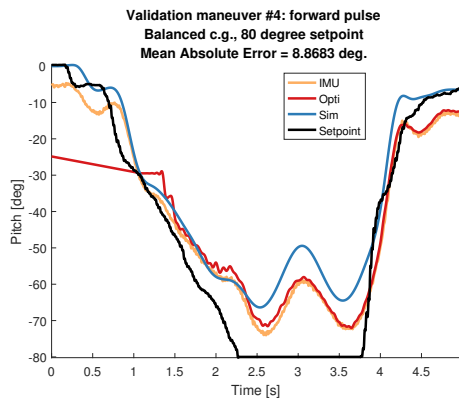


Figure A-68: Fourth validation step maneuver with 80 degree pitch forward setpoint.

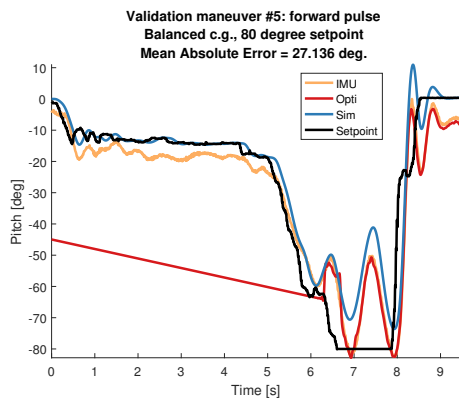


Figure A-69: Fifth validation step maneuver with 80 degree pitch forward setpoint.

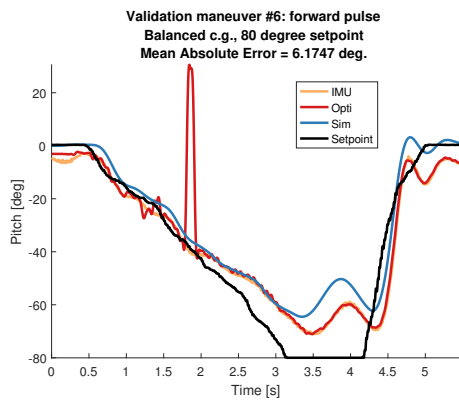


Figure A-70: Sixth validation step maneuver with 80 degree pitch forward setpoint.

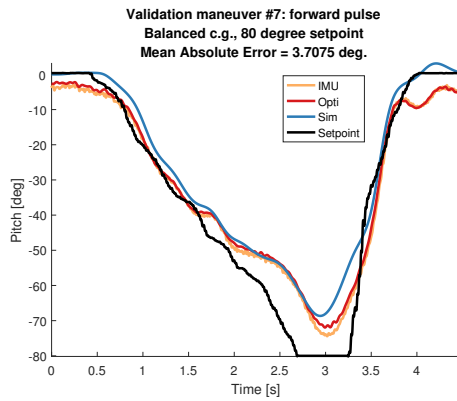


Figure A-71: Seventh validation step maneuver with 80 degree pitch forward setpoint.

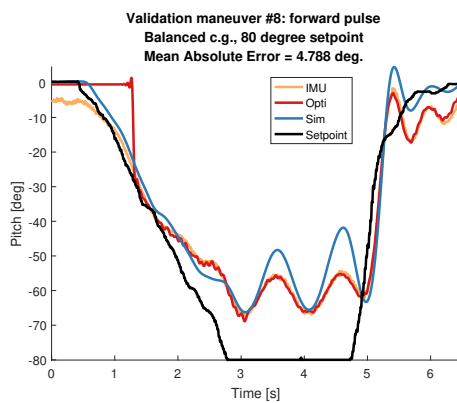


Figure A-72: Eighth validation step maneuver with 80 degree pitch forward setpoint.

Appendix B

Individual flight maneuvers - dataset II

B-1 Maneuvers with front heavy center of mass and 30 degree pitch setpoints

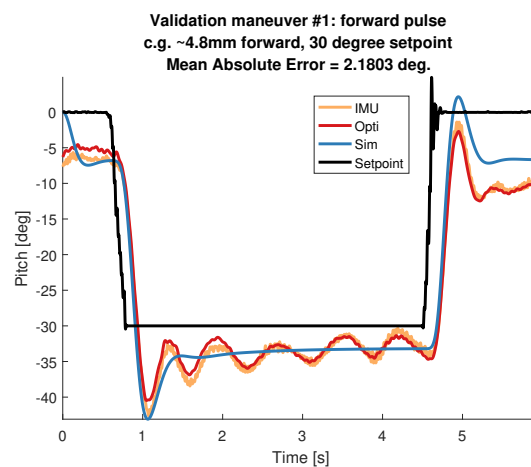


Figure B-1: First validation step maneuver with a front heavy (4.8mm) center of mass and 30 degree pitch forward setpoint.

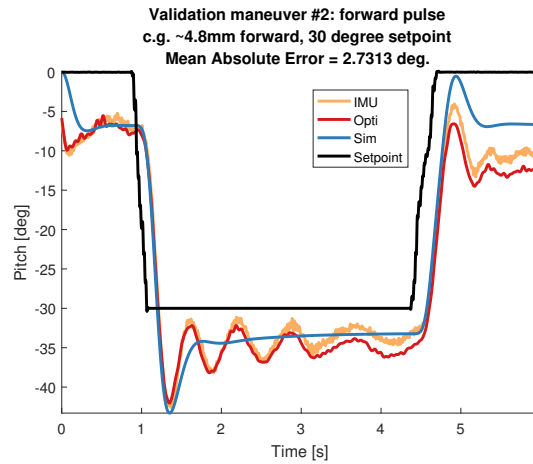


Figure B-2: Second validation step maneuver with a front heavy (4.8mm) center of mass and 30 degree pitch forward setpoint.

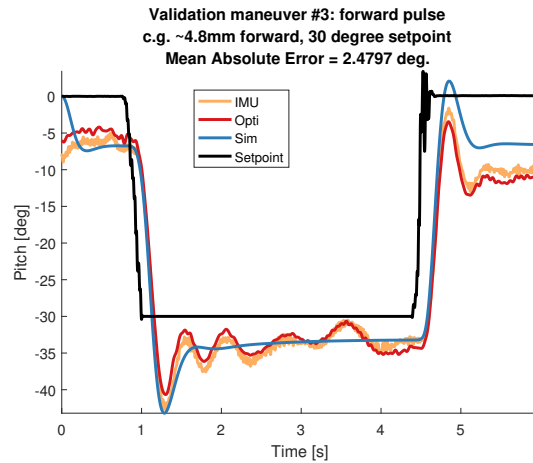


Figure B-3: Third validation step maneuver with a front heavy (4.8mm) center of mass and 30 degree pitch forward setpoint.

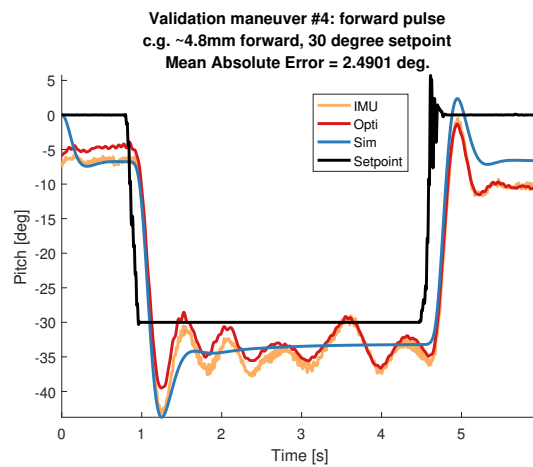


Figure B-4: Fourth validation step maneuver with a front heavy (4.8mm) center of mass and 30 degree pitch forward setpoint.

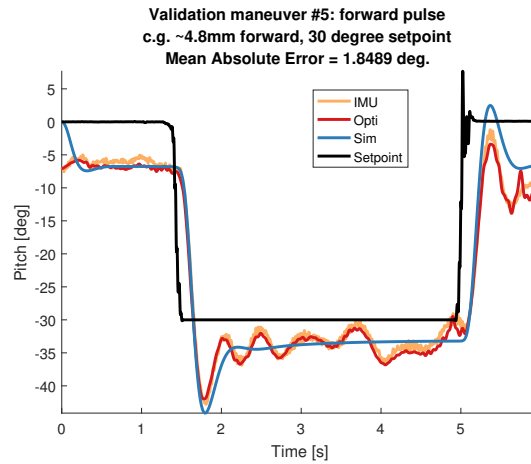


Figure B-5: Fifth validation step maneuver with a front heavy (4.8mm) center of mass and 30 degree pitch forward setpoint.

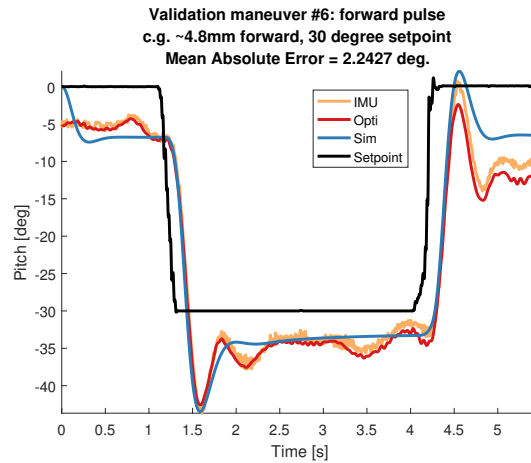


Figure B-6: Sixth validation step maneuver with a front heavy (4.8mm) center of mass and 30 degree pitch forward setpoint.

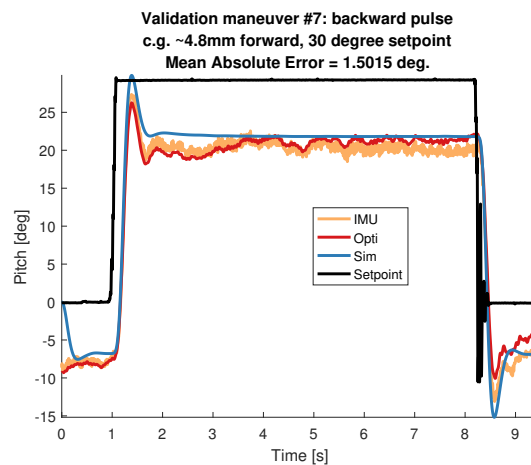


Figure B-7: First validation step maneuver with a front heavy (4.8mm) center of mass and 30 degree pitch backward setpoint.

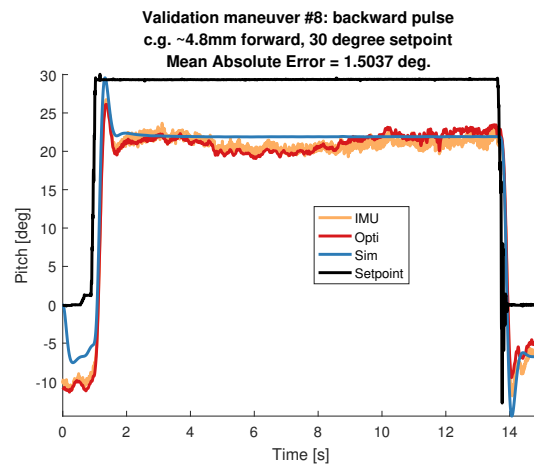


Figure B-8: Second validation step maneuver with a front heavy (4.8mm) center of mass and 30 degree pitch backward setpoint.

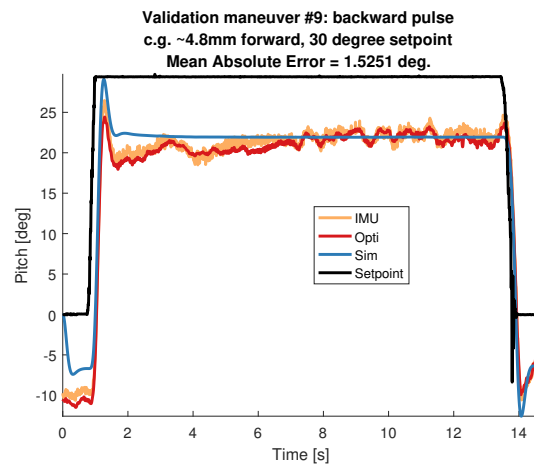


Figure B-9: Third validation step maneuver with a front heavy (4.8mm) center of mass and 30 degree pitch backward setpoint.

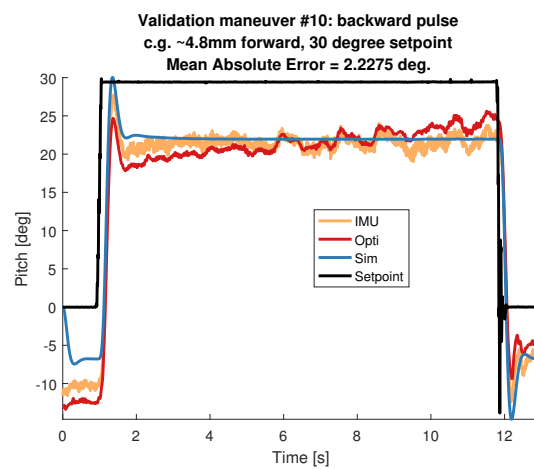


Figure B-10: Fourth validation step maneuver with a front heavy (4.8mm) center of mass and 30 degree pitch backward setpoint.

B-1 Maneuvers with front heavy center of mass and 30 degree pitch setpoints⁸⁵

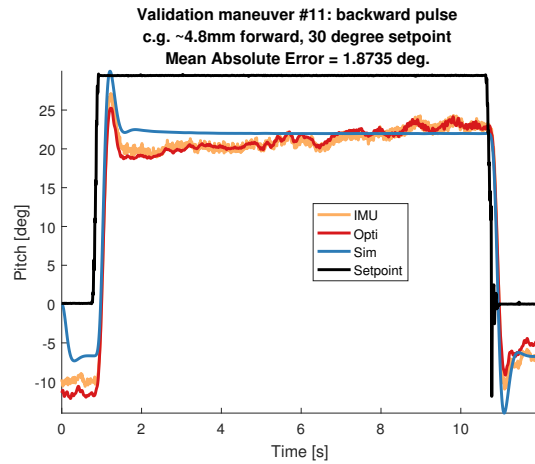


Figure B-11: Fifth validation step maneuver with a front heavy (4.8mm) center of mass and 30 degree pitch backward setpoint.

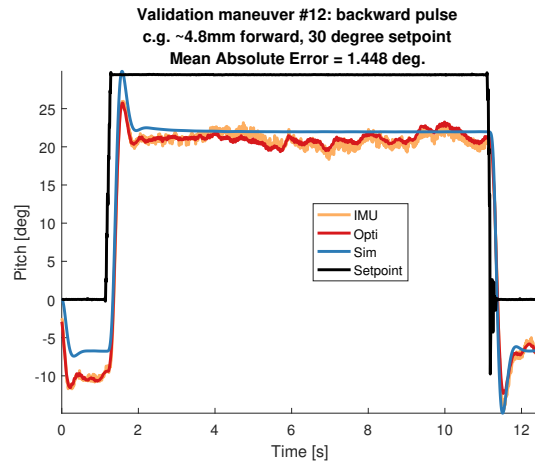


Figure B-12: Sixth validation step maneuver with a front heavy (4.8mm) center of mass and 30 degree pitch backward setpoint.

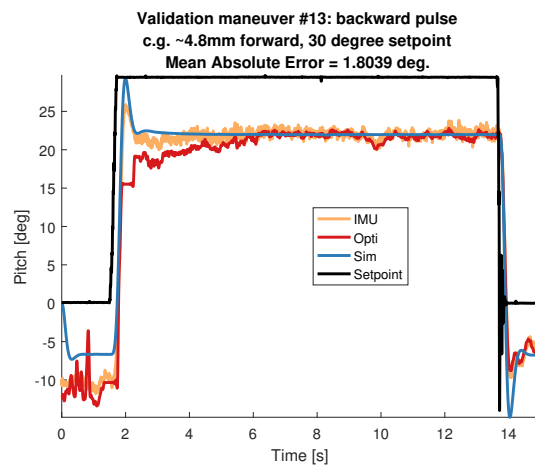


Figure B-13: Seventh validation step maneuver with a front heavy (4.8mm) center of mass and 30 degree pitch backward setpoint.

B-2 Maneuvers with bottom heavy center of mass and 30 degree pitch setpoints

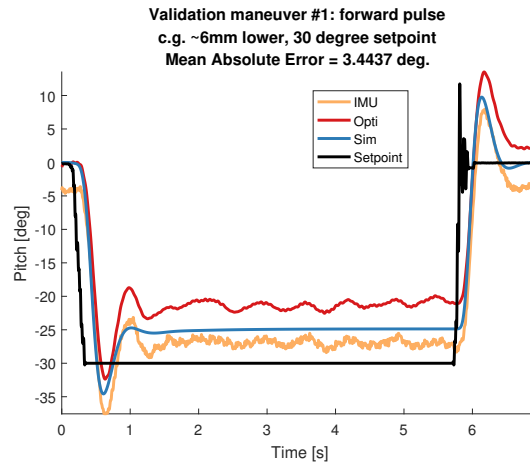


Figure B-14: First validation step maneuver with a bottom heavy (6mm) center of mass and 30 degree pitch forward setpoint.

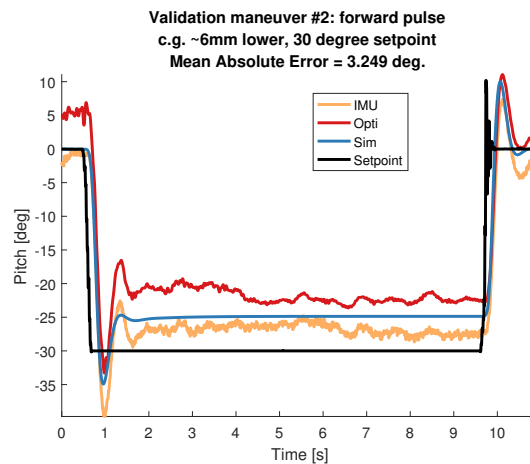


Figure B-15: Second validation step maneuver with a bottom heavy (6mm) center of mass and 30 degree pitch forward setpoint.

B-2 Maneuvers with bottom heavy center of mass and 30 degree pitch setpoints

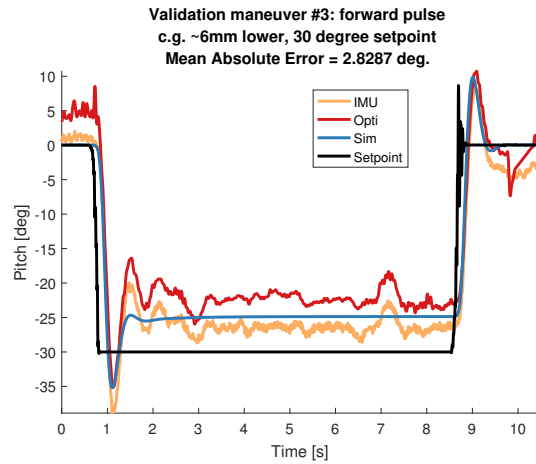


Figure B-16: Third validation step maneuver with a bottom heavy (6mm) center of mass and 30 degree pitch forward setpoint.

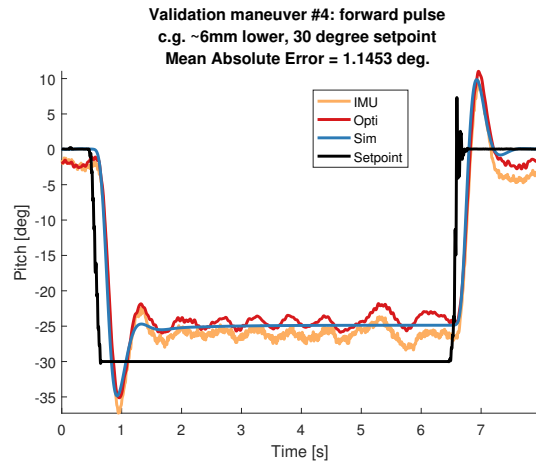


Figure B-17: Fourth validation step maneuver with a bottom heavy (6mm) center of mass and 30 degree pitch forward setpoint.

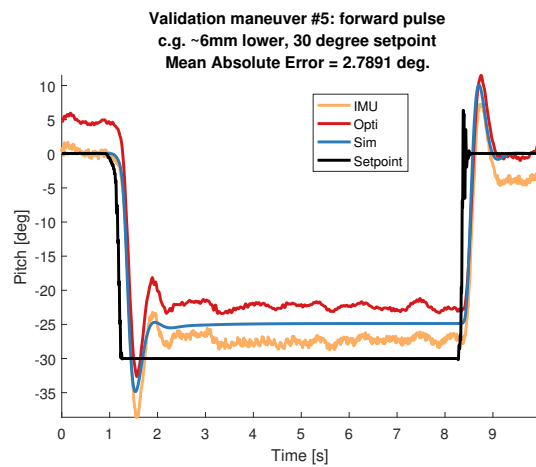


Figure B-18: Fifth validation step maneuver with a bottom heavy (6mm) center of mass and 30 degree pitch forward setpoint.

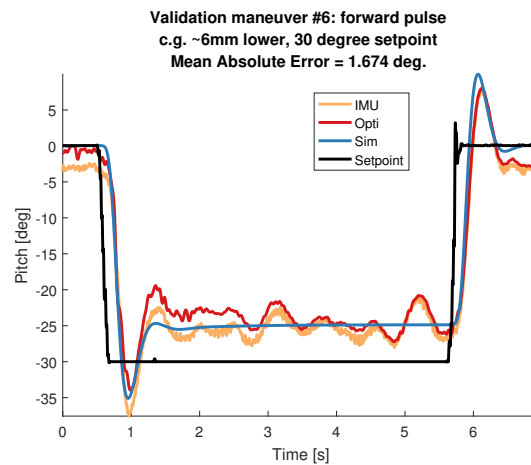


Figure B-19: Sixth validation step maneuver with a bottom heavy (6mm) center of mass and 30 degree pitch forward setpoint.

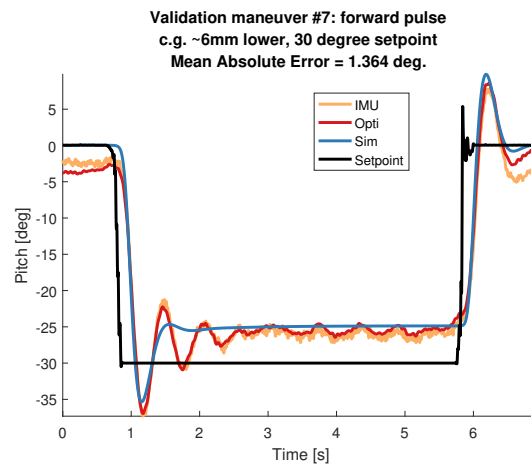


Figure B-20: Seventh validation step maneuver with a bottom heavy (6mm) center of mass and 30 degree pitch forward setpoint.

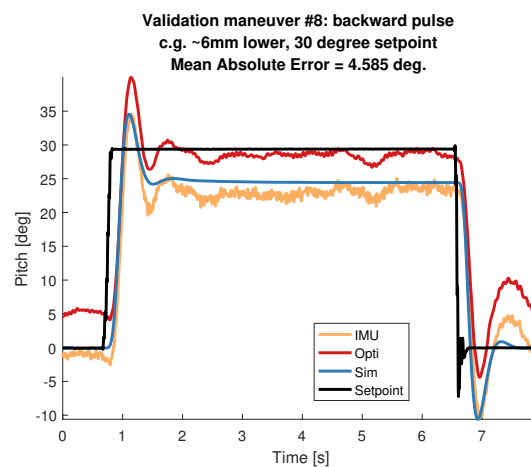


Figure B-21: First validation step maneuver with a bottom heavy (6mm) center of mass and 30 degree pitch backward setpoint.

B-2 Maneuvers with bottom heavy center of mass and 30 degree pitch setpoint

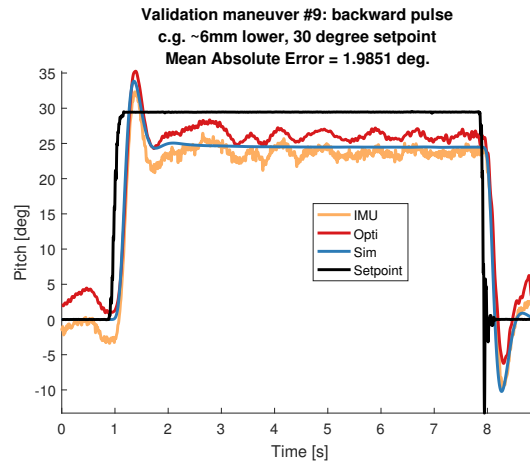


Figure B-22: Second validation step maneuver with a bottom heavy (6mm) center of mass and 30 degree pitch backward setpoint.

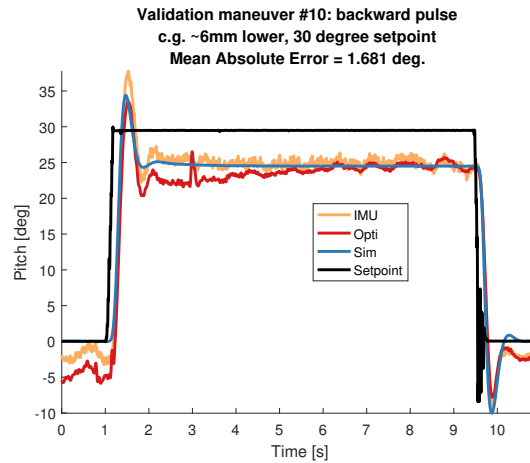


Figure B-23: Third validation step maneuver with a bottom heavy (6mm) center of mass and 30 degree pitch backward setpoint.

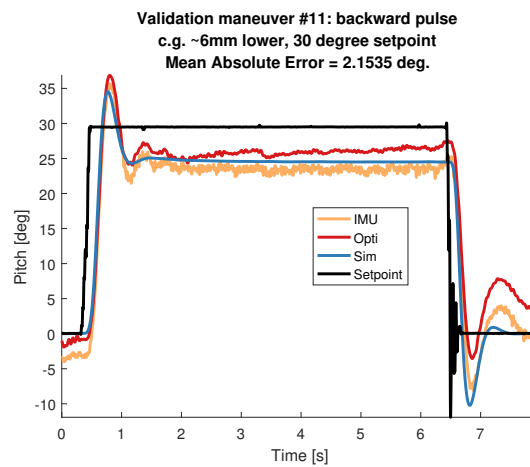


Figure B-24: Fourth validation step maneuver with a bottom heavy (6mm) center of mass and 30 degree pitch backward setpoint.

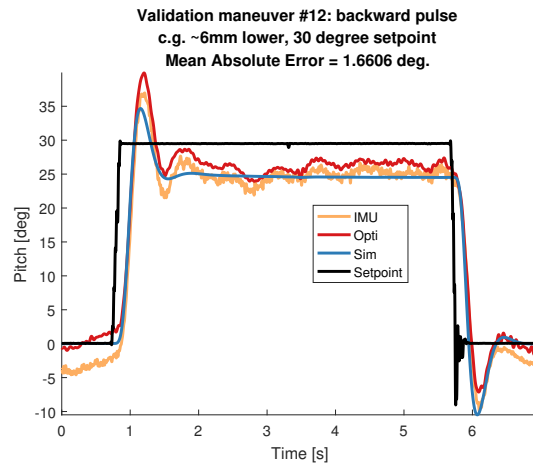


Figure B-25: Fifth validation step maneuver with a bottom heavy (6mm) center of mass and 30 degree pitch backward setpoint.

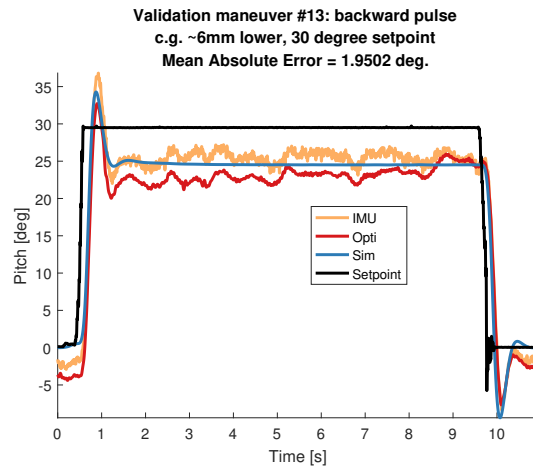


Figure B-26: Sixth validation step maneuver with a bottom heavy (6mm) center of mass and 30 degree pitch backward setpoint.

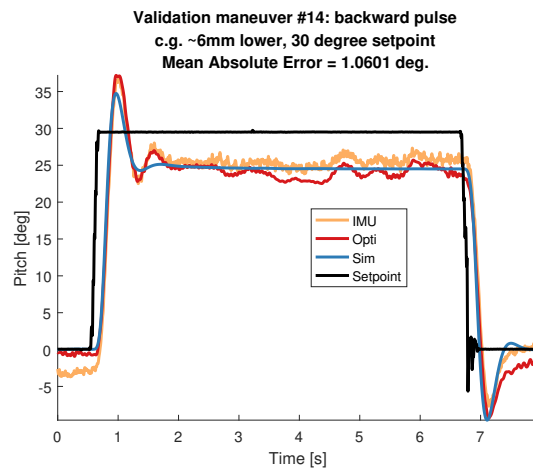


Figure B-27: Seventh validation step maneuver with a bottom heavy (6mm) center of mass and 30 degree pitch backward setpoint.

Individual flight maneuvers - dataset III

C-1 Maneuvers with 40 degree pitch setpoints, baseline controller

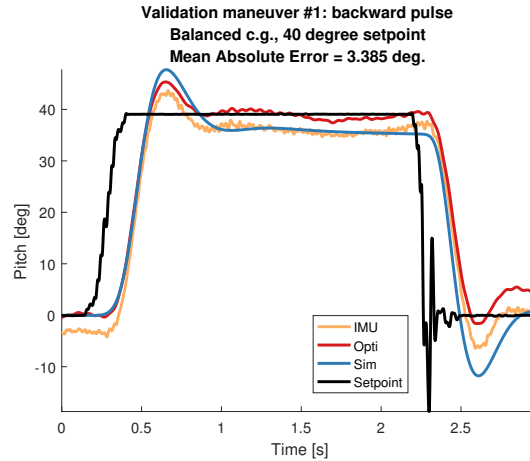


Figure C-1: First validation step maneuver with baseline controller and 40 degree pitch backward setpoint.

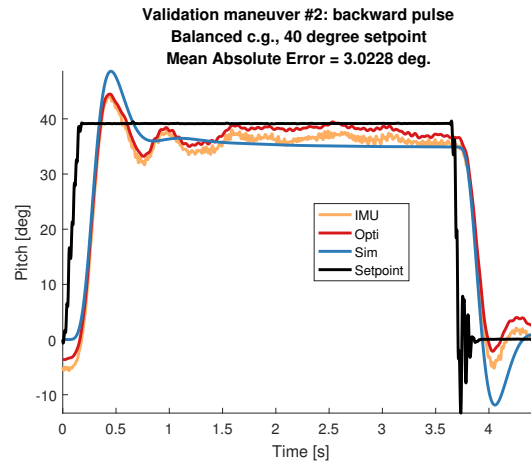


Figure C-2: Second validation step maneuver with baseline controller and 40 degree pitch backward setpoint.

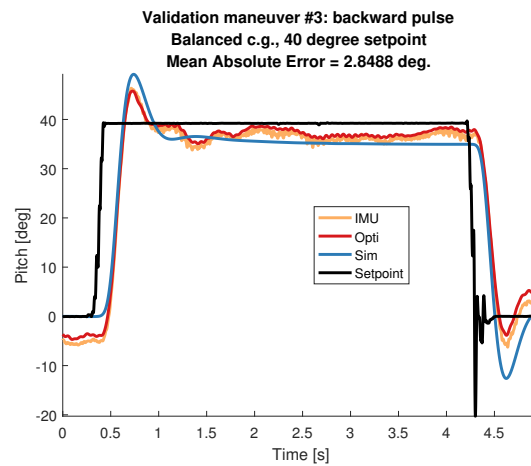


Figure C-3: Third validation step maneuver with baseline controller and 40 degree pitch backward setpoint.

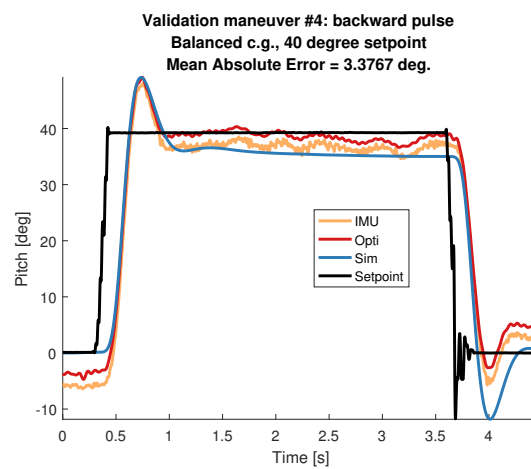


Figure C-4: Fourth validation step maneuver with baseline controller and 40 degree pitch backward setpoint.

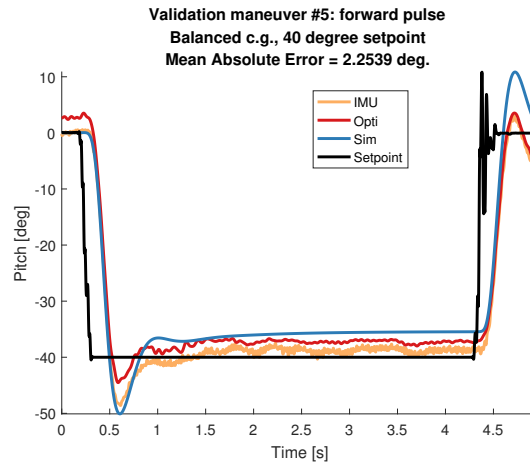


Figure C-5: First validation step maneuver with baseline controller and 40 degree pitch forward setpoint.

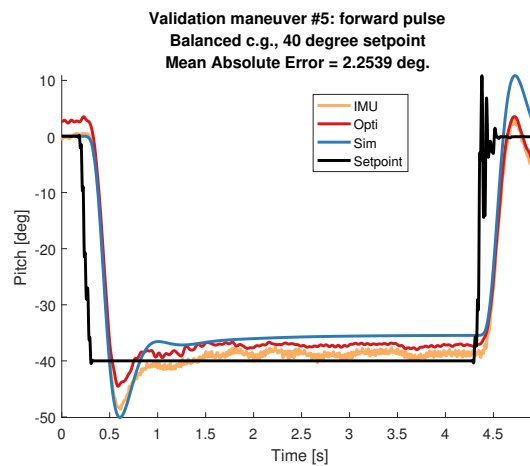


Figure C-6: Second validation step maneuver with baseline controller and 40 degree pitch forward setpoint.

C-2 Maneuvers with 40 degree pitch setpoints, command filter cutoff 10 Hz

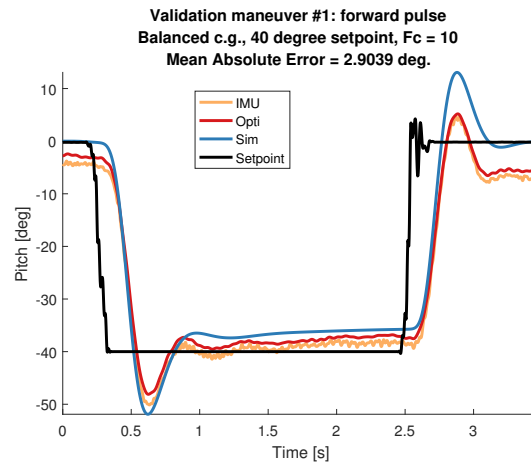


Figure C-7: First validation step maneuver with 10 Hz command filter cutoff frequency and 40 degree pitch forward setpoint.

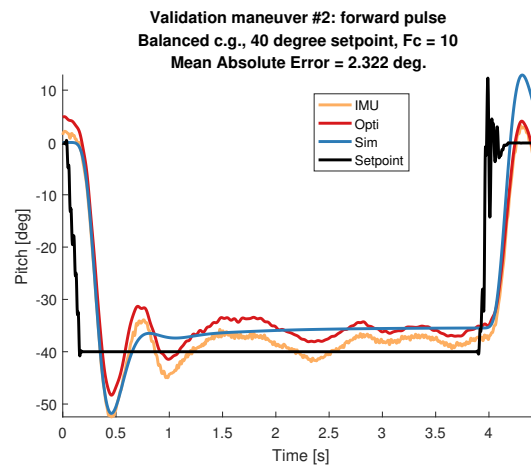


Figure C-8: Second validation step maneuver with 10 Hz command filter cutoff frequency and 40 degree pitch forward setpoint.

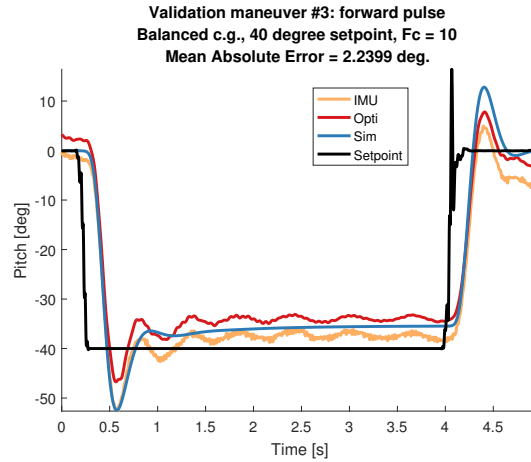


Figure C-9: Third validation step maneuver with 10 Hz command filter cutoff frequency and 40 degree pitch forward setpoint.

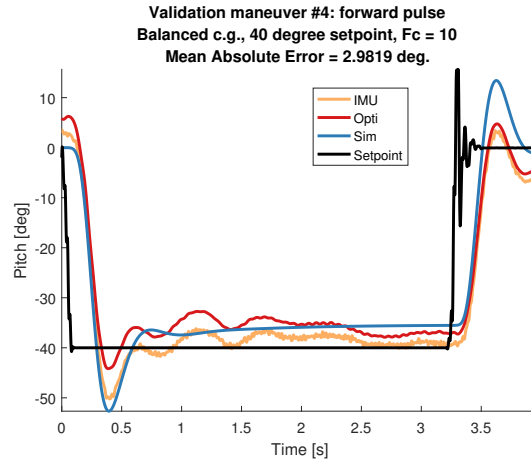


Figure C-10: Fourth validation step maneuver with 10 Hz command filter cutoff frequency and 40 degree pitch forward setpoint.

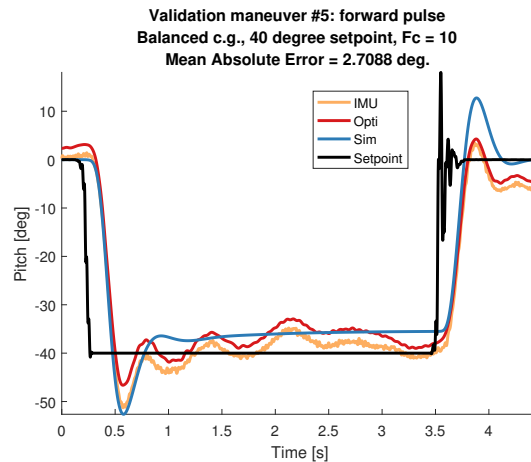


Figure C-11: Fifth validation step maneuver with 10 Hz command filter cutoff frequency and 40 degree pitch forward setpoint.

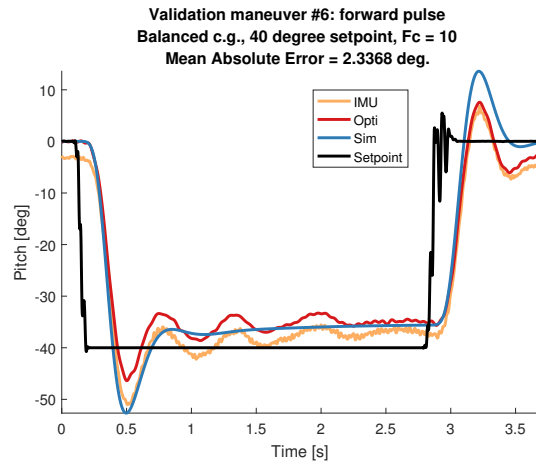


Figure C-12: Sixth validation step maneuver with 10 Hz command filter cutoff frequency and 40 degree pitch forward setpoint.

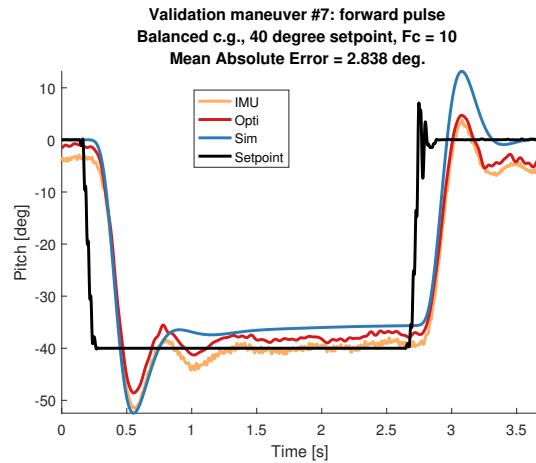


Figure C-13: Seventh validation step maneuver with 10 Hz command filter cutoff frequency and 40 degree pitch forward setpoint.

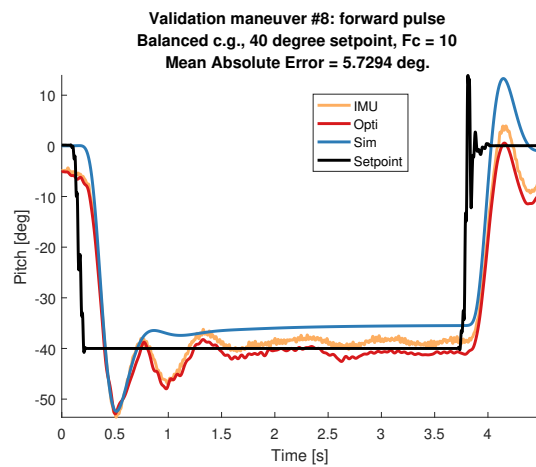


Figure C-14: Eighth validation step maneuver with 10 Hz command filter cutoff frequency and 40 degree pitch forward setpoint.

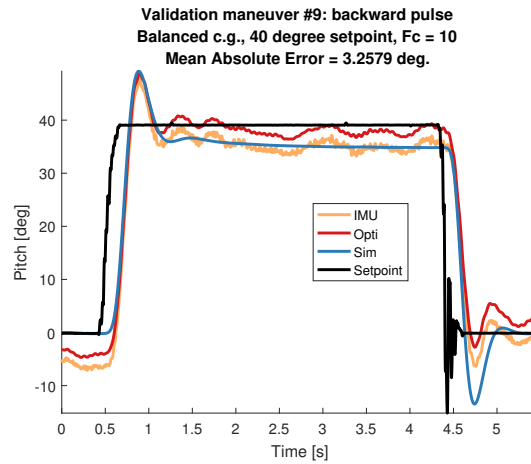


Figure C-15: First validation step maneuver with 10 Hz command filter cutoff frequency and 40 degree pitch backward setpoint.

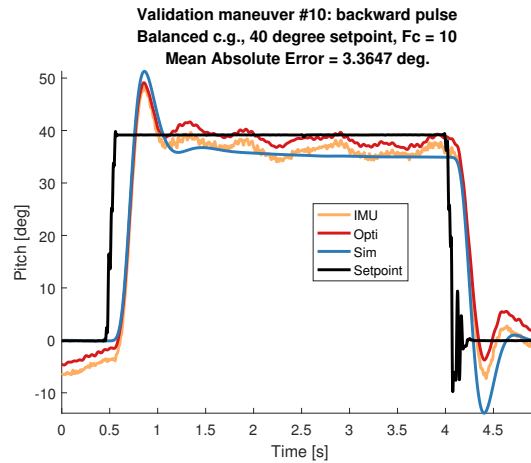


Figure C-16: Second validation step maneuver with 10 Hz command filter cutoff frequency and 40 degree pitch backward setpoint.

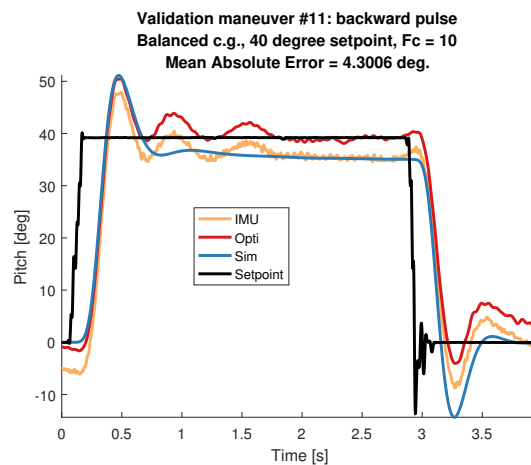


Figure C-17: Third validation step maneuver with 10 Hz command filter cutoff frequency and 40 degree pitch backward setpoint.

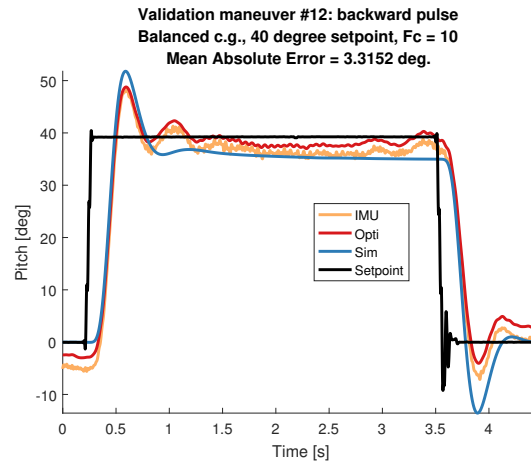


Figure C-18: Fourth validation step maneuver with 10 Hz command filter cutoff frequency and 40 degree pitch backward setpoint.

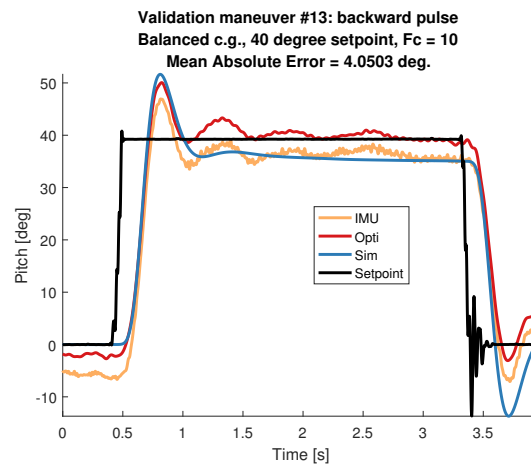


Figure C-19: Fifth validation step maneuver with 10 Hz command filter cutoff frequency and 40 degree pitch backward setpoint.

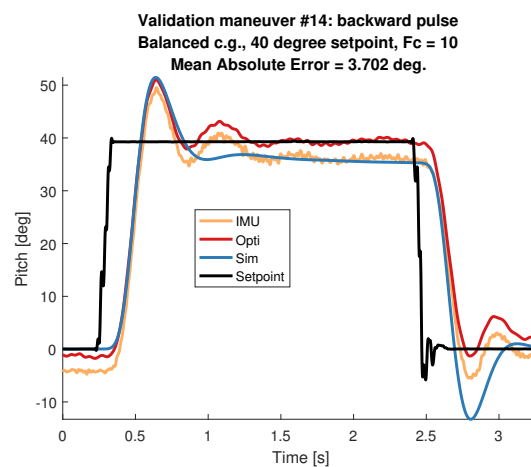


Figure C-20: Sixth validation step maneuver with 10 Hz command filter cutoff frequency and 40 degree pitch backward setpoint.

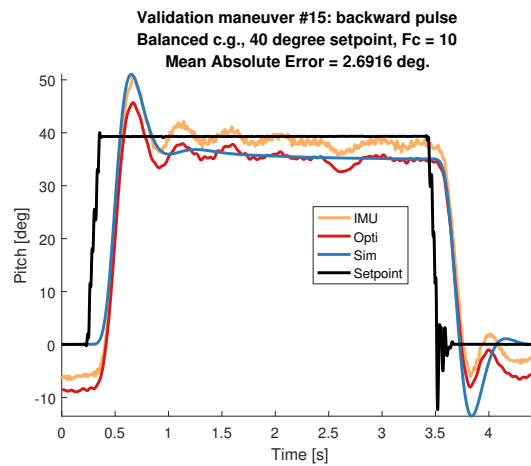


Figure C-21: Seventh validation step maneuver with 10 Hz command filter cutoff frequency and 40 degree pitch backward setpoint.

C-3 Maneuvers with 40 degree pitch setpoints, command filter cutoff 256 Hz

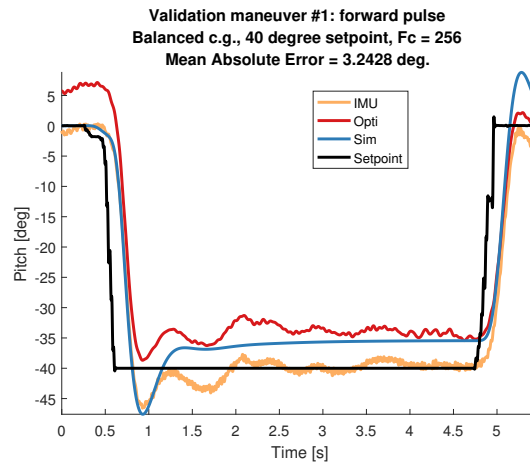


Figure C-22: First validation step maneuver with 256 Hz command filter cutoff frequency and 40 degree pitch forward setpoint.

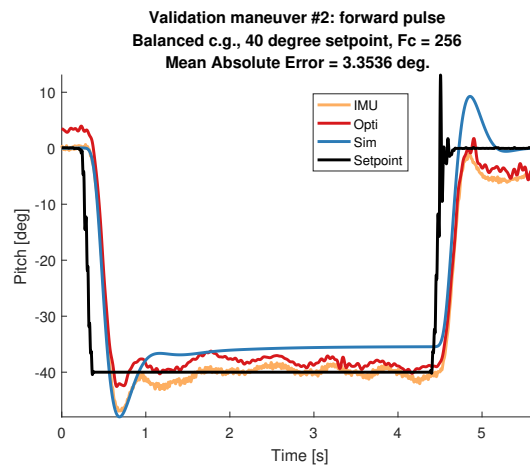


Figure C-23: Second validation step maneuver with 256 Hz command filter cutoff frequency and 40 degree pitch forward setpoint.

C-3 Maneuvers with 40 degree pitch setpoints, command filter cutoff 256 Hz

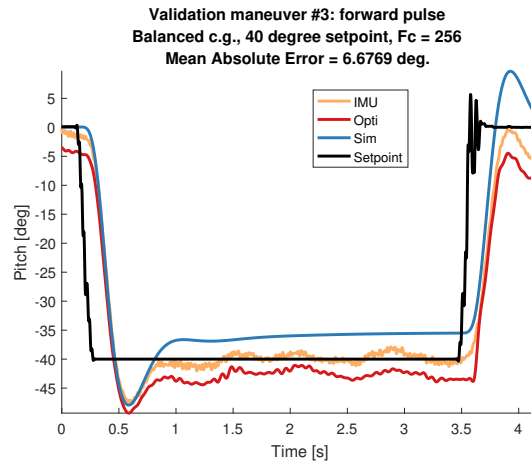


Figure C-24: Third validation step maneuver with 256 Hz command filter cutoff frequency and 40 degree pitch forward setpoint.

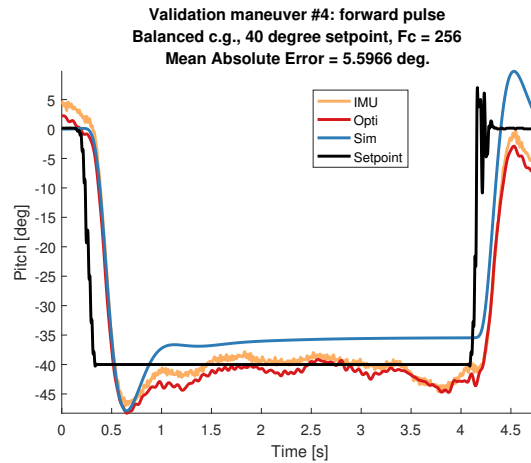


Figure C-25: Fourth validation step maneuver with 256 Hz command filter cutoff frequency and 40 degree pitch forward setpoint.

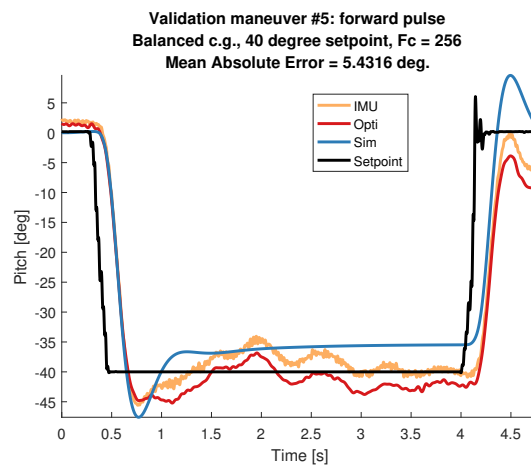


Figure C-26: Fifth validation step maneuver with 256 Hz command filter cutoff frequency and 40 degree pitch forward setpoint.

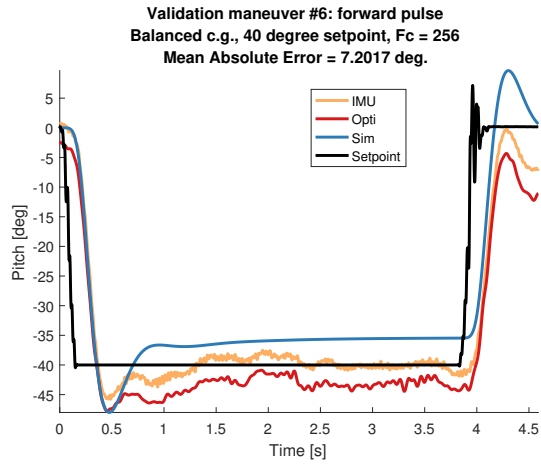


Figure C-27: Sixth validation step maneuver with 256 Hz command filter cutoff frequency and 40 degree pitch forward setpoint.

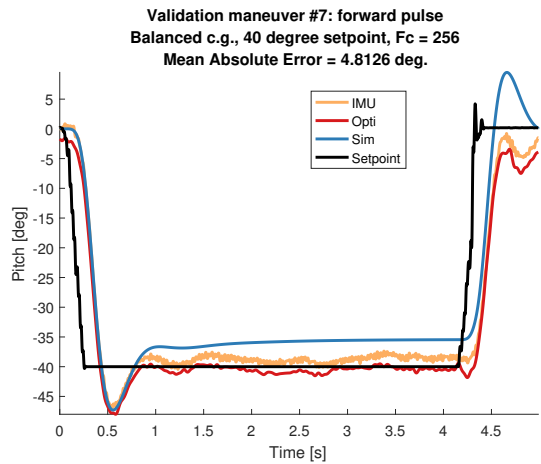


Figure C-28: Seventh validation step maneuver with 256 Hz command filter cutoff frequency and 40 degree pitch forward setpoint.

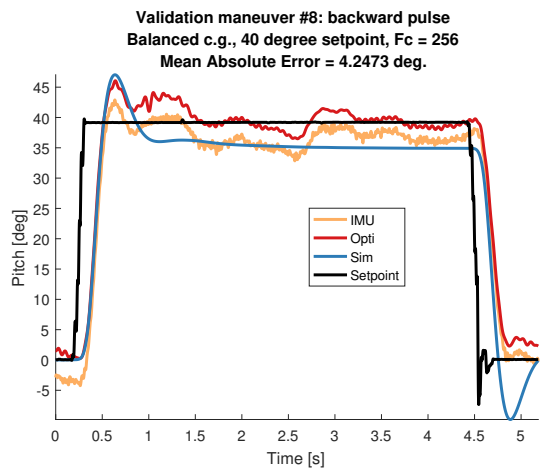


Figure C-29: First validation step maneuver with 256 Hz command filter cutoff frequency and 40 degree pitch backward setpoint.

C-3 Maneuvers with 40 degree pitch setpoints, command filter cutoff 256 Hz¹⁰³

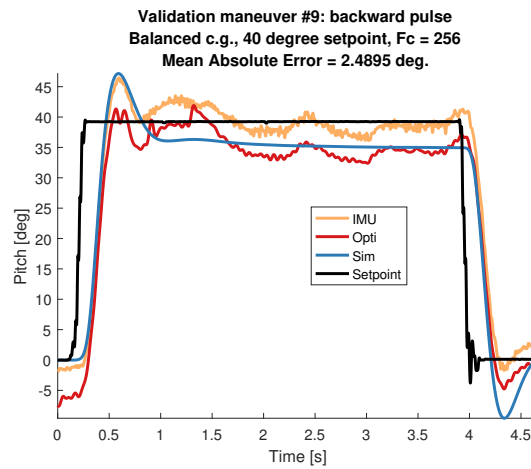


Figure C-30: Second validation step maneuver with 256 Hz command filter cutoff frequency and 40 degree pitch backward setpoint.

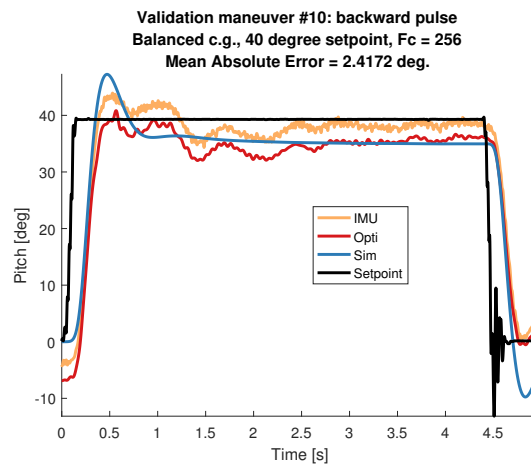


Figure C-31: Third validation step maneuver with 256 Hz command filter cutoff frequency and 40 degree pitch backward setpoint.

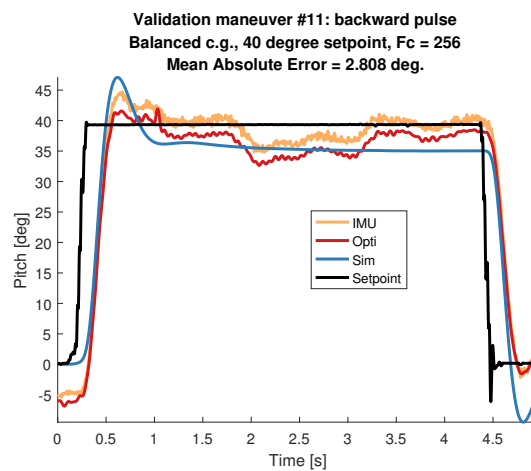


Figure C-32: Fourth validation step maneuver with 256 Hz command filter cutoff frequency and 40 degree pitch backward setpoint.

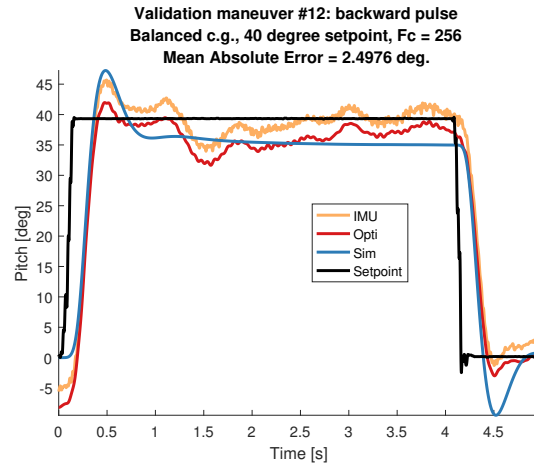


Figure C-33: Fifth validation step maneuver with 256 Hz command filter cutoff frequency and 40 degree pitch backward setpoint.

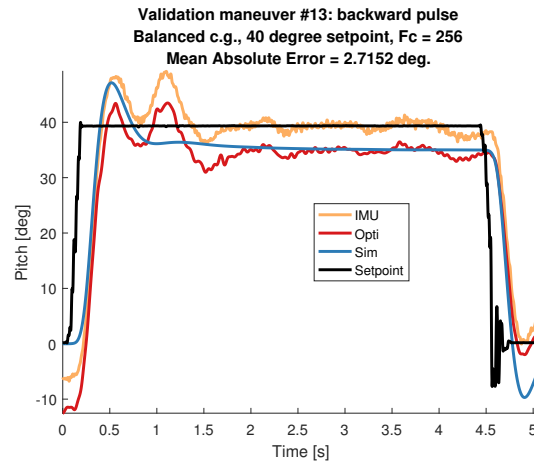


Figure C-34: Sixth validation step maneuver with 256 Hz command filter cutoff frequency and 40 degree pitch backward setpoint.

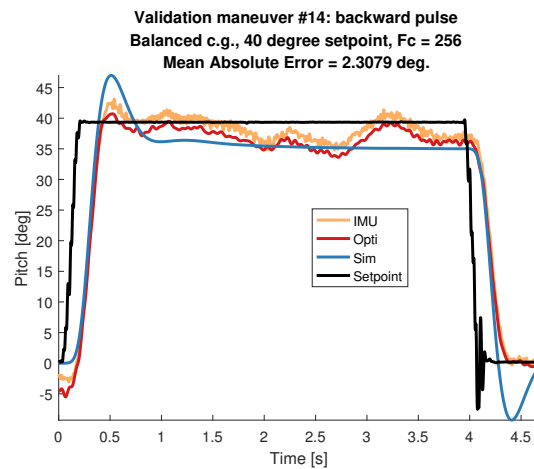


Figure C-35: Seventh validation step maneuver with 256 Hz command filter cutoff frequency and 40 degree pitch backward setpoint.

C-4 Maneuvers with 40 degree pitch setpoints, rate feedback gain 600

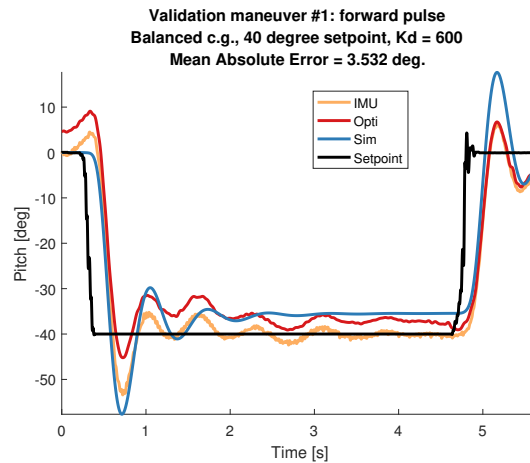


Figure C-36: First validation step maneuver with rate feedback 600 (PPRZ units) and 40 degree pitch forward setpoint.

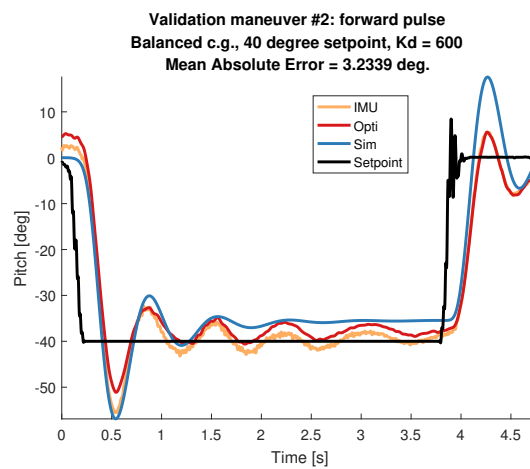


Figure C-37: Second validation step maneuver with rate feedback 600 (PPRZ units) and 40 degree pitch forward setpoint.

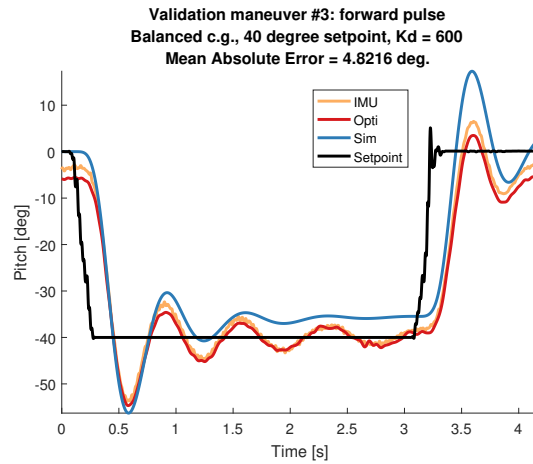


Figure C-38: Third validation step maneuver with rate feedback 600 (PPRZ units) and 40 degree pitch forward setpoint.

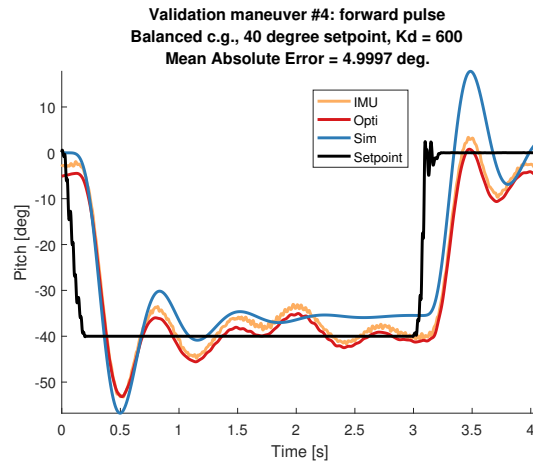


Figure C-39: Fourth validation step maneuver with rate feedback 600 (PPRZ units) and 40 degree pitch forward setpoint.

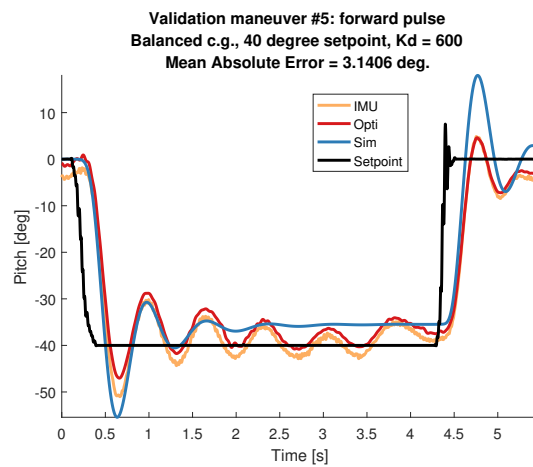


Figure C-40: Fifth validation step maneuver with rate feedback 600 (PPRZ units) and 40 degree pitch forward setpoint.

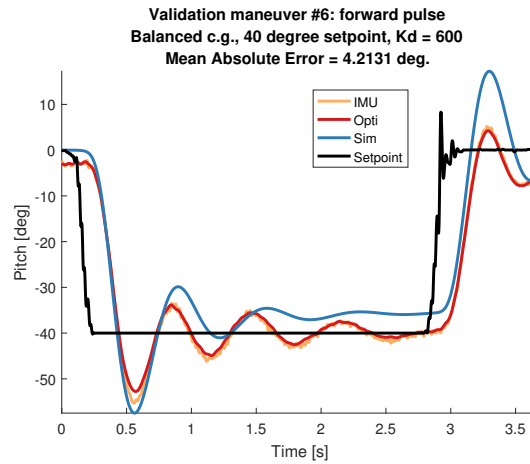


Figure C-41: Sixth validation step maneuver with rate feedback 600 (PPRZ units) and 40 degree pitch forward setpoint.

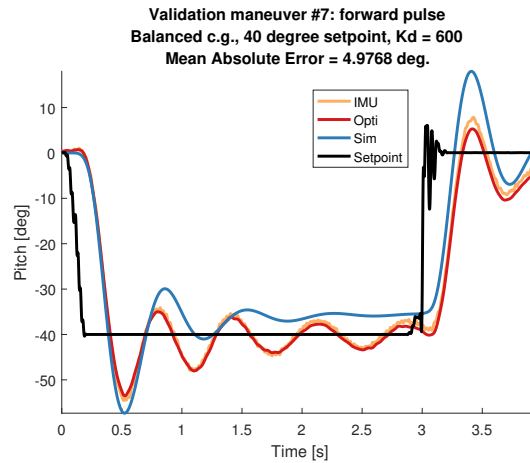


Figure C-42: Seventh validation step maneuver with rate feedback 600 (PPRZ units) and 40 degree pitch forward setpoint.

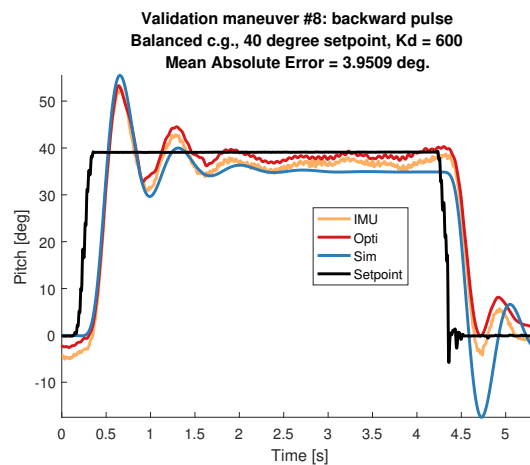


Figure C-43: First validation step maneuver with rate feedback 600 (PPRZ units) and 40 degree pitch backward setpoint.

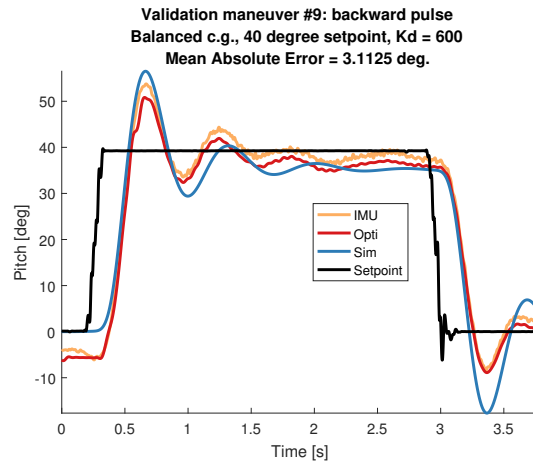


Figure C-44: Second validation step maneuver with rate feedback 600 (PPRZ units) and 40 degree pitch backward setpoint.

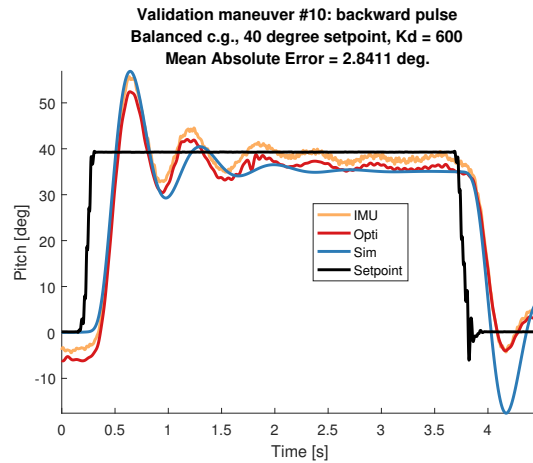


Figure C-45: Third validation step maneuver with rate feedback 600 (PPRZ units) and 40 degree pitch backward setpoint.

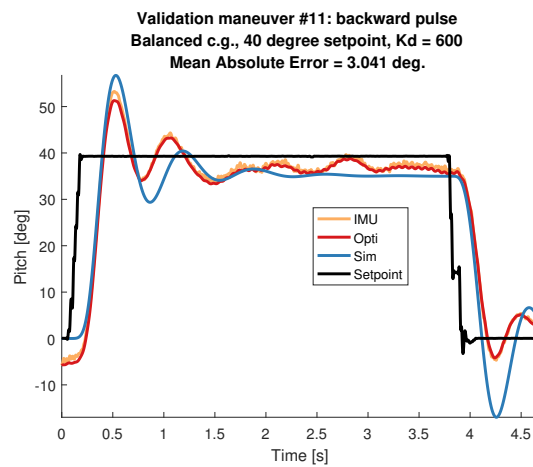


Figure C-46: Fourth validation step maneuver with rate feedback 600 (PPRZ units) and 40 degree pitch backward setpoint.

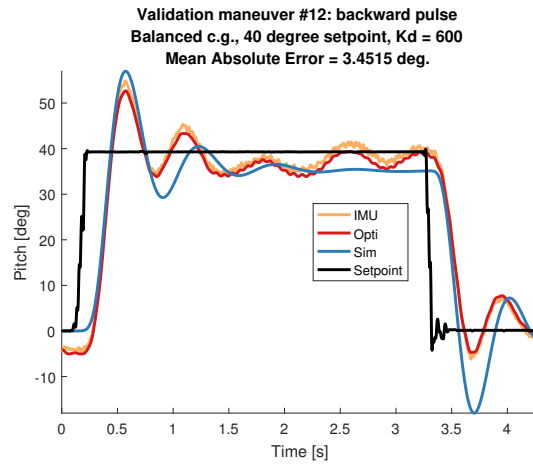


Figure C-47: Fifth validation step maneuver with rate feedback 600 (PPRZ units) and 40 degree pitch backward setpoint.

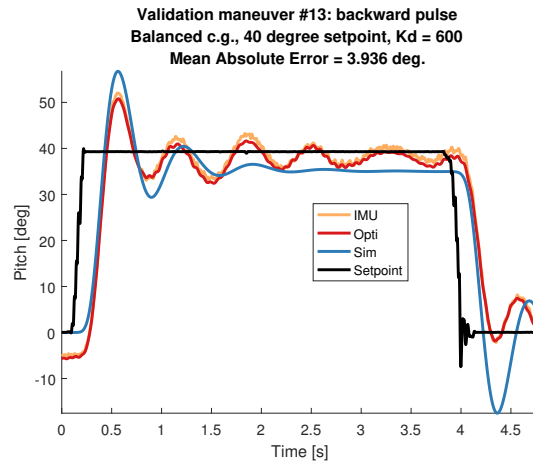


Figure C-48: Sixth validation step maneuver with rate feedback 600 (PPRZ units) and 40 degree pitch backward setpoint.

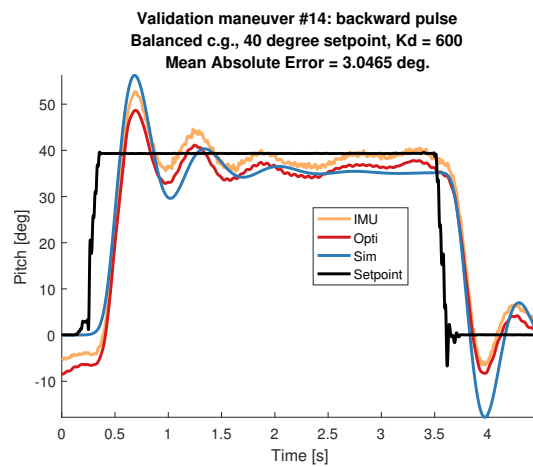


Figure C-49: Seventh validation step maneuver with rate feedback 600 (PPRZ units) and 40 degree pitch backward setpoint.

C-5 Maneuvers with 40 degree pitch setpoints, rate feedback gain 800

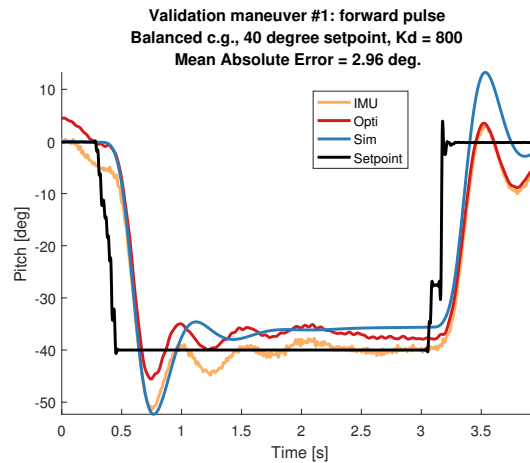


Figure C-50: First validation step maneuver with rate feedback 800 (PPRZ units) and 40 degree pitch forward setpoint.

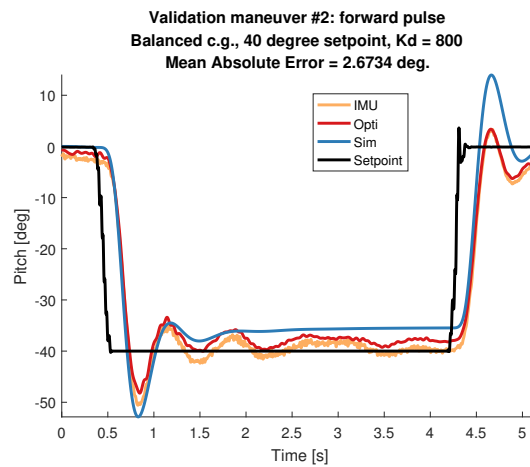


Figure C-51: Second validation step maneuver with rate feedback 800 (PPRZ units) and 40 degree pitch forward setpoint.

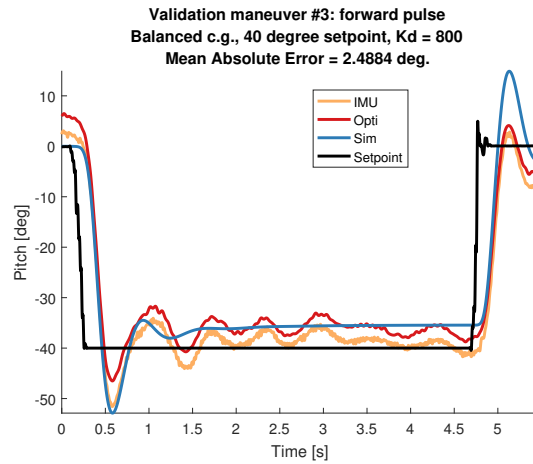


Figure C-52: Third validation step maneuver with rate feedback 800 (PPRZ units) and 40 degree pitch forward setpoint.

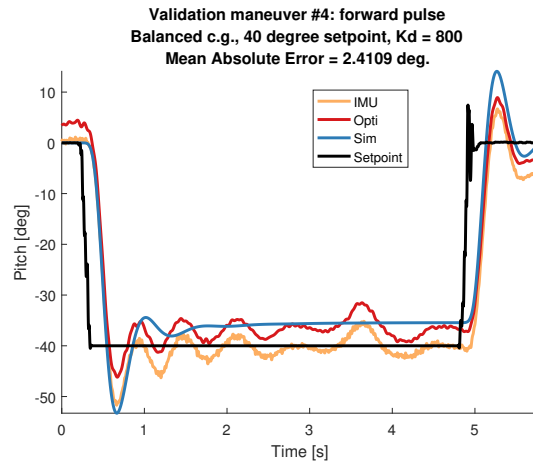


Figure C-53: Fourth validation step maneuver with rate feedback 800 (PPRZ units) and 40 degree pitch forward setpoint.

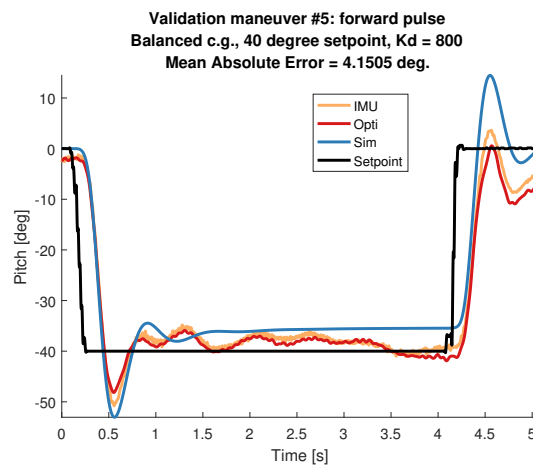


Figure C-54: Fifth validation step maneuver with rate feedback 800 (PPRZ units) and 40 degree pitch forward setpoint.

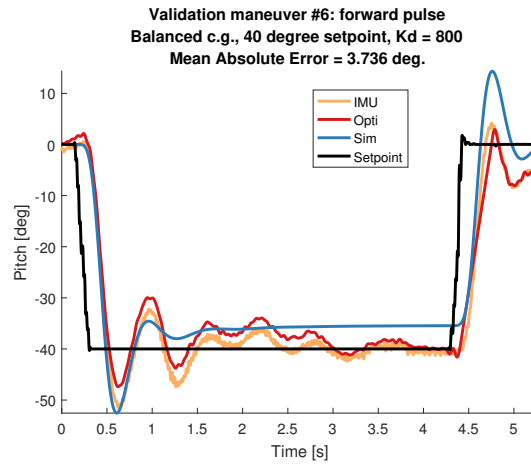


Figure C-55: Sixth validation step maneuver with rate feedback 800 (PPRZ units) and 40 degree pitch forward setpoint.

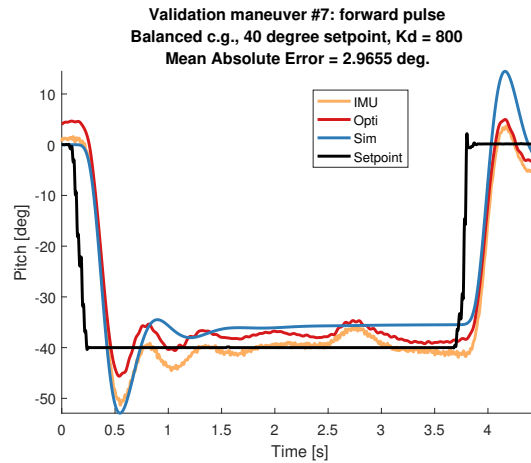


Figure C-56: Seventh validation step maneuver with rate feedback 800 (PPRZ units) and 40 degree pitch forward setpoint.

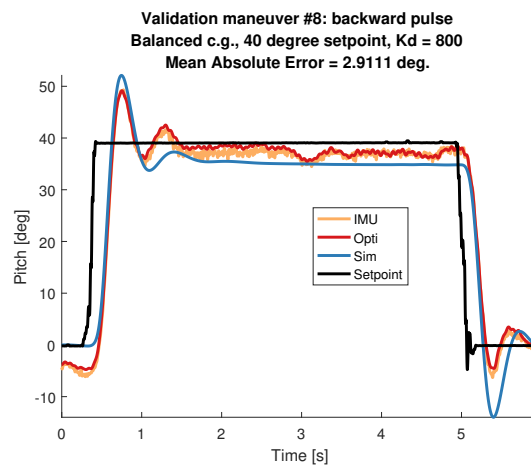


Figure C-57: First validation step maneuver with rate feedback 800 (PPRZ units) and 40 degree pitch backward setpoint.

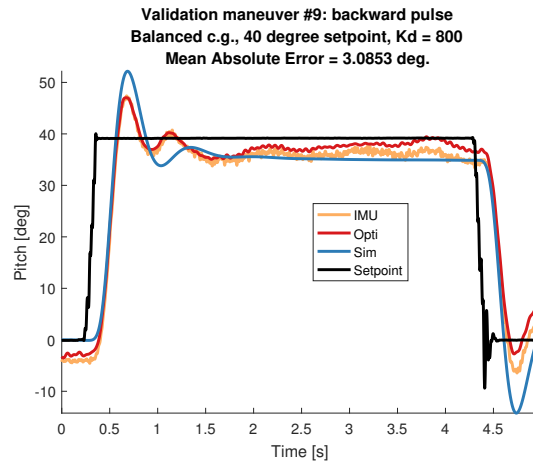


Figure C-58: Second validation step maneuver with rate feedback 800 (PPRZ units) and 40 degree pitch backward setpoint.

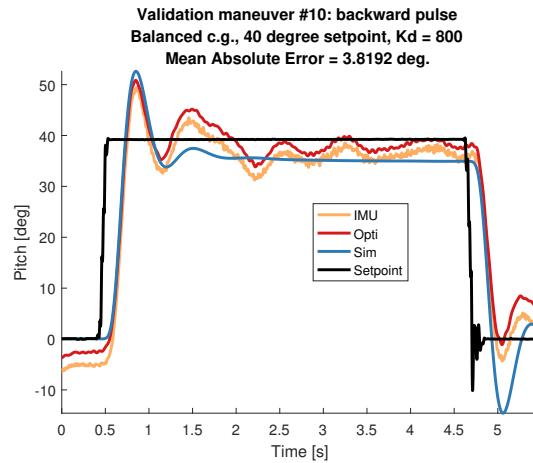


Figure C-59: Third validation step maneuver with rate feedback 800 (PPRZ units) and 40 degree pitch backward setpoint.

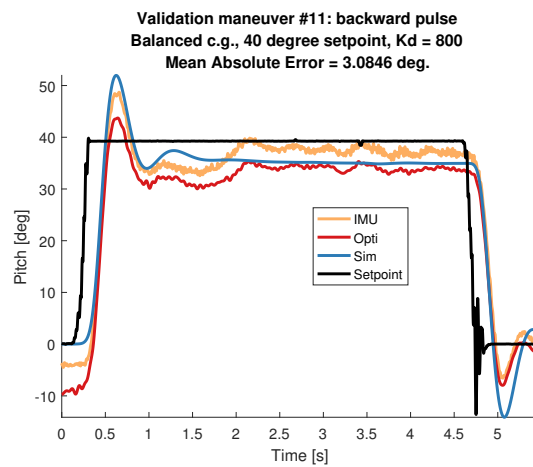


Figure C-60: Fourth validation step maneuver with rate feedback 800 (PPRZ units) and 40 degree pitch backward setpoint.

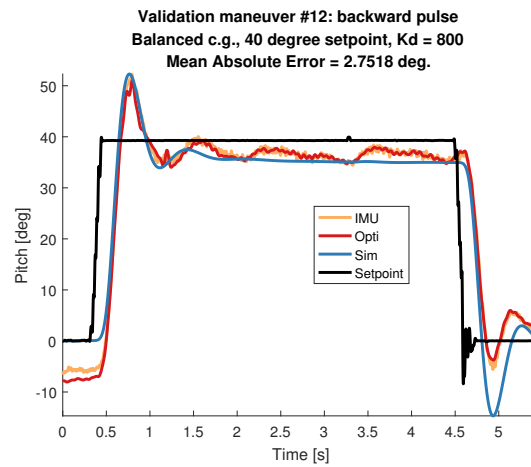


Figure C-61: Fifth validation step maneuver with rate feedback 800 (PPRZ units) and 40 degree pitch backward setpoint.

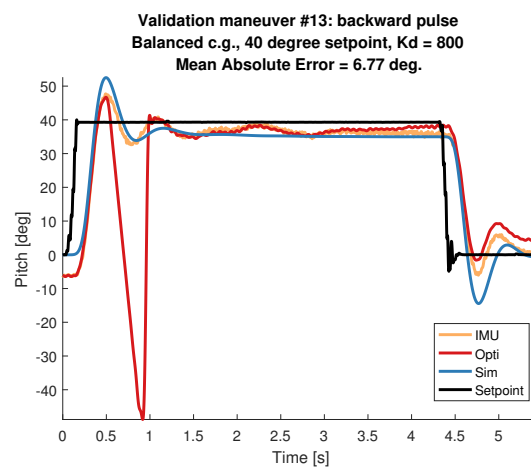


Figure C-62: Sixth validation step maneuver with rate feedback 800 (PPRZ units) and 40 degree pitch backward setpoint.

C-6 Maneuvers with 40 degree pitch setpoints, attitude feedback gain 3900

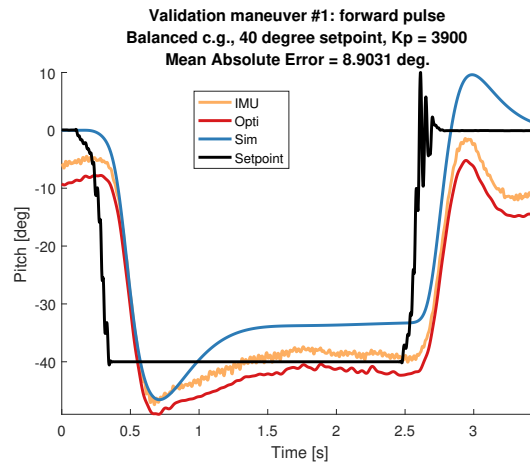


Figure C-63: First validation step maneuver with attitude feedback 3900 (PPRZ units) and 40 degree pitch forward setpoint.

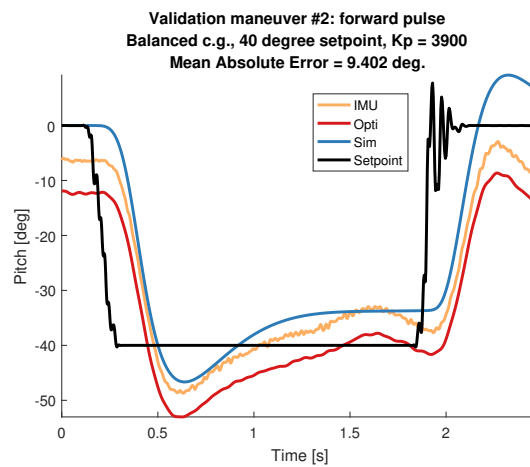


Figure C-64: Second validation step maneuver with attitude feedback 3900 (PPRZ units) and 40 degree pitch forward setpoint.

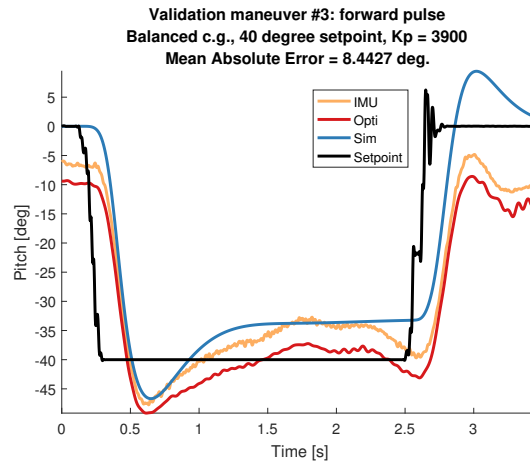


Figure C-65: Third validation step maneuver with attitude feedback 3900 (PPRZ units) and 40 degree pitch forward setpoint.

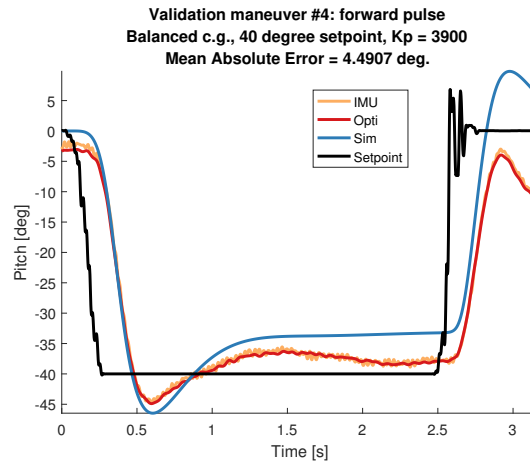


Figure C-66: Fourth validation step maneuver with attitude feedback 3900 (PPRZ units) and 40 degree pitch forward setpoint.

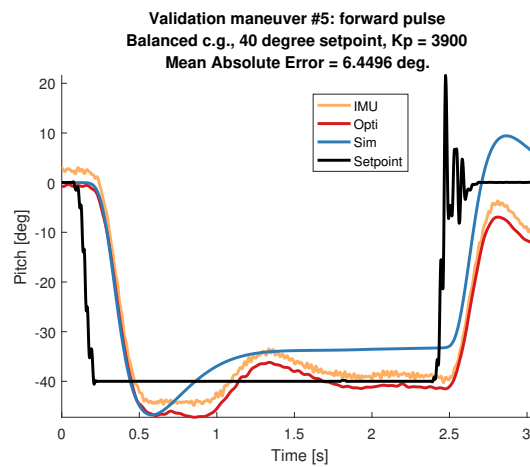


Figure C-67: Fifth validation step maneuver with attitude feedback 3900 (PPRZ units) and 40 degree pitch forward setpoint.

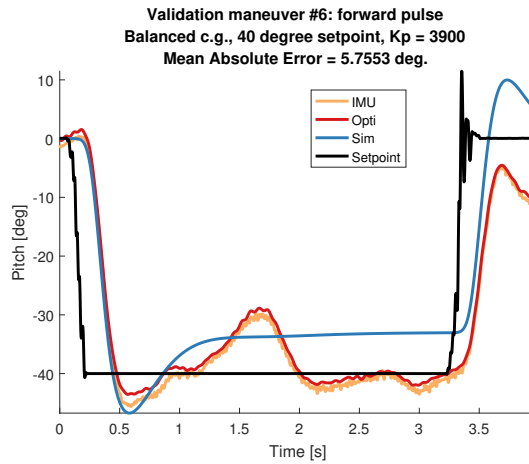


Figure C-68: Sixth validation step maneuver with attitude feedback 3900 (PPRZ units) and 40 degree pitch forward setpoint.

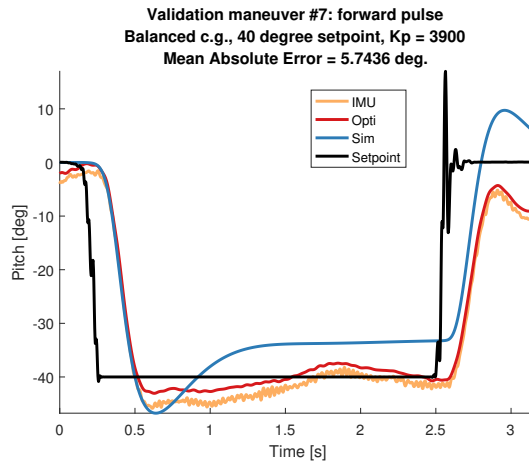


Figure C-69: Seventh validation step maneuver with attitude feedback 3900 (PPRZ units) and 40 degree pitch forward setpoint.

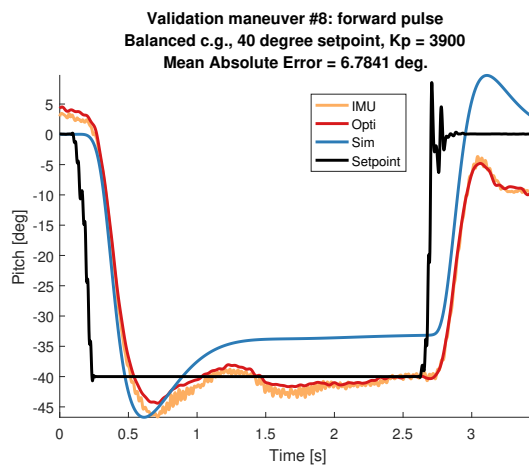


Figure C-70: Eighth validation step maneuver with attitude feedback 3900 (PPRZ units) and 40 degree pitch forward setpoint.

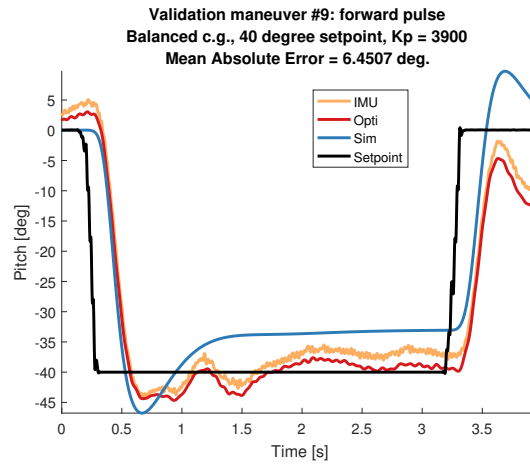


Figure C-71: Ninth validation step maneuver with attitude feedback 3900 (PPRZ units) and 40 degree pitch forward setpoint.

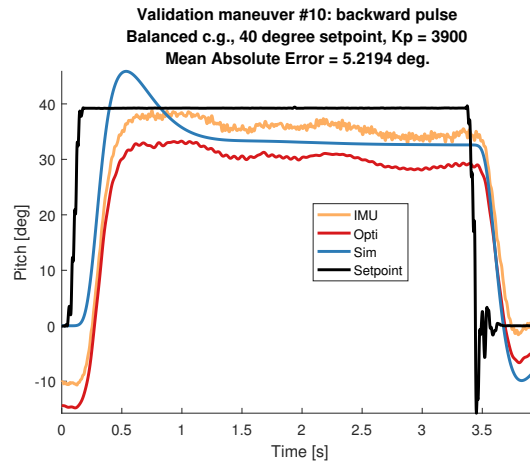


Figure C-72: First validation step maneuver with attitude feedback 3900 (PPRZ units) and 40 degree pitch backward setpoint.

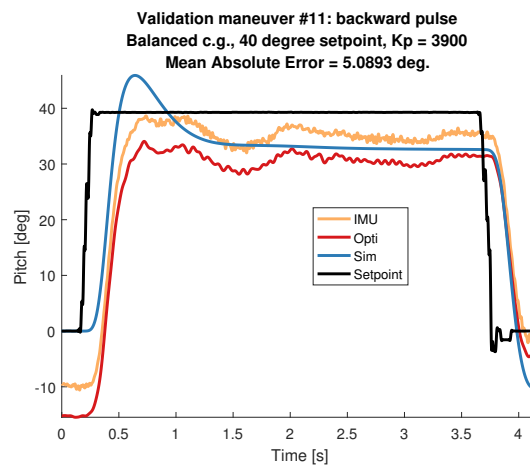


Figure C-73: Second validation step maneuver with attitude feedback 3900 (PPRZ units) and 40 degree pitch backward setpoint.

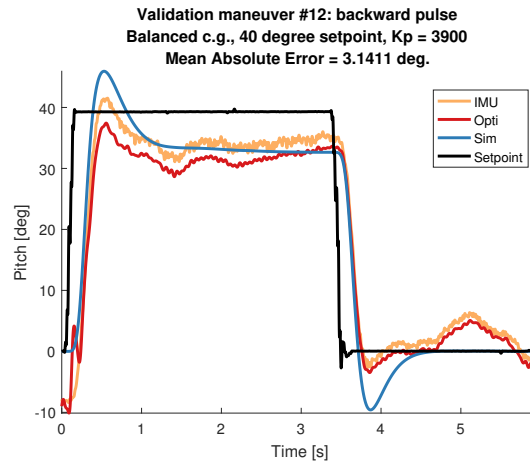


Figure C-74: Third validation step maneuver with attitude feedback 3900 (PPRZ units) and 40 degree pitch backward setpoint.

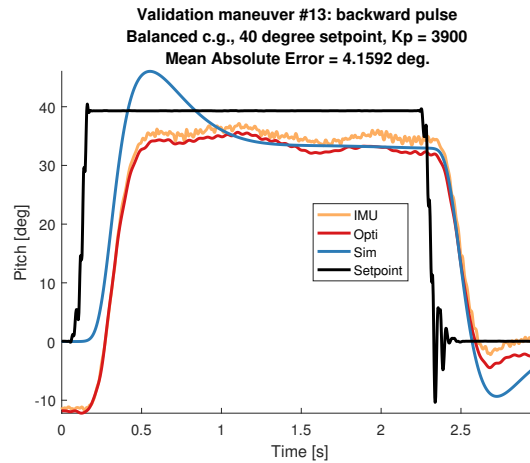


Figure C-75: Fourth validation step maneuver with attitude feedback 3900 (PPRZ units) and 40 degree pitch backward setpoint.

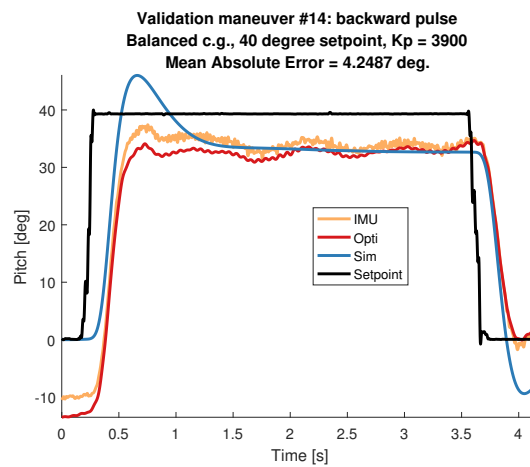


Figure C-76: Fifth validation step maneuver with attitude feedback 3900 (PPRZ units) and 40 degree pitch backward setpoint.

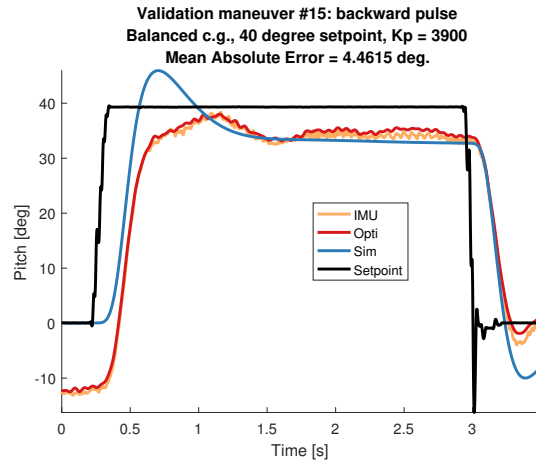


Figure C-77: Sixth validation step maneuver with attitude feedback 3900 (PPRZ units) and 40 degree pitch backward setpoint.

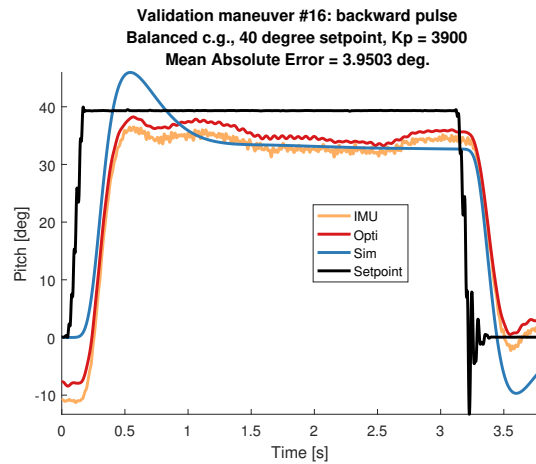


Figure C-78: Seventh validation step maneuver with attitude feedback 3900 (PPRZ units) and 40 degree pitch backward setpoint.

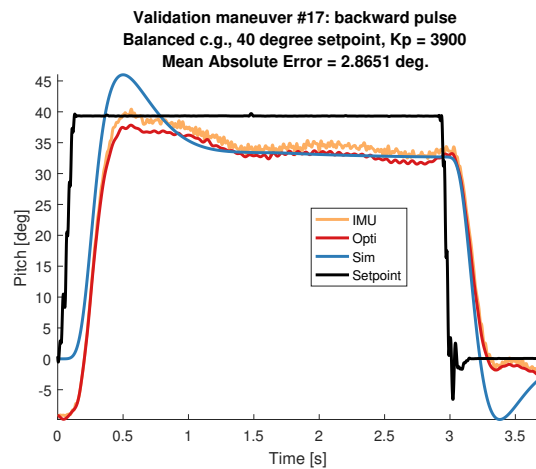


Figure C-79: Eighth validation step maneuver with attitude feedback 3900 (PPRZ units) and 40 degree pitch backward setpoint.

C-7 Maneuvers with 40 degree pitch setpoints, attitude feedback gain 11700

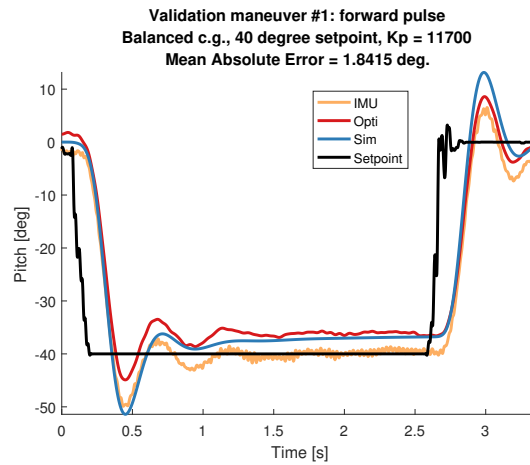


Figure C-80: First validation step maneuver with attitude feedback 11700 (PPRZ units) and 40 degree pitch forward setpoint.

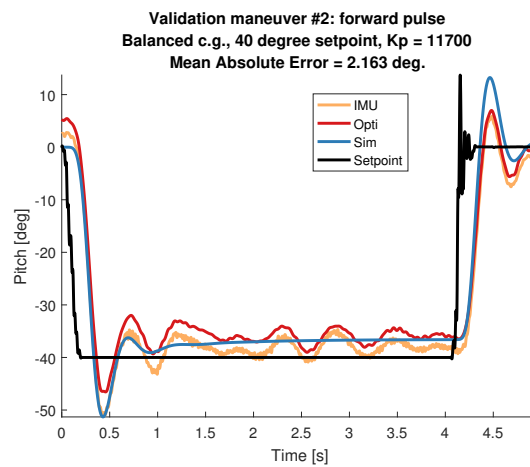


Figure C-81: Second validation step maneuver with attitude feedback 3900 (PPRZ units) and 40 degree pitch forward setpoint.

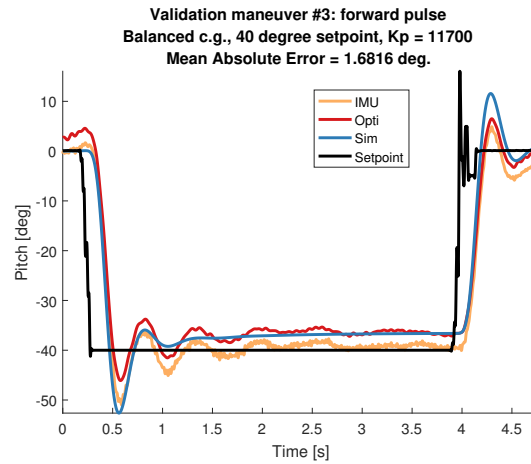


Figure C-82: Third validation step maneuver with attitude feedback 11700 (PPRZ units) and 40 degree pitch forward setpoint.

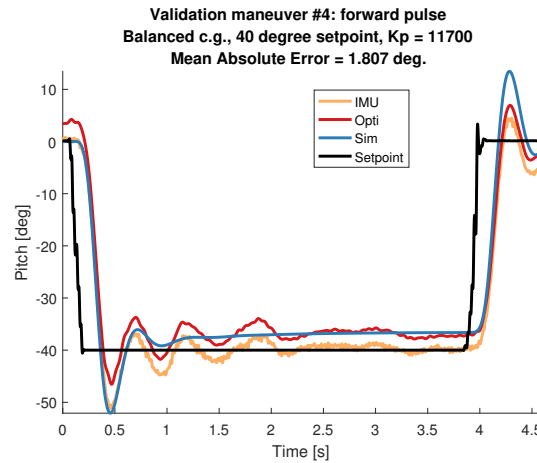


Figure C-83: Fourth validation step maneuver with attitude feedback 11700 (PPRZ units) and 40 degree pitch forward setpoint.

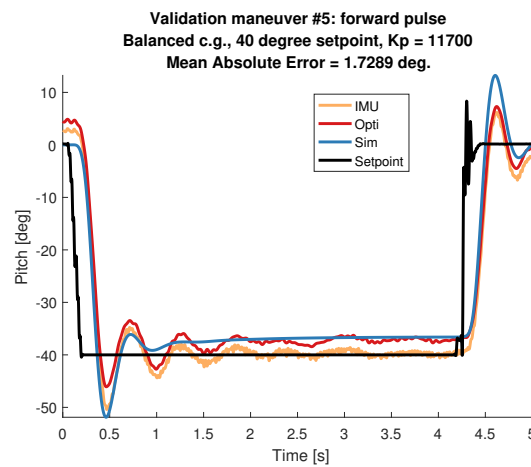


Figure C-84: Fifth validation step maneuver with attitude feedback 11700 (PPRZ units) and 40 degree pitch forward setpoint.

C-7 Maneuvers with 40 degree pitch setpoints, attitude feedback gain 11700 123

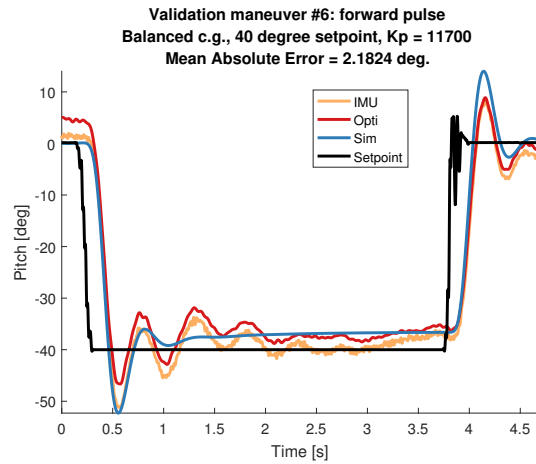


Figure C-85: Sixth validation step maneuver with attitude feedback 11700 (PPRZ units) and 40 degree pitch forward setpoint.

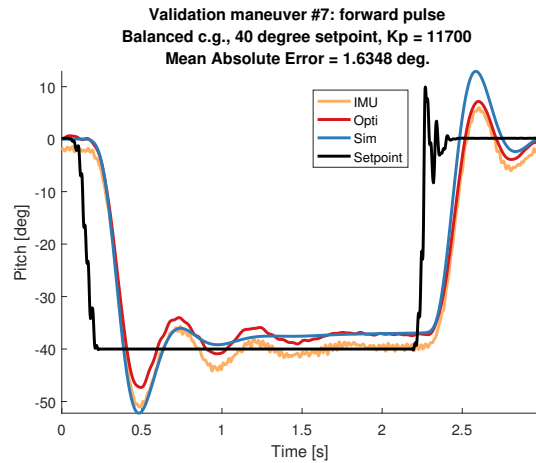


Figure C-86: Seventh validation step maneuver with attitude feedback 11700 (PPRZ units) and 40 degree pitch forward setpoint.

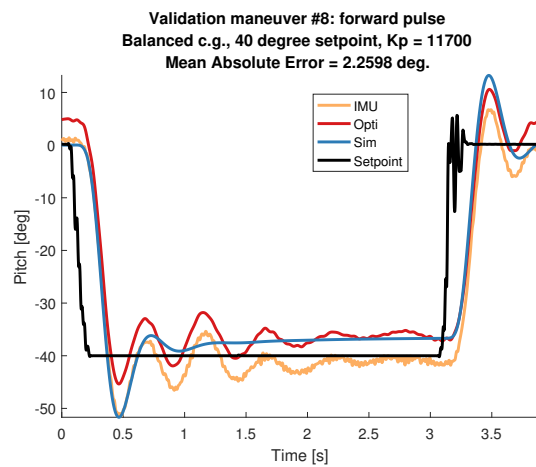


Figure C-87: Eighth validation step maneuver with attitude feedback 11700 (PPRZ units) and 40 degree pitch forward setpoint.

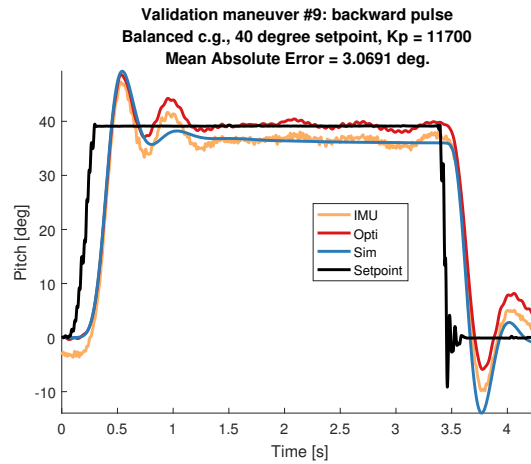


Figure C-88: Ninth validation step maneuver with attitude feedback 11700 (PPRZ units) and 40 degree pitch backward setpoint.

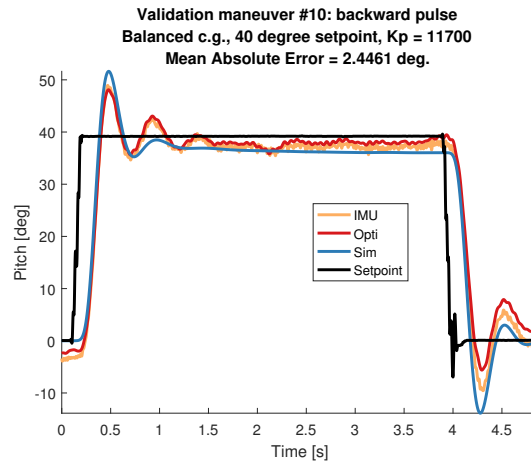


Figure C-89: First validation step maneuver with attitude feedback 11700 (PPRZ units) and 40 degree pitch backward setpoint.

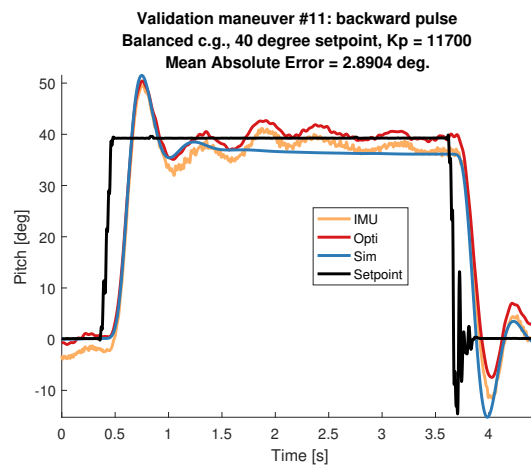


Figure C-90: Second validation step maneuver with attitude feedback 11700 (PPRZ units) and 40 degree pitch backward setpoint.

C-7 Maneuvers with 40 degree pitch setpoints, attitude feedback gain 11700 125

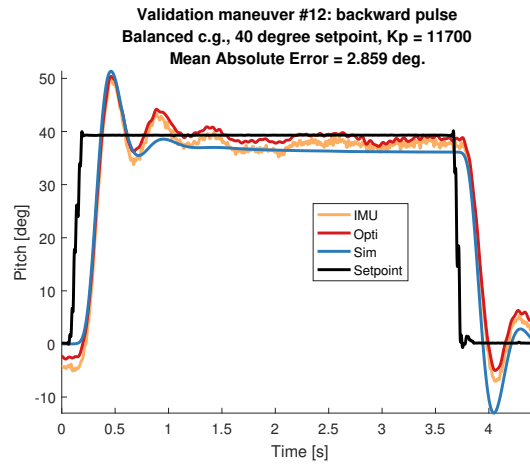


Figure C-91: Third validation step maneuver with attitude feedback 11700 (PPRZ units) and 40 degree pitch backward setpoint.

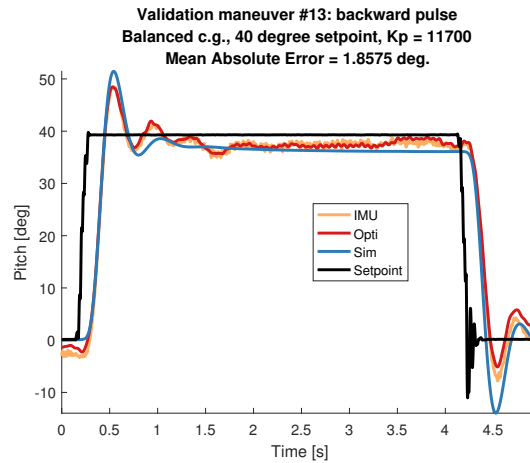


Figure C-92: Fourth validation step maneuver with attitude feedback 11700 (PPRZ units) and 40 degree pitch backward setpoint.

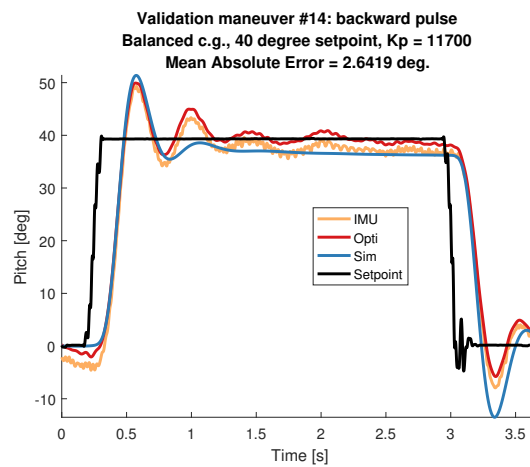


Figure C-93: Fifth validation step maneuver with attitude feedback 11700 (PPRZ units) and 40 degree pitch backward setpoint.

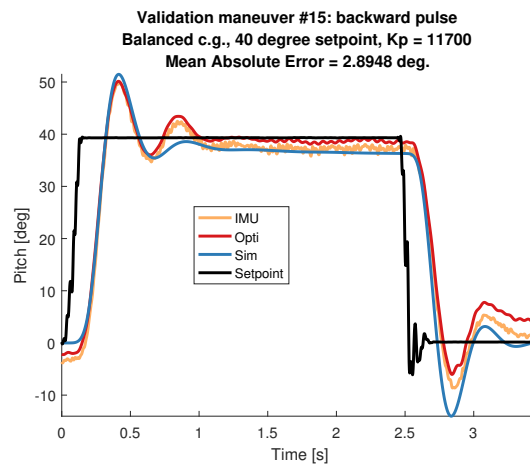


Figure C-94: Sixth validation step maneuver with attitude feedback 11700 (PPRZ units) and 40 degree pitch backward setpoint.

Bibliography

- [1] L. Zheng, T. L. Hedrick, and R. Mittal. “A comparative study of the hovering efficiency of flapping and revolving wings”. In: *Bioinspiration & Biomimetics* 8.3 (May 2013), pp. 1–13.
- [2] G. C. H. E. de Croon et al. “Design, aerodynamics and autonomy of the DelFly”. In: *Bioinspiration & Biomimetics* 7.2 (June 2012), pp. 1–16.
- [3] Mark A. Groen et al. “Improving flight performance of the flapping wing MAV DelFly II”. In: *International Micro Air Vehicle Conference and Competitions (IMAV 2010)*. 2010.
- [4] S. Deng et al. “Experimental Investigation of the Flapping Performance on ‘Delfly Micro’”. In: *IMAV 2013: Proceedings of the International Micro Air Vehicle Conference and Flight Competition, Toulouse, France, 17-20 September 2013*. September. 2013, pp. 17–20.
- [5] Matej Karasek et al. “A bio-inspired free-flying robot elucidates how fruit flies control rapid banked turns”. In: *(under review)* (2018).
- [6] Pakpong Chirarattananon, Kevin Y. Ma, and Robert J. Wood. “Adaptive control for takeoff, hovering, and landing of a robotic fly”. In: *2013 IEEE/RSJ International Conference on Intelligent Robots and Systems*. IEEE, Nov. 2013, pp. 3808–3815.
- [7] Matthew Keennon, Karl Klingebiel, and Henry Won. “Development of the Nano Hummingbird: A Tailless Flapping Wing Micro Air Vehicle”. In: *50th AIAA Aerospace Sciences Meeting including the New Horizons Forum and Aerospace Exposition*. January. Reston, Virginia: American Institute of Aeronautics and Astronautics, Jan. 2012, pp. 1–24.
- [8] Hoang Vu Phan, Taesam Kang, and Hoon Cheol Park. “Design and stable flight of a 21g insect-like tailless flapping wing micro air vehicle with angular rates feedback control”. In: *Bioinspiration & Biomimetics* 12.3 (Apr. 2017), p. 036006.
- [9] Mao Sun and Ji Kang Wang. “Flight stabilization control of a hovering model insect”. In: *Journal of Experimental Biology* 210.15 (Aug. 2007), pp. 2714–2722.

- [10] Yanlai Zhang and Mao Sun. “Dynamic flight stability of a hovering model insect: lateral motion”. In: *Acta Mechanica Sinica* 26.2 (May 2010), pp. 175–190.
- [11] Na Gao, Hikaru Aono, and Hao Liu. “Perturbation analysis of 6DoF flight dynamics and passive dynamic stability of hovering fruit fly *Drosophila melanogaster*”. In: *Journal of Theoretical Biology* 270.1 (Feb. 2011), pp. 98–111.
- [12] Sanjay P. Sane and Michael H. Dickinson. “The aerodynamic effects of wing rotation and a revised quasi-steady model of flapping flight.” In: *The Journal of experimental biology* 205.Pt 8 (Apr. 2002), pp. 1087–1096.
- [13] Matěj Karásek and André Preumont. “Flapping Flight Stability in Hover: A Comparison of Various Aerodynamic Models”. In: *International Journal of Micro Air Vehicles* 4.3 (Sept. 2012), pp. 203–226.
- [14] Sophie F. Armanini et al. “Quasi-steady aerodynamic model of clap-and-fling flapping MAV and validation using free-flight data”. In: *Bioinspiration & Biomimetics* 11.4 (June 2016), pp. 1–25.
- [15] Diana D. Chin and David Lentink. “Flapping wing aerodynamics: from insects to vertebrates”. In: *The Journal of Experimental Biology* 219.7 (Apr. 2016), pp. 920–932.
- [16] Torkel Weis-Fogh. “Quick Estimates of Flight Fitness in Hovering Animals, Including Novel Mechanisms for Lift Production”. In: *J. Exp. Biol.* 59.1 (1973), pp. 169–230.
- [17] M. Sun. “Dynamic flight stability of a hovering bumblebee”. In: *Journal of Experimental Biology* 208.3 (2005), pp. 447–459.
- [18] Floris van Breugel, William Regan, and Hod Lipson. “From insects to machines”. In: *IEEE Robotics & Automation Magazine* 15.4 (Dec. 2008), pp. 68–74.
- [19] Z. E. Teoh et al. “A hovering flapping-wing microrobot with altitude control and passive upright stability”. In: *2012 IEEE/RSJ International Conference on Intelligent Robots and Systems*. IEEE, Oct. 2012, pp. 3209–3216.
- [20] L. Ristroph et al. “Active and passive stabilization of body pitch in insect flight”. In: *Journal of The Royal Society Interface* 10.85 (2013), pp. 20130237–20130237.
- [21] A. Roshanbin et al. “COLIBRI: A hovering flapping twin-wing robot”. In: *International Journal of Micro Air Vehicles* 9.4 (Dec. 2017), pp. 270–282.
- [22] Mohd Firdaus Bin Abas et al. “Flapping wing micro-aerial-vehicle: Kinematics, membranes, and flapping mechanisms of ornithopter and insect flight”. In: *Chinese Journal of Aeronautics* 29.5 (Oct. 2016), pp. 1159–1177.
- [23] William Dickson et al. “An Integrative Model of Insect Flight Control (Invited)”. In: *44th AIAA Aerospace Sciences Meeting and Exhibit*. January. Reston, Virginia: American Institute of Aeronautics and Astronautics, Jan. 2006, pp. 1–19.
- [24] Bo Cheng and Xinyan Deng. “Near-hover dynamics and attitude stabilization of an insect model”. In: *Proceedings of the 2010 American Control Conference*. IEEE, June 2010, pp. 39–44.
- [25] T. Beatus, J. M. Guckenheimer, and I. Cohen. “Controlling roll perturbations in fruit flies”. In: *Journal of The Royal Society Interface* 12.105 (Mar. 2015), pp. 20150075–20150075.

- [26] Michael H. Dickinson and Florian T. Muijres. “The aerodynamics and control of free flight manoeuvres in *Drosophila*”. In: *Philosophical Transactions of the Royal Society B: Biological Sciences* 371.1704 (Sept. 2016), p. 20150388.
- [27] L. Ristroph et al. “Discovering the flight autostabilizer of fruit flies by inducing aerial stumbles”. In: *Proceedings of the National Academy of Sciences* 107.11 (Mar. 2010), pp. 4820–4824.
- [28] Michael W. Oppenheimer, David B. Doman, and David O. Sigthorsson. “Dynamics and Control of a Minimally Actuated Biomimetic Vehicle: Part II-Control”. In: *AIAA Guidance, Navigation, and Control Conference*. August. Reston, Virginia: American Institute of Aeronautics and Astronautics, Aug. 2009, pp. 1–23.
- [29] Michael W. Oppenheimer, David B. Doman, and David O. Sigthorsson. “Dynamics and Control of a Biomimetic Vehicle Using Biased Wingbeat Forcing Functions”. In: *Journal of Guidance, Control, and Dynamics* 34.1 (Jan. 2011), pp. 204–217.
- [30] Xinyan Deng, Luca Schenato, and S. S. Sastry. “Flapping flight for biomimetic robotic insects: part II-flight control design”. In: *IEEE Transactions on Robotics* 22.4 (Aug. 2006), pp. 789–803.
- [31] Yan Xiong and Mao Sun. “Stabilization control of a bumblebee in hovering and forward flight”. In: *Acta Mechanica Sinica* 25.1 (Feb. 2009), pp. 13–21.
- [32] Jason Geder et al. “Modeling and Control Design for a Flapping-Wing Nano Air Vehicle”. In: *AIAA Guidance, Navigation, and Control Conference*. August. Reston, Virginia: American Institute of Aeronautics and Astronautics, Aug. 2010, pp. 2–5.
- [33] Pakpong Chirarattananon, Kevin Y. Ma, and Robert J. Wood. “Single-loop control and trajectory following of a flapping-wing microrobot”. In: *2014 IEEE International Conference on Robotics and Automation (ICRA)*. IEEE, May 2014, pp. 37–44.
- [34] James E. Bluman, Chang-Kwon Kang, and Yuri B. Shtessel. “Sliding Mode Control of a Biomimetic Flapping Wing Micro Air Vehicle in Hover”. In: *AIAA Atmospheric Flight Mechanics Conference*. January. Reston, Virginia: American Institute of Aeronautics and Astronautics, Jan. 2017, pp. 1–16.
- [35] M. Alkitbi and Andrea Serrani. “Robust Control of a Flapping-Wing MAV by Differentiable Wingbeat Modulation”. In: *IFAC-PapersOnLine* 49.18 (2016), pp. 290–295.
- [36] Hala Rifaï, Nicolas Marchand, and Guylaine Poulin. “Bounded control of a flapping wing micro drone in three dimensions”. In: *2008 IEEE International Conference on Robotics and Automation*. IEEE, May 2008, pp. 164–169.
- [37] Qing Guo et al. “Hovering control based on fuzzy neural networks for biomimetic flying robotic”. In: *2008 International Conference on Information and Automation*. IEEE, June 2008, pp. 504–508.
- [38] Soon-Jo Chung and Michael Dorothy. “Neurobiologically Inspired Control of Engineered Flapping Flight”. In: *Journal of Guidance, Control, and Dynamics* 33.2 (Mar. 2010), pp. 440–453.
- [39] Sanjay K. Boddhu and John C. Gallagher. “Evolving non-autonomous neuromorphic flight control for a flapping-wing mechanical insect”. In: *2009 IEEE Workshop on Evolvable and Adaptive Hardware*. 1. IEEE, Mar. 2009, pp. 9–16.

- [40] Xinyan Deng et al. “Flapping flight for biomimetic robotic insects: part I-system modeling”. In: *IEEE Transactions on Robotics* 22.4 (Aug. 2006), pp. 776–788.
- [41] David B. Doman, Michael W. Oppenheimer, and David O. Sigthorsson. “Dynamics and Control of a Minimally Actuated Biomimetic Vehicle: Part I - Aerodynamic Model”. In: *AIAA Guidance, Navigation, and Control Conference*. August. Reston, Virginia: American Institute of Aeronautics and Astronautics, Aug. 2009, pp. 10–13.
- [42] David B. Doman, Michael W. Oppenheimer, and David O. Sigthorsson. “Wingbeat Shape Modulation for Flapping-Wing Micro-Air-Vehicle Control During Hover”. In: *Journal of Guidance, Control, and Dynamics* 33.3 (May 2010), pp. 724–739.
- [43] Michael W. Oppenheimer, David B. Doman, and David O. Sigthorsson. “Dynamics and Control of a Biomimetic Vehicle Using Biased Wingbeat Forcing Functions: Part I - Aerodynamic Model”. In: *Journal of Guidance, Control, and Dynamics* 34.1 (Jan. 2011), pp. 204–217.
- [44] Michael W. Oppenheimer et al. “Control of a Minimally Actuated Biomimetic Vehicle Using Quarter-Cycle Wingbeat Modulation”. In: *Journal of Guidance, Control, and Dynamics* 38.7 (July 2015), pp. 1187–1196.
- [45] Andrea Serrani. “Robust hovering control of a single-DOF flapping wing MAV”. In: *Proceedings of the 2010 American Control Conference*. IEEE, June 2010, pp. 1302–1307.
- [46] Andrea Serrani et al. “Robust Control of a 3-DOF Flapping Wing Micro Air Vehicle”. In: *AIAA Guidance, Navigation, and Control Conference*. August 2010. Reston, Virginia: American Institute of Aeronautics and Astronautics, Aug. 2010.
- [47] Hala Rifaï et al. “Biomimetic-based output feedback for attitude stabilization of a flapping-wing micro aerial vehicle”. In: *Robotica* 31.06 (Sept. 2013), pp. 955–968.
- [48] Bo Cheng and Xinyan Deng. “A Neural Adaptive Controller in Flapping Flight”. In: *Journal of Robotics and Mechatronics* 24.4 (Aug. 2012), pp. 602–611.
- [49] John C. Gallagher and Michael W. Oppenheimer. “An improved evolvable oscillator for all flight mode control of an insect-scale flapping-wing micro air vehicle”. In: *2011 IEEE Congress of Evolutionary Computation (CEC)*. IEEE, June 2011, pp. 417–425.
- [50] Qingwei Li and Hongjun Duan. “Modeling and Adaptive Control for Flapping-Wing Micro Aerial Vehicle”. In: *8th International Conference on Intelligent Computing*. Vol. LNCS 7389. 2012, pp. 269–276.
- [51] Hongjun Duan and Qingwei Li. “Attitude Control of Flapping-wing Micro Aerial Vehicle Based on Active Disturbance Rejection Control”. In: *2011 International Conference on Internet Computing and Information Services*. IEEE, Sept. 2011, pp. 396–398.
- [52] Jun-Seong Lee, Joong-Kwan Kim, and Jae-Hung Han. “Stroke Plane Control for Longitudinal Stabilization of Hovering Flapping Wing Air Vehicles”. In: *Journal of Guidance, Control, and Dynamics* 38.4 (Apr. 2015), pp. 800–806.
- [53] Lidia María Belmonte et al. “Robust Linear Longitudinal Feedback Control of a Flapping Wing Micro Air Vehicle”. In: *Artificial Computation in Biology and Medicine*. Vol. 9107. 2015, pp. 449–458.

- [54] Chang-ping Du, Jian-xin Xu, and Yao Zheng. “Application of iterative learning tuning to a dragonfly-like flapping wing micro aerial vehicle”. In: *2016 Chinese Control and Decision Conference (CCDC)*. IEEE, May 2016, pp. 4215–4220.
- [55] J. P. Whitney and Robert J. Wood. “Aeromechanics of passive rotation in flapping flight”. In: *Journal of Fluid Mechanics* 660 (Oct. 2010), pp. 197–220.
- [56] Kevin Y. Ma et al. “Controlled Flight of a Biologically Inspired, Insect-Scale Robot”. In: *Science* 340.6132 (May 2013), pp. 603–607.
- [57] Pakpong Chirarattananon, Kevin Y. Ma, and Robert J. Wood. “Adaptive control of a millimeter-scale flapping-wing robot”. In: *Bioinspiration & Biomimetics* 9.2 (May 2014), pp. 1–15.
- [58] Pakpong Chirarattananon, Kevin Y. Ma, and Robert J. Wood. “Perching with a robotic insect using adaptive tracking control and iterative learning control”. In: *The International Journal of Robotics Research* 35.10 (Sept. 2016), pp. 1185–1206.
- [59] Pakpong Chirarattananon et al. “Dynamics and flight control of a flapping-wing robotic insect in the presence of wind gusts”. In: *Interface Focus* 7.1 (Feb. 2017), pp. 1–14.
- [60] Michael W. Oppenheimer, David B. Doman, and David O. Sigthorsson. “Dynamics and Control of a Biomimetic Vehicle Using Biased Wingbeat Forcing Functions”. In: *Journal of Guidance, Control, and Dynamics* 34.1 (Jan. 2011), pp. 204–217.
- [61] Andrew R. Teel. “Global stabilization and restricted tracking for multiple integrators with bounded controls”. In: *Systems & Control Letters* 18.3 (Mar. 1992), pp. 165–171.
- [62] Andrew R. Teel. “A nonlinear small gain theorem for the analysis of control systems with saturation”. In: *IEEE Transactions on Automatic Control* 41.9 (1996), pp. 1256–1270.
- [63] José Guerrero-Castellanos et al. “Biomimetic-Based Output Feedback for Attitude Stabilization of Rigid Bodies: Real-Time Experimentation on a Quadrotor”. In: *Micromachines* 6.8 (Aug. 2015), pp. 993–1022.
- [64] J. Bayandor et al. “Adaptive control for bioinspired flapping wing robots”. In: *2013 American Control Conference*. IEEE, June 2013, pp. 609–614.
- [65] Jun-seong Lee, Joong-kwan Kim, and Jae-hung Han. “Control of Wing Stroke Plane Angle for Stabilizing of a Hovering Flapping-Wing Air Vehicle”. In: *AIAA Guidance, Navigation, and Control Conference*. January. Reston, Virginia: American Institute of Aeronautics and Astronautics, Jan. 2014.
- [66] Nestor O Perez-Arancibia et al. “Model-free control of a flapping-wing flying micro-robot”. In: *2013 16th International Conference on Advanced Robotics (ICAR)*. IEEE, Nov. 2013, pp. 1–8.
- [67] Wilson J. Rugh and Jeff S. Shamma. “Research on gain scheduling”. In: *Automatica* 36.10 (2000), pp. 1401–1425.
- [68] Karl Åström. *Encyclopedia of Systems and Control*. Ed. by John Baillieul and Tariq Samad. Bellman 1961. London: Springer London, 2014, pp. 1–9.
- [69] Emil Fresk and George Nikolakopoulos. “Full Quaternion Based Attitude Control for a Quadrotor”. In: *2013 European Control Conference*. 2013, pp. 3864–3869.

- [70] Ewoud J. J. Smeur, Qiping Chu, and G. C. H. E. de Croon. “Adaptive Incremental Nonlinear Dynamic Inversion for Attitude Control of Micro Air Vehicles”. In: *Journal of Guidance, Control, and Dynamics* 39.3 (Mar. 2016), pp. 450–461.
- [71] Robert Stengel. *Flight dynamics*. Princeton, NJ : Princeton University Press, 2004, p. 169.